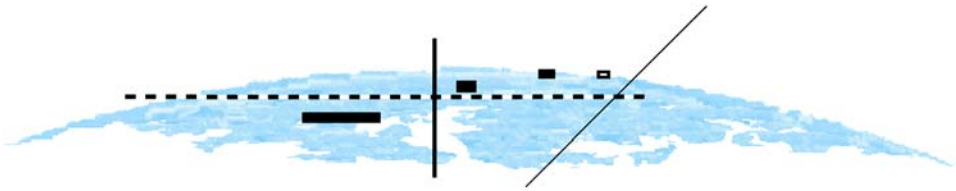

GeoForschungsZentrum Potsdam

STIFTUNG DES ÖFFENTLICHEN RECHTS

Scientific Technical Report

ISSN 1610-0956

Forough Sodoudi

Lithospheric structure of the Aegean obtained from P and S receiver functions

---

Dissertation
zur Erlangung des Doktorgrades
am Fachbereich Geowissenschaften
der Freien Universität Berlin

2005

Tag der mündlichen Prüfung: 21. June 2005

Erstgutachter: Prof. Dr. Rainer Kind
Zweitgutachter: Prof. Dr. Serge Shapiro

ABSTRACT

Aegean is one of the most tectonically complex areas worldwide. Because of its position in the back arc area of the active subduction of the African plate beneath the Eurasian plate as well as occurrence of two successive stages of extension within Aegean since Oligocene times, it belongs to the most interesting areas and has been the focus of many studies. In this thesis a joint P and S receiver function analysis is used to estimate the crustal and upper mantle structure in the whole Aegean Sea, mainland Greece and the island of Crete. To reach this goal, combined P and S receiver functions of teleseismic events are computed, which are recorded by a total number of 65 temporary and permanent stations including GEOFON, National Observatory of Athens, Cyclades-network, Mediterranean network and the Seisfaultgreece experiment. These combined data show a more dense coverage in the southern and central Aegean Sea where no information from P receiver functions can be obtained without OBS stations. The receiver function images reliably demonstrate the subducting oceanic African lithosphere up to northern Greece, where the slab is not marked by earthquakes. The results lead also to an average depth of 40 km for the subducted oceanic Moho beneath southern Crete, western Peleponnesus and southeast of Rhodes, which significantly increases down to the volcanic arc to a depth of 160 km. The oceanic Moho can be reliably followed further north to depth of 220 km beneath northern Greece. The new information on the oceanic and continental lithosphere deduced from the new technique of S receiver function clearly reveals the lithosphere-asthenosphere boundary beneath each part of the area. This boundary is estimated about 150 km beneath mainland Greece, which presents the continental Aegean lithosphere (Eurasian lithosphere) and shows a thickening from 100 km beneath southern Crete to about 225 km under volcanic arc of the subduction zone.

This thickening of the LAB towards the Aegean Sea is associated with the subduction of the oceanic African lithosphere beneath the Aegean plate. Moreover, detailed informations about the crustal thickness variation are inferred from this study. In Crete, the Aegean Moho varies from 25 km in the east to 33 km in the west. In the Cretan Sea a thin crust of approximately 20 km is observed, which thickens up to 30 km at the volcanic arc. A thicker crust of about 35 km beneath two volcanic islands in the Aegean (SANT, MILO) are also observed. In the northern Aegean Sea the crustal thickness is ranging between 25-28 km, whereas beneath western Greece a significantly crustal thickening resulted in a Moho depth of 32-38 km. The estimations in the Peleponnesus show a crustal thickness of 25-28 km.

Zusammenfassung

Das Ägäische Meer ist eines der tektonisch kompliziertesten Gebiete weltweit. Wegen seiner Lage im *backarc* Bereich der aktiven Subduktionszone von afrikanischer Platte unter die eurasische Platte sowie das Auftreten zweier aufeinanderfolgender Extensionsstadien im Ägäischen Meer seit dem Oligozän, gehört es zu einem der interessantesten Gebiete und war bereits Grundlage zahlreicher Studien. In der vorliegenden Arbeit wurde eine gemeinsame P und S *Receiver Function* Analyse durchgeführt, um die Struktur der Kruste und des oberen Mantels unterhalb des gesamten Ägäischen Meeres, des griechischen Festlandes und Kreta zu bestimmen. Zu diesem Zweck wurden P und S *Receiver Functions* von teleseismischen Ereignissen berechnet, die an 65 temporären bzw. permanenten Stationen unterschiedlicher Netzwerke (GEOFON, Nationalobservatorium von Athen, Cyclades network, Mediterranean network und Seisfaultgreece Experiment) aufgezeichnet worden sind. Die gemeinsamen Daten weisen eine dichte Überdeckung im südlichen und zentralen Ägäischen Meer auf, während von den P *Receiver Functions* allein hier keine Informationen ohne OBS-Stationen gewonnen werden können. Die subduzierte afrikanische Lithosphäre kann anhand der *Receiver Function* Darstellungen bis unter das nördliche Griechenland verfolgt werden. Hier wird die abtauchende Platte jedoch nicht mehr durch lokale Seismizität abgebildet. Die Ergebnisse führen zu einer durchschnittlichen Moho-Tiefe von 40 km für die subduzierte ozeanische Platte unterhalb Südkretas, Westpeloponnes und des Südostens von Rhodos, die bis auf 160 km unterhalb des vulkanischen Bogens zunimmt. Die ozeanische Moho kann bis in eine Tiefe von 220 km unterhalb des nördlichen Griechenlandes zuverlässig beobachtet werden. Die mittels der S *Receiver Function* Methode gewonnenen neuen Informationen über die ozeanische und kontinentale Lithosphäre zeigen die

Lithosphären-Asthenosphären Grenze für das gesamte Untersuchungsgebiet. Diese Grenze wird in ca. 150 km Tiefe unterhalb des griechischen Festlandes abgeschätzt, welches die kontinentale Ägäische Lithosphäre (eurasische Lithosphäre) darstellt und weist eine Zunahme um 100 km unterhalb Südkretas bis auf 225 km unterhalb des vulkanischen Bogens der Subduktionszone auf. Die Zunahme der Mächtigkeit der LAB in Richtung Ägäisches Meer wird mit der Subduktion der ozeanischen afrikanischen Lithosphäre unter die Ägäische Platte in Verbindung gebracht. Desweiteren können detailierte Informationen zur Variation der Krustenmächtigkeit im Untersuchungsgebiet aus dieser Studie abgeleitet werden. Unterhalb Kretas ändert sich die Tiefenlage der Ägäischen Moho von 25 km im Osten auf 33 km im Westen. Im kretischen Meer wird eine geringe Krustenmächtigkeit von ca. 20 km beobachtet, die zum vulkanischen Bogen hin auf 30 km zunimmt. Eine mächtigere Kruste von ca. 35 km wird unterhalb der vulkanischen Inseln im Ägäischen Meer (SANT, MILO) beobachtet. Im nördlichen Ägäischen Meer variiert die Krustenmächtigkeit zwischen 25-28 km, während die Kruste unterhalb Westgriechenlandes durch Krustenverdickung auf 32-38 km zugenommen hat. Die Abschätzungen für Peloponnes zeigen eine Krustenmächtigkeit von 25-28 km.

TABLE OF CONTENTS

Abstract **1**

Zusammenfassung **3**

Chapter 1 Introduction **9**

Chapter 2 Geology and tectonics of the Aegean **13**

2.1 Tectonic setting 15

2.1.1 The northern Aegean region 18

2.1.2 The western Aegean region 20

2.1.3 The southern Aegean subduction 22

2.1.4 The Cretan basin 24

2.2 Geological setting 25

2.3 Seismicity 28

2.4 Previous geophysical studies 30

2.4.1 The continental Moho of the Aegean plate 30

2.4.2 The oceanic Moho of the African plate 35

Chapter 3 Methods **39**

3.1 P-to-S receiver function method 39

3.1.1 Restitution 41

3.1.2 Rotation 42

3.1.3 Deconvolution..... 43
3.1.4 Moveout correction..... 46
3.1.5 Migration..... 49
3.1.6 Estimation of crustal thickness and Vp/Vs ratio... 50
3.2 S-to-P receiver function method..... 53
3.2.1 Lithosphere-asthenosphere boundary..... 56
3.2.2 Processing..... 56
3.2.3 Rotation..... 57
3.2.4 Deconvolution..... 61
3.2.5 Moveout correction and stacking..... 63

Chapter 4 Data..... 67
4.1 Data set for P receiver function analysis..... 67
4.1.1 Seismic stations..... 67
4.1.2 Prerequisites for P receiver function method..... 69
4.2 Data set for S receiver function analysis..... 69
4.2.1 Seismic stations..... 69
4.2.2 Prerequisites for S receiver function method..... 71

Chapter 5 Results and Discussions..... 73
5.1 Results from P receiver functions..... 73
5.1.1 Observed P receiver functions..... 73
5.1.2 Reversed Moho contrast in the forearc..... 78
5.1.3 Calculating Moho depth from Ps conversions..... 80
5.1.4 Calculated slab depth from Ps conversions..... 82
5.1.5 Receiver function migration..... 82
5.2 Results from S receiver functions..... 85

5.2.1 Observed S receiver functions..... 85
5.2.2 Distribution of Piercing points..... 87
5.2.3 Descending oceanic African Moho..... 87
5.2.4 Slab geometry obtained from profiles A-C..... 89
5.2.5 Slab geometry obtained from profiles D-F..... 92
5.2.6 Lithosphere-Asthenosphere boundary..... 93
5.3 Discussions..... 96
5.3.1 Thickness of the Lithosphere..... 96
5.3.2 Description of the Hellenic subduction zone 98
5.3.3 Reversed continental Moho contrast complication.. 101
5.3.4 Crustal thickness of the Aegean plate..... 104
5.3.4.1 The observed Moho phase beneath PENT and ATH..... 107
5.3.4.2 Presence of thick Moho under SANT and MILO..... 107
5.3.4.3 Moho depth map..... 110

Chapter 6 Concluding remarks..... **115**
6.1 Crust-mantle boundary of the Aegean plate..... 115
6.2 Crust-mantle boundary of the African plate..... 116
6.3 LAB beneath the whole area..... 117

References..... **119**
Appendix A: Stations List and Instrumentation **141**
Appendix B: List of events..... **145**
Appendix C: List of delay times and depth values..... **159**
Danksagung..... **165**

Lebenslauf..... **167**

CHAPTER 1

INTRODUCTION

Considering the complexity of the surface tectonics, it is important to investigate the structure of the underlying upper mantle in order to better understand the tectonic evolution of the region. The global scale tomographic image of the Earth's interior indicates that the structure in the top 100-200 km is closely related to the tectonic regime at the surface. To determine the physical properties of the deep structure, potential (gravity, magnetic, heat flow) or kinetic (seismic waves that generated from earthquakes) energy of the Earth itself and kinetic energy that is created artificially (seismic sounding) have been used in the Aegean region since the 1960' s. The crustal and mantle structures of the Aegean are the result of a complex history that started probably during the late Cretaceous (e.g. McKenzie, 1972) and resulted in the subduction of Africa beneath Eurasia, the building of mountain belts caused by collision between Apulia and western Greece and the creation of stretched regions, which has occurred since the early Miocene. Tectonic processes such as subduction change the equilibrium conditions in the Earth’s layered medium. As a result of these changes in the mantle, the surface geology is greatly affected or directly formed by material carried from the mantle or the subducting oceanic lithosphere.

There is a lot of unknown geological and geophysical details in the Aegean region that need to be determined. The present-day kinematics and surface deformation are reasonably well known because of the large amount of GPS measurements covering the Aegean (e.g. Le Pichon et al., 1995; Reilinger et al., 1997; McClusky et al., 2000). However, the present-day kinematics is certainly different from that of the past, as it is attested by the large amount of rotation that the Hellenic arc experienced since the

Oligocene (Kissel and Laj, 1988). Therefore, a knowledge of the crustal structure, compared with the present day kinematics could help constraining the previous episodes of deformation.

The lithospheric structure in the Aegean area has been the focus of many studies. Travel time analysis from local and regional earthquakes, refraction profiles beneath specific areas in the Aegean, tomographic studies in the Aegean scale and gravity measurements have mapped the structure, but the data are scarce and of varying quality. However, multi disciplinary studies are needed to resolve the complex structure beneath this area.

The main goal of this thesis is to obtain homogeneous and detailed image of the continental Aegean lithosphere and subducting African slab in the region of Crete, the mainland of Greece and the Aegean down to the mantle from direct seismological observations. To reach this goal, I apply the P receiver function technique to the existing data recorded by 43 stations belonging to various networks across the whole area. The fine structure within the crust is resolved by P receiver functions, even though the derived seismological images have large gaps where no station exists. The structure in areas not covered by P receiver functions are obtained with S receiver functions, which offers an opportunity to sample seismic boundaries in sea areas with data from nearby land stations. S receiver functions are computed for 50 stations within the area. Both techniques compliment each other, with P receiver functions resolving the most prominent structures beneath each seismological station and S receiver functions filling in the gaps deduced from P receiver function images and resulting structures of larger distances from the stations and at larger depths in the mantle. S receiver functions have no multiples which disturb P receiver functions and therefore are utilized to identify such a discontinuity like the lithosphere-asthenosphere boundary, which is generally invisible in P receiver functions. The combination of all these data resulted in the most complete high-resolution image of the crustal thickness of the continental Aegean plate as well as the subducting oceanic African plate. The geometry of the subducted plate is also presented using S receiver functions. Finally, a map of the lithosphere-asthenosphere boundary is obtained from

the S data.

This thesis consists of six chapters :

Chapter **2** explains the detailed tectonic and geological settings of the Aegean area. The seismicity of the Aegean is presented and the previous works in this region are briefly introduced.

Chapter **3** discusses the P and S receiver function methods as they have been used and developed for this study. Synthetic receiver functions are shown to describe different aspects of the steps taken to process the data.

Chapter **4** introduces the data set, the utilized seismic stations for each method and the various networks, which have been deployed.

Chapter **5** shows the results obtained from P and S receiver function methods across the whole Aegean. The results on the continental Aegean lithosphere as well as on the descending African lithosphere are presented in trems of two maps. The new information about the lithosphere-asthenosphere boundary is also presented for the first time for both, the continental and oceanic plates. The results are then discussed and compared with previous studies in this area.

Chapter **6** includes the concluding remarks of the study.

The additional information on the events and instrumentation used in this study are then presented in appendixes **A** and **B**. Appendix **C** includes the arrival times of Ps and Sp conversions from major discontinuities in the crust and upper mantle as well as calculated depth values.

CHAPTER 2

In this chapter, the geological and tectonic settings of the study area as well as the seismicity and previous studies are introduced.

2. Geology and tectonics of the Aegean

The deformation pattern in the Mediterranean region that constructs a low elevated part of the Alpine Himalayan belt is rather complex, as usually occurs in continental collision zones. Five arcuate belts are situated in the Mediterranean region. Four of them have island arc system characteristics, with marginal seas. The southern Aegean region is one of them (Fig. 2.1)

In general view, the Aegean region is bounded to the north by the stable continental Eurasian plate, to the west by the Adriatic region, to the east by the central Anatolian, and to the south by the oceanic material beneath the Mediterranean Sea (northern edge of the African plate). The Aegean Sea floor (about 350 m mean depth) is seen as a high plateau between the deeper Black Sea floor (mean depth 1300 m) and Mediterranean Sea floor (mean depth 1500 m). The Aegean is characterized by a relatively thicker crust (25-30 km) than a typical oceanic crust, which might be interpreted as a thinned continental crust.

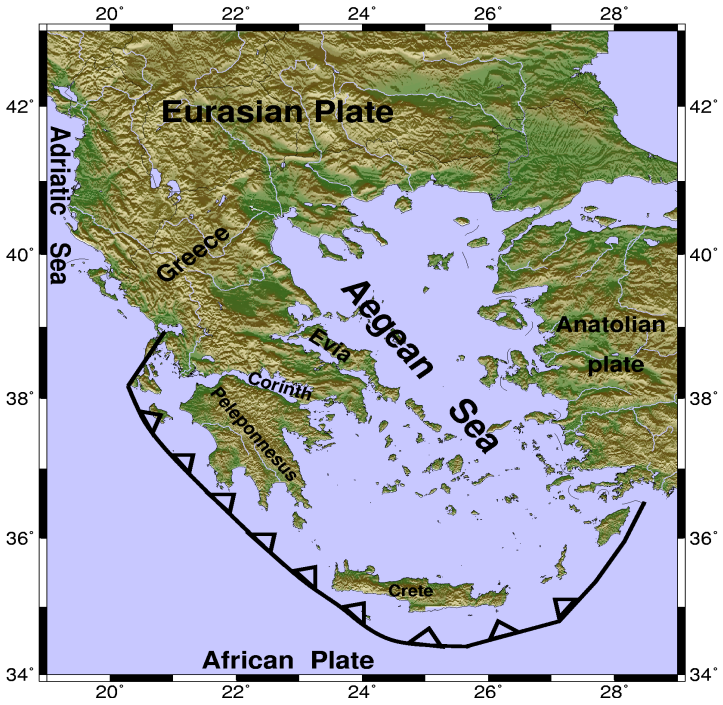

Fig. 2.1. Aegean Sea and its surrounding area. The Aegean micro plate located in the convergent region between the Eurasian and the African plates and bounded to the west by the Adriatic Sea and to the east by central Anatolia.

The Aegean is also situated in the convergent boundary between the African plate and Eurasian plate (Fig. 2.1). The crustal and mantle structures of the Aegean are the result of a complex history that started probably during the late Cretaceous (e.g. McKenzie, 1972). The African plate has rotated counter-clockwise with respect to Eurasian plate during the last 92 My (Müller & Kahle, 1993). The existence of a calc-alkaline inner volcanic arc, the spatial distribution of earthquakes and detailed tomographic studies indicate the existence of a northward-dipping subducted slab beneath this region (African plate beneath Eurasian plate). However, in the Aegean a roughly N-S directed lithosphere shortening rate is increasing from west to east (Müller et al., 1997). The region is also characterized by high heat flow, which is related to thinned and deformed (stretched) continental crust. This thinning is continuing till now. For this reason, it is the world wide most seismically active and rapidly internally deforming area of the entire Alpine-Himalayan belt and at of all

continents (McKenzie, 1972; Mercier et al., 1977; Jackson et al., 1994).

2.1 Tectonic setting

The tectonic framework of the eastern Mediterranean is dominated by the collision of the Arabian and African plates with Eurasia (McKenzie, 1970; Jackson and McKenzie , 1984, 1988). Plate tectonic models (DeMets et al., 1990) based on analysis of global seafloor spreading, fault systems, and earthquake slip vectors indicate that the Arabian plate is moving in a north-northwest direction relative to Eurasia at a rate of about 18 mm/yr (McClusky et al., 2000), averaged over about 3 My (Fig. 2.2). These models also indicate that the African plate is moving in a northly direction relative to Eurasia at a rate of about 6 mm/yr (McClusky et al., 2000). Different motions between Africa and Arabia (~ 8-15 mm/yr) are thought to be taken up predominantly by left-lateral motion along the Dead Sea transform fault. This northward motion results in westward extrusion of the Anatolian plate (McKenzie, 1970).

According to this model, the Anatolian plate is rotating counter-clockwise, relatively to Eurasia, about an Euler pole located north of the Sinai peninsula (31.1°N, 33.4°E), which results in a slip velocity of 24 mm/yr in the North Anatolian Fault (McClusky et al., 2000). This westward motion of Anatolia does not result in a compressional field in the Aegean area, which on the contrary, is dominated by an extensional stress field. Moreover, the Aegean moves as a more or less coherent unit in respect to Eurasia with much high velocity (~30 mm/yr) than the corresponding velocity of the Anatolian plate (Kahle et al., 1998) to the southwest. For this reason the Aegean area can be considered as separate microplate. This high rate convergence along the Hellenic arc, rather than the relative northward motion of the African plate itself, requires that the arc moves southward (~ 30 mm/yr) relative to Eurasia proper (e.g. Sonder and England, 1989; Royden, 1993). The corresponding velocity direction changes from ENE-WSW in the central coast of western Turkey to NNE-SSW in the southern Aegean. It also shows that additional forces (except from Anatolia westward motion) exist in the Aegean, related either to the slab pull or the gravitational collapse

of the Hellenides, which are responsible for this velocity acceleration and change of direction from almost E-W to almost N-S.

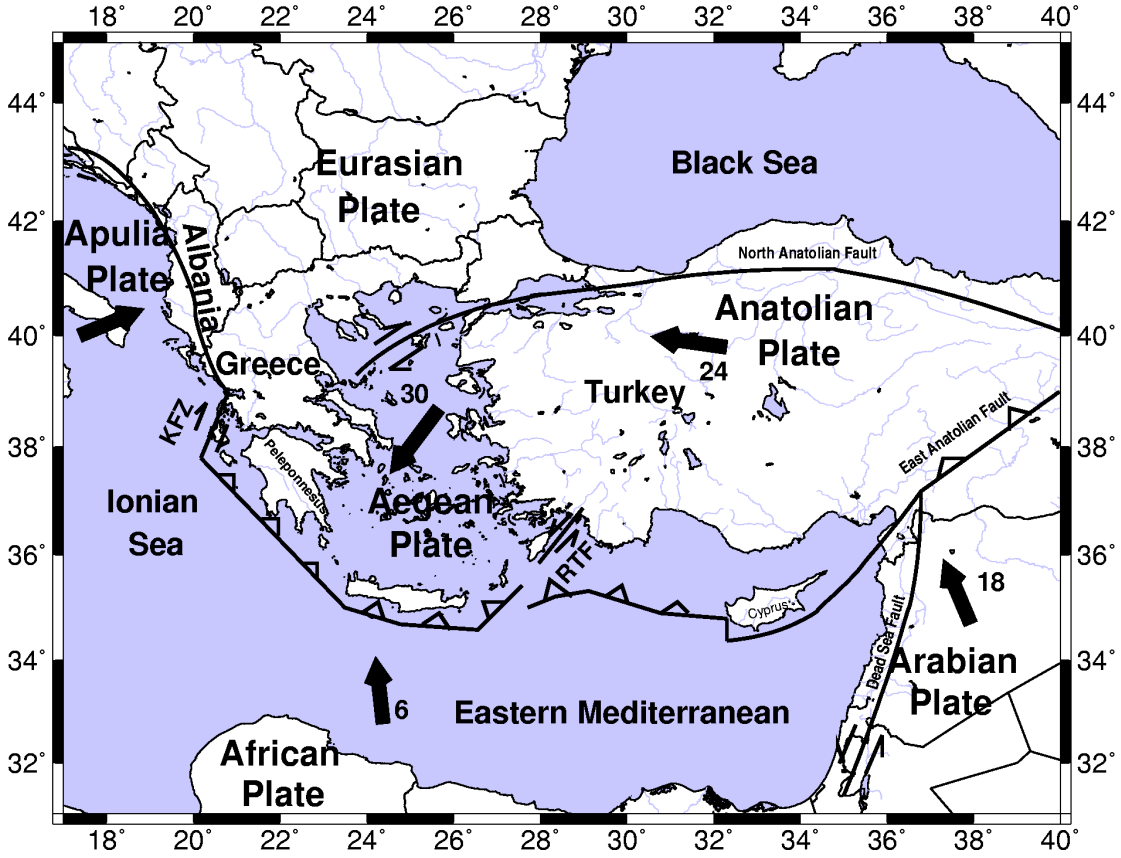

Fig.2.2 Schematic illustration of the principal motions affect active tectonics in the Aegean and surrounding area. Arrows indicate the direction of the motion relative to Eurasia. The values (mm/yr) are shown near each arrow (McClusky et al. 2000).

However, the GPS measurements (McClusky et al., 2000) indicate that relative to Eurasia, the southwestern Aegean-Peleponnesus moves toward the SSW in a coherent fashion with low internal deformation (< 2 mm/yr). The southeastern Aegean region deviates significantly from this coherent motion, rotating counter-clockwise and moving toward the Hellenic trench (i.e. toward the SE) at ~ 10 mm/yr relative to the southwestern Aegean. The Africa-Aegean relative motion is approximately normal to the arc along the western arc and parallel to the arc along the eastern segment. Rapid motions in the SE Aegean are a response to rapid sinking of the downgoing plate and

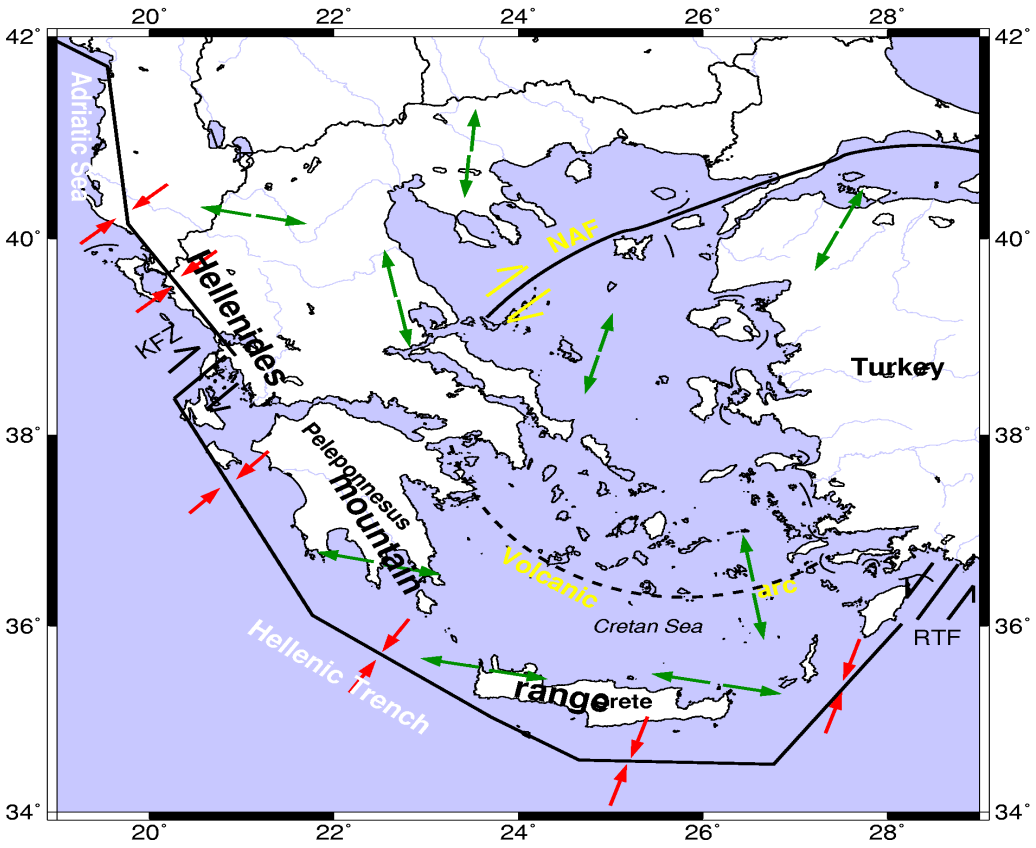

Fig. 2.3. The compression and extension zones in the Aegean. The main zone of compression with thrust faults observed along the Hellenic arc and western coast of Greece is related to the subduction of the African plate beneath Eurasian plate and continental type collision between Adriatic microplate and western Greek-Albanian coast, respectively. The back arc area is dominated by N-S extension. A narrow zone of E-W extension is observed in the forearc area. The situation of volcanic arc associated with the subduction is marked with dashed line. NAF = North Anatolian Fault; KFZ = Kefallonia Fault Zone; RTF = Rhodes Transform Fault.

allows the arc to override more easily the African plate. Right lateral strike-slip deformation associated with the North Anatolian Fault extends into the north Aegean terminating near the Gulf of Corinth or continuing to the Kefallonia fault zone (KFZ in Figure 2.2). The dextral sense of strike-slip motion along the KFZ indicates an abrupt change in the Hellenic subduction zone (Kahle et al., 1998). The north Aegean trough and Gulf of Corinth form the principal northern boundary of the southwestern Aegean plate. The main zone of compression observed along the Hellenic arc and along the western coast of northern Greece and Albania (Fig. 2.3), is associated with

the subduction of the eastern Mediterranean beneath the Aegean and the continental-continental type collision between Adriatic (Apulia) microplate and the western Greek-Albanian coasts (Anderson & Jackson 1987). The largest part of the backarc Aegean is dominated by normal faults with an E-W trend, suggesting an N-S extension. Fault plane solutions *(*Kirtazi et al. 1987, Papazachos et al. 1998) and GPS measurements (McClusky et al. 2000) indicated recently a narrow zone of E-W extension in the forearc, which lies between the thrust faults of the outer Hellenic arc and the N-S extension field in the backarc area.

The eastern limit of the Hellenic arc is defined by the sinistral Rhodes Transform Fault (RTF in Figure 2.3), which is the only main strike-slip fault in the Aegean area, which is not dextral. All data mentioned previously exhibit a consistent geotectonic setting, which is characterized by a dominant extension regime in the Aegean after Lower Miocene. Figure 2.3 shows the schematic illustration of the different zones in the Aegean area. The kinematic status of the Aegean shows that the bulk of the motion of the southern Aegean/Hellenic arc appears to be associated with coherent rotation of the southern Aegean plate. It is likely concentrated on SW striking, right-lateral strike slip and NW oriented normal faults in the northern Aegean Sea. It shows also a gradual increase of deformation velocities, with respect to Europe, from 10 mm/yr in the North Aegean Trough up to 35-40 mm/yr in the southernmost Hellenic arc.

2.1.1 The northern Aegean region

The area is characterized by a high strike slip component of faults with the N-S extensional regime of the Aegean region (Fig. 2.4). The Strymon basin, North Aegean Trough (NAT) and Skyros basin are the most pronounced and are considered as the major tectonic elements in northern Aegean region, as shown in Figure 2.4. Young tectonic activity in this region has affected the geomorphology and normal strike-slip

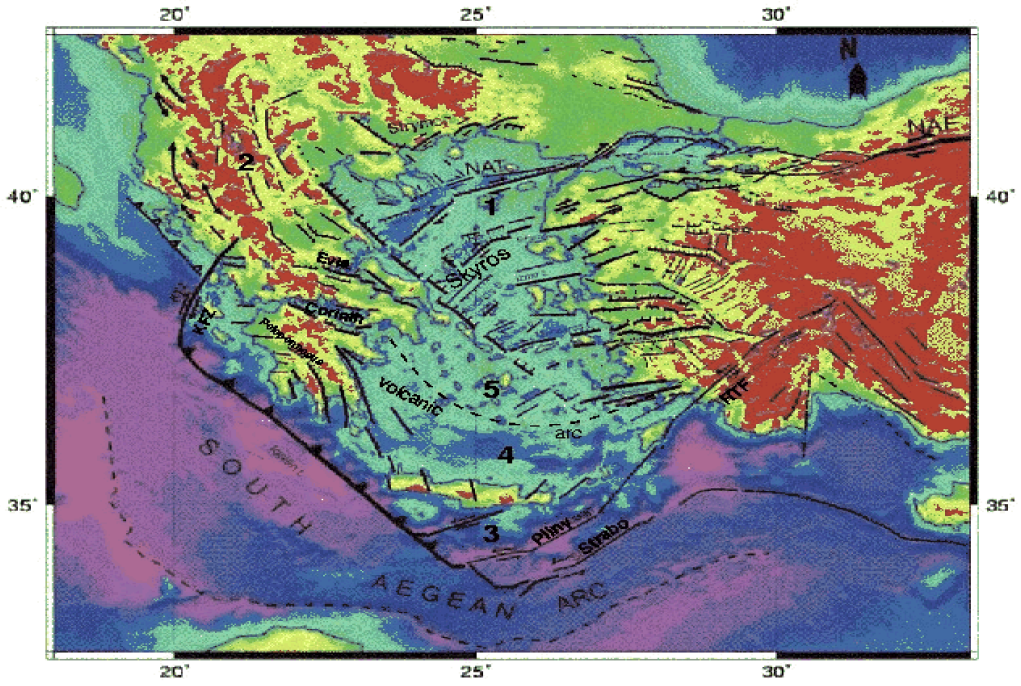

Fig. 2.4. Detailed tectonic features in the Aegean. Aegean is dominated by normal faulting. Major normal faults are demonstrated in the central and northern Aegean Sea. The most strike-slip faults are dextral in the Aegean area, the only main fault, which is not dextral is situated in the eastern part of the Hellenic arc (RTF). 1 = northern Aegean region; 2 = western Aegean region; 3 = south Aegean subduction; 4 = Cretan basin; 5 = Cyclades.

faults. Therefore, dominantly oblique faults and basins can be clearly seen in the morphology. Strikes of the strike-slip faulting in these places are the most obvious trend in the seismicity map (Taymaz et al., 1991). A good correlation also exists between seismic activity and high heat flow anomalies, because these are deep reaching oblique faults (Alptekin et al., 1990; Simsek, 1997). Gravity anomalies are also well correlated with these major tectonic lines. The narrow North Anatolian Fault Zone (NAFZ) is the northern boundary of the westward moving Anatolian block and connects the compressional regime in eastern Anatolia with the extensional regime in the Aegean Sea area. As Figure 2.4 shows, the boundary becomes diffused further west.

The most dramatic bathymetric feature of the North Aegean Sea is the NAT (Fig. 2.4), which consists of a series of deep fault-bounded active basins (Vogt & Higgs, 1969; Lort, 1971; Le Pichon et al., 1984). This feature is thought to be a continuation of the

NAF by many scientists. Intense seismicity clearly defines also the trough. The trough is bounded by a major fault to the south and by a faulted flexure to the north (Le Pichon et al., 1984; Mascle & Martin, 1990). Major seismic activity is also located about 50 km south of the deep linear trough, which could be related to the northward dipping major fault (McKenzie, 1972). The NAT could be divided into two basins: the Saros basin, which trends ENE-WSW in the east and the Sporades basin, which trends NE-SW in the west. These changes indicate that the western part of the Anatolian Trough contains a larger component of opening (McKenzie, 1978). The focal mechanism solutions show that the N-S component of the motion increases westward (McKenzie, 1978). Focal mechanism solutions in the NAT show mainly right lateral strike-slip faulting (Taymaz et al., 1991). Large principal values of extension are also found in the northern Aegean Sea, along the NAT.

2.1.2 The western Aegean region

The Hellenides-Peloponnisian peninsula is characterized by a NNW-SSE trending mountain belt that constructed of nappe pilling. The belt is indicated by the high negative Bouguer anomaly that strikes NNW-SSE in the western Aegean Region (Makris, 1977, 1985). The NW-SE trending normal faults to the NE continue step by step to the center of the Aegean Sea and the last fault zone occurs as eastward dipping asymmetric grabens (e.g., Strymon, Sporades, Skyros, Anros, Mikonos, Sirna) and bounds NE-SW trending basins like NAT. The lineation of faults over the Greek mainland can be seen from bathymetry-topography and geological structure as well as focal mechanism solutions of moderate earthquakes (Roberts & Jackson, 1991; Taymaz et al., 1991). These grabens were also been recognized from diffuse seismicity distribution (McKenzie, 1978; Hatzfeld et al., 1990; Rigo et al., 1995; Hatzfeld al., 1996; Mueller et al., 1997) and a structural geological study (Mercier et al., 1976). West of the Aegean region, two huge NW-WNW striking grabens (Corinth and Evia) are obvious from bathymetry and topography. Towards the Aegean Sea, these two basins become more southerly. These grabens indicate recent extensional structures

that accommodate a large part of the internal deformation of Hellenides-Peloponnesus (see for detail Armijo et al., 1996; Hatzfeld et al., 1996). The Gulf of Corinth, located between Greece and Peloponnesus, is a recent N-S extensional structure (McKenzie, 1978). It is not older than 2 My, it opens at about 1 cm/yr and accommodates a large part of the extensional deformation (Armijo et al., 1996; Hatzfeld et al., 1996). It is suggested that this detachment is due to the uncoupling of the brittle upper crust from a more ductile lower crust (Melis et al., 1989; Rigo et al., 1995). Its western segment is connected to the Ionian trench system by a series of NE-trending transform faults with dextral polarity called the Kefallonia Fault Zone (KFZ). The rift's eastern segment transverses the volcanic arc of the Aegean orogeny and can be considered as a first order cross fault (Hatzfeld al., 1996). Taymaz et al. (1991) suggest that the overall NE-SW motion across the region is due to oblique (left-lateral and normal) slip on these normal faults (Berckhemer & Kowalczyk, 1978; Myrianthis, 1984). North of the Kefallonia fault zone, the NW end of the subduction zone is characterized by a negligible motion (see Mueller et al., 1997). In northwestern Greece and Albania, there is a band of thrusting near the western coasts (Fig. 2.4). The most obvious problem in accounting for the observed deformation is the relationship between the thrusting and normal faulting further east in the northwestern part of the area (see also McKenzie, 1978).

Geodetic displacements measured in Greece indicate that slip vectors parallel to the main basin trend over east and central Aegean. But in the western Aegean region the vectors are perpendicular to the strike of large scale crustal blocks bounded by normal faults (Oral et al., 1995; Jolivet et al., 1994). On the other hand the vectors further east in the Aegean Sea are approximately parallel to the bathymetric features which could be thought as cross grabens (e.g., Sengör, 1987). Taymaz et al. (1991), by considering paleomagnetic and seismotectonic results, suggest that central Greece is rotating clockwise about a vertical axis as a whole. Furthermore, some evidences show that the sediments deposited in the Evia and Attica are tilted southward. The analysis of structures in the metamorphic domes on footwalls of Evia and Attica faults also show a very consistent fabric with flat foliation and N-S trend of stretching lineation (Faure

& Bonneau, 1988; Gautier et al., 1990; Jolivet et al., 1994). Extension is taken up by low angle normal faults, which bound upper crustal blocks such as Evia and Attica (Jolivet et al., 1994). The Cyclades area is also like a shallow plateau that appear as a footwall of the northward dipping faults to the NE. It is obvious that the NAT and the other NE-SW trending basins end in front of these blocks as cross grabens.

2.1.3 The southern Aegean subduction - Hellenic Subduction Zone

Based on earthquake investigations as well as geophysical investigations of gravity, magnetic and seismic wave velocities, Papazachos & Comninakis (1969, 1971), Caputo et al. (1970), Papazachos (1973), Comninakis & Papazachos (1980), Gregersen & Jaeger (1984), Makropoulos & Burton (1984) and Spakman et al. (1988) have shown the existence of dipping lithospheric material towards the concave side of the southern Aegean arc (Hellenic arc). Negative low Bouguer gravity anomalies show that there is dense material (a sinkable slab) beneath Crete, Rhodes and the Pelopennesus (Ryan et al., 1969; Makris, 1985; Tsokas & Hansen, 1997).

Recent volcanism on some islands parallel to the South Aegean trough is related to a subducting plate in the Aegean region (Fig. 2.4). Most of the heat flow values observed over the Cyclades are like those for other island arc systems in the world (Jongsma, 1974). Furthermore, heat flow values increase towards the inside of the arc from the trench, as they do in the Kuril and Japan island arcs. The Hellenic arc has such general characteristics of the arcs as a trench in its convex side, a seismicity belt, negative free air anomaly along the trench, a sedimentary arc in the trench as well as a volcanic arc and a marginal sea (Aegean Sea) in its concave part.

However, the Benioff zone ends beneath the volcanic arc (~ 180 km), only tomographic results (Spakman et al., 1988, 1993; Papazachos et al., 1995) show that the Benioff zone must extend further to the north. At greater depths the slab could not accumulate stress because it may behave as plastic material above a critical heat and pressure. Limited isotopic data suggest that little of the sediment is incorporated into

the volcanic rocks of the Aegean arc (Barton et al., 1983; Briqueu et al., 1986). This means that it is not transported deep enough into the mantle for melting to occur. A low-velocity layer is observed in the upper mantle in the middle of the Aegean Sea from earthquakes data (Spakman et al., 1993; Papazachos, 1994; Papazachos et al., 1995). This remarkable low velocity anomaly may be caused by the dehydration of the subducting lithosphere around a depth of 80 to 90 km (Papazachos & Nolet, 1997; Tsokas & Hansen, 1997).

Along the western coast of Albania and Greece, and seaward of a trench from SW Greece through Crete to SW Turkey, the Hellenic arc is one of the most remarkable tectonic features of the Mediterranean area (Fig. 2.4). This is the consuming boundary of the African plate in the region. However, the location of the consuming boundary is not perfectly known. Recent tomographic results (Papazachos & Nolet, 1997) indicate that the lithosphere dives approximately along the line of the south coast of Crete.

A narrow zone of negative free air gravity anomalies (Woodside & Bowin, 1970, Allan & Morelli, 1971) and low seismic wave velocities (Alessandrini et al., 1997; Papazachos & Nolet, 1997) coincides with this trench. A thick sedimentary prism along the trench causes these anomalies. The detailed morphology in this trough is extremely complicated. The South Aegean Trench named Hellenic trench, consists of a number of prominent deep basins that form an arc shape from Kefallonia to Rhodes (e.g., Ryan et al., 1969). To the east of the trough there are narrow linear basins called the Pliny and Strabo trenches. On the other hand, along the Ionian trench, structures west of Crete are not linearized and they extend towards the Ionian Sea (McKenzie, 1978). These depressions are collectively called the South Aegean Trough (SAT). To the east, based on focal mechanism solutions of earthquakes and shallow seismic profiles, McKenzie (1972) suggested that the Pliny Trench is the main zone of subduction, rather than the Strabo Trench as supposed by Ryan et al. (1973). On the other hand the Strabo trench continues further to the NE than the Pliny Trench and probably links up with another trench system to the east (Fig. 2.4).

Because the convergent rate is high enough (~ 35 mm/yr), the deforming structures

can be clearly seen in batherymetry without sedimentary carpet. However these deep basins of the Hellenic trench are considerably shallower and more highly curved (R=400km) than the other subduction related main trenches elsewhere in the world (Le Pichon & Angelier, 1979; Jongsma, 1977).

Based on microearthquake data, focal mechanism solutions of earthquakes and normal faulting in the region, indicate NW-SE extension in southern Peleponnesus, western Crete and E-W extension in central and eastern Crete (Hatzfeld et al., 1993). The Peleponnesus have NNW elongated faults, Crete has E-W, ENE-WSW and NE-SW strike faults and Rhodes has NNE-SSW elongated faults. These faults are mainly normal and strike parallel to the elongation of the Hellenic trench system. It was also suggested that the present day E-W extension of the south Aegean region is related to the arc curvature, and the arc parallel extension is possibly related to slabpull force.

2.1.4 The Cretan Basin

The Cretan basin (see Figure 2.4) is situated between the outer arc (Kithera, Andikithera, Crete, Karpathos and Rhodes) and the active volcanic arc (the Cyclades, Thira, Milos etc.). Based on crustal thickness determinations, maximum extension occurs in the Cretan Basin region. This area just behind the consuming boundary has been stretched perhaps more than any other part of the Aegean (Le Pichon & Angelier, 1979, 1981; Angelier et al., 1982), but now is an undeforming part of the Aegean region. McKenzie (1978) suggested that the region moves to the south as a whole i.e., not deforming internally. It is characterized by the highest positive gravity anomalies in the Aegean region. The models of some scientists (McKenzie, 1978; Le Pichon & Angelier, 1979; Angelier & Le Pichon, 1980; Angelier et al., 1982), based on the relation between crustal thickness and extension, show that Crete is detached from the Cyclades area.

The deformation in this region must have slowed down recently, probably because of collision to the south of the Hellenic trench. By using seismic profiling information, Mascle & Martin (1990) observed decreasing extension since the Late Miocene in the

Cretan basin. In the southern part of the Aegean there is little recent seismic activity clearly identifiable beneath the Cretan Sea (Galanopoulos, 1967; Ergin, 1966). This would suggest that there is no deformation in the Cretan Sea. The Cretan basin consists of a series of elongated depressions, which follow the trend of the volcanic arc. There is a general eastward increase in the depths of the basins (Maley & Johnson, 1971). The southern margin of the Cretan basin is also fault controlled (Jongsma, 1975). Mascle & Martin (1990) described this basin as a half graben. A major downward dipping fault can be traced for 105 km N of the eastern half of Crete. The N-S faults in the region continue to the south with a NNE-SSW direction (Angelier et al., 1982). The E-W normal faults in Crete continue to the north in the Cretan Basin (Angelier et al., 1982).

2.2 Geological setting

The African plate (Tethys Ocean) is being consumed by subduction towards the north. The crust of Alpine Himalayan belt is constructed of approximately parallel trending units whose configuration developed in paleotectonic times. To both sides of the Aegean Sea (Greece and Turkey), the units that are massifs and suture zones (ophiolite and blue schists) are linked to each other (Fig. 2.5). As the Tethys closed, pieces of continent (terrenes) were swept together (accreted) to form a tampon mass between African and Eurasian plates. Evidence for this accretion may be found in the Turkish and Greek ophiolite suture zones. In the Aegean area, these units and ophiolitic suture zones are cut by prominent post orogenic active extensional structures. The Eocene blueschists and eclogites in the Cyclades in the center of the Aegean Sea indicates that during the Mid-Eocene the region was characterized by a thick continental crust (> 50 km) because of a compressional regime. The timing and cause of transition from compressional to extensional regime in the Aegean region are not well defined.

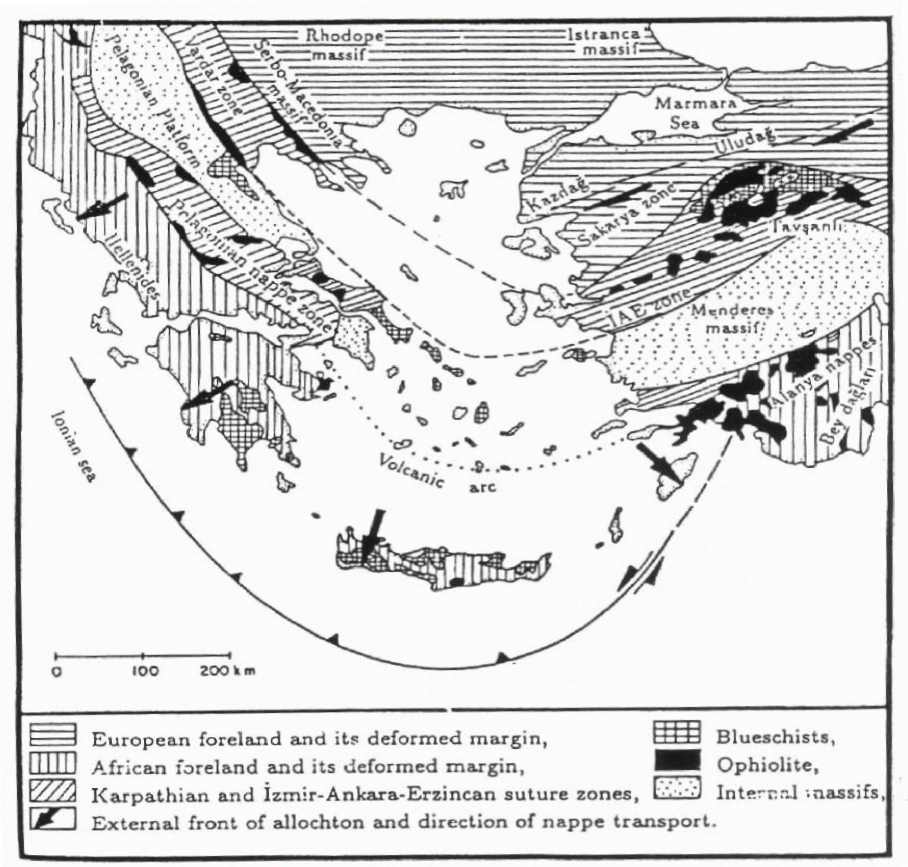

Fig. 2.5. Geological map of the Aegean.

Estimates of the age of transition from compressional to extensional regime range from Late Oligocene to Late Miocene. The underlying cause of the extensional regime is also debated. One possibility is the gravitational collapse of the major topography created as a result of the mid-Eocene crustal thickening. A second is the rollback of the South Aegean Subduction Zone, creating a back-arc-type extension. The third are the forces of the boundaries created by the collision of the Africa-Arabian plate with the Eurasian plate. It is likely that, prior to the Oligo-Miocene time, the slow convergence between Africa and Eurasia was accommodated by northward-dipping subduction along E-W trending boundary. Geological estimates of average extension rates in the Aegean are poorly constrained.

Sengör et al. (1985) suggest that the onset of extension is thought to predate the initiation of the NAF and has been estimated as Miocene in age (~ 15 My), although

some evidences suggest that extension may intensified during the Pliocene (~ 5 My) (Westaway, 1994b). This extension are attested by the creation of deep basins (Mascle & Martin, 1990), the exhumation of metamorphic core complexes mostly in the Cyclades islands, the crustal thinning, and the existence of major active crustal faults in the whole Aegean. If back arc extension predates the initiation of the NAF as hypothesized *(*Angelier et al., 1982; Armijo et al., 1996), it is at least plausible that the southern Aegean was extended prior to NAF deformation propagation into the north Aegean. This earlier mode of extension was greatest in the Sea of Crete where it reaches a factor of two (McKenzie, 1978; Angelier et al., 1982), and it is responsible of the curvature of the Hellenic arc. This extension is consistent with paleomagnetic rotations of rock units in the opposite sense observed on the east and west sides of the Aegean (e.g. Kissel & Laj, 1988). Unlike the present episode of deformation, the North Anatolian Fault was not involved in this earlier deformation. This earlier episode of deformation was discontinuous both in time and space (Mercier et al, 1989). Propagation of the NAF into the north Aegean concentrated the more recent (~ 5 My) phase of extension in the northern Aegean and in the Gulf of Corinth, leaving the southern Aegean to translate SW as a coherent unit. The relatively young age inferred for the Gulf of Corinth ~ 1 My (Armijo et al., 1996) is consistent with this scenario.

The Cretan Basin that is the most aseismic area in the region possibly had been stretched parallel to Hellenic arc. However, possible collision of the Hellenic arc with the African promontory might stop further stretching of the Cretan basin. After that event, the Aegean region underwent a new stage of the extensional regime or the second stage of extension is related to the combined effects of the still active migration of the African slab and of the westward migration of Anatolia. There is no doubt that the strain has varied spatially over extensional time (e.g., McKenzie, 1978; Mercier et al., 1989; Le Pichon et al., 1995).

2.3 Seismicity

The Aegean region is one of the most seismically active areas in the world (e.g., McKenzie, 1972, 1978; Mercier et al., 1977; Jackson et al., 1982; Armijo et al., 1996). The scatter in the seismicity of the Aegean region is not due to errors in the location of epicenters, which are usually less than 30 km. Figure 2.6 shows that earthquakes are not homogeneously distributed over the Aegean but are primarily located around the Hellenic Trench and western Greece and therefore related either to the active subduction process or to the continental collision with Apulia. Earthquakes are also loctaed in the north Aegean Sea and related to the north Anatolian fault.

Most of the seismic energy release from the north Aegean Sea. The released seismic energy is not homogeneous over the Aegean. The largest is in the north Aegean Sea, where several earthquakes with magnitude greater than 7 have been occurred since the beginning of the 19th century (Ambraseys and Jackson 1990). The less energy is in the Sea of Crete, where only one earthquake of magnitude 7 has been occurred. This difference in seismicity is also observed in the historical seismicity records. The present shallow seismicity is concentrated in two diffuse belts along the Hellenic trench and in the northern Aegean (Galanopoulos, 1967; Caputo et al., 1970; Ryan et al., 1969; McKenzie, 1970, 1972; Papazachos & Comninakis, 1971). The Hellenic trench and volcanic arc are seismic regions that contain a broad belt in which seismic activity has occurred at both shallow and intermediate depths (Fig. 2.6). Graben like basins in Greece are also dominated by high seismicity and large earthquakes (Ms = 5.5) (Ambraseys & Tchalenko, 1970).

As Figure 2.6 shows, the Hellenic trench elongation can be identified on a seismicity map as a curved shape. Most of the seismicity stops abruptly about 40 km from the trench. The highest concentration is seen in the western part of the Peloponnesus. Some clusters are located where there are changes in the morphology of the Hellenic trench (Hatzfeld et al., 1989).

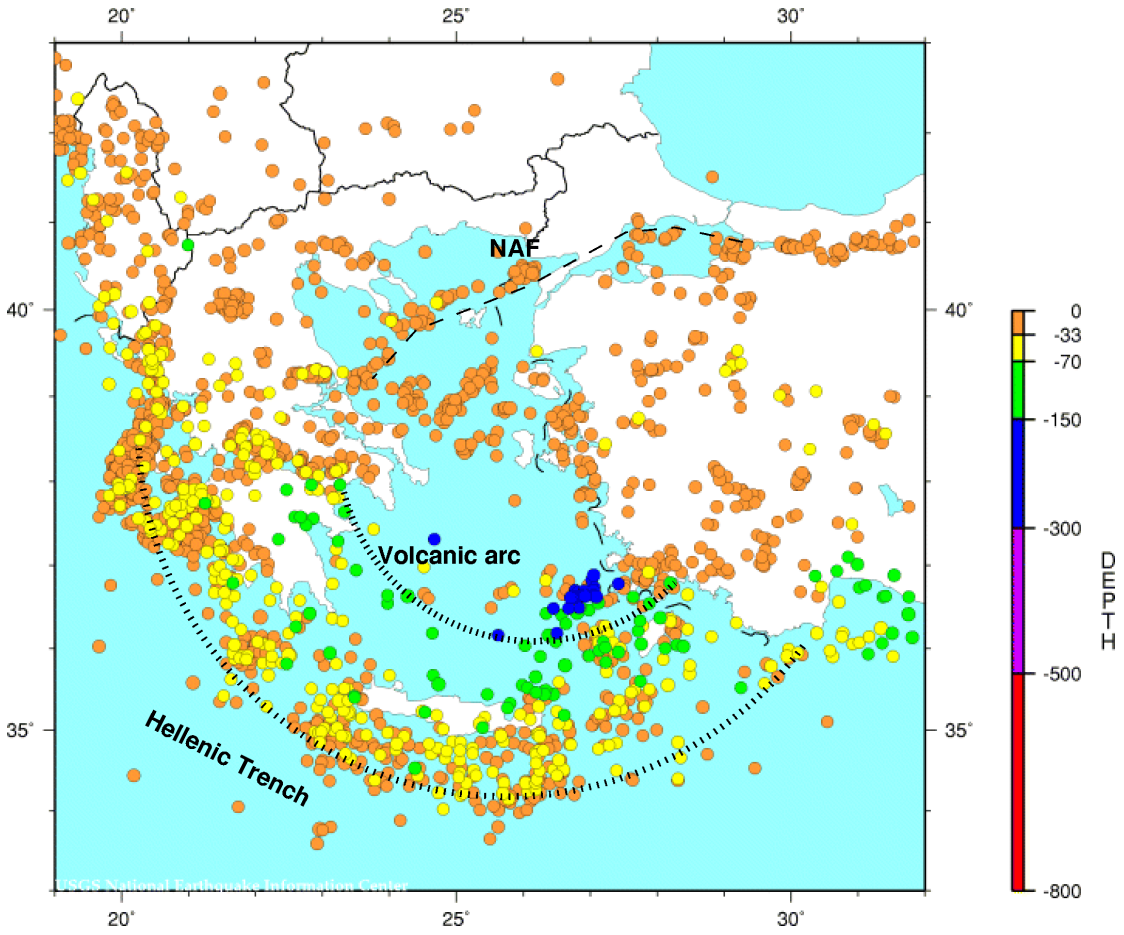

Fig. 2.6. Seismicity in the Aegean area (mb > 4.5, 1973-2005, NEIC catalogue). Earthquakes are mostly located either along the Hellenic trench and western Greece associated with the subduction process and continental collision, respectively or in the north Aegean Sea related to the north Anatolian fault system. The deepest earthquakes occur in SE Aegean in the depth of 180 km.

The 100 km and 150 km isodepth contours of hypocenters of earthquakes are not parallel to the Hellenic arc (Hatzfeld & Martin, 1992) and show that the gently dipping part of the slab is longer in the west than in the east (Hatzfeld & Martin, 1992; Papazachos, 1990). In other parts of the world, convergent-plate tectonic environments similar to that of the Hellenic arc have produced earthquakes of magnitude 8 and larger.

The Cyclades islands and southern Aegean area are observed almost strain-free. There is also low seismicity in this area, although intermediate-depth earthquakes (depths greater than 50 km) occur within the subducting Africa plate beneath central Greece,

SE Aegean and Cyclades Islands. The seismicity map shows that the most intermediate-depth earthquakes occur in the southeastern part of the Aegean.
Reverse faulting is observed from focal mechanisms of earthquakes along the Hellenic arc, on the other hand, in the internal part of the arc normal faulting is obvious (Hatzfeld et al., 1990). The transition between reverse faulting and normal faulting is rather sharp, but with some overlap of the two families (Hatzfeld et al., 1990). Intermediate microseismicity determined by Hatzfeld et al. (1989) also defines a subducted slab dipping gently (10º) towards the northeast for the first 200 km and dipping more steeply (45º) beneath the Cyclades. These results are consistent with the seismicity obtained by a careful selection of well defined events (ISC data) by Martin (1988).

2.4 Previous geophysical studies

The lithospheric structure in the Aegean area has been the focus of many intensive geological and geophysical studies. Due to the tectonic complexity in this area, which includes the subduction of the African plate beneath Aegean as well as the internal extension within the whole Aegean, studies are generally divided into two main parts. One of them concentrates on the structure of the continental Aegean plate, while the other deals with the oceanic lithosphere of the subducted African plate.

2.4.1 The continental Moho of the Aegean plate

Due to the geodynamic evolution of the Aegean area, the crustal thickness undergoes strong variations. This variations determined to be over a range of 15-25 km beneath the back-arc basin (Aegean Sea) to 40-60 km beneath the orogenic belts (mainland Greece)(e.g., Alessandrini et al., 1997). In Table 2.1, brief information is given about crustal thickness in various parts. In general, the continental lithosphere thins from the north to south (Makris, 1978a,b).

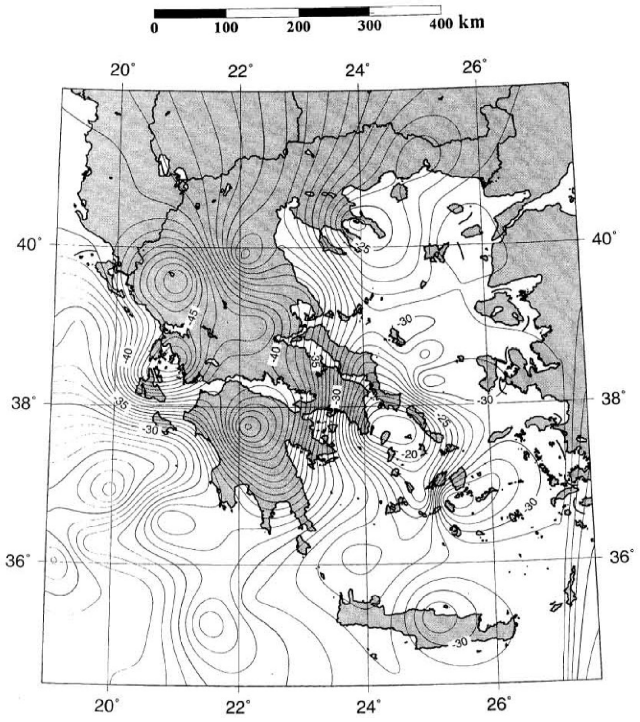

Fig. 2.7. Moho depth map obtained from gravity data by Tsokas & Hansen (1997).

After a deep seismic sounding study of Makris (1973), it is clearly understood that the crust in Aegean region is continental but thin. Results from seismic refraction experiments (Deep Seismic Profiles - DSP) were presented in a series of papers by Makris (1973, 1976, 1978). Makris in his pioneering work, proposed an average crustal thickness for the Aegean and the Hellenides mountain range that varied between 30 and 44km, respectively, whereas for the southern Aegean (Cretan sea) between 20 and 25km and less than 20km for the Ionian Sea. Makris (1977) also compiled the first map of the Mohorovic discontinuity depth in the broader Aegean area by combining data from these seismic experiments with gravimetric data. Similar results were also obtained from DSP data by Makris & Stobbe (1984), Delibasis et al. (1988), Bohnhoff et al. (2001) and Clément et al. (2004). These results were also confirmed later by travel time analysis from local and regional earthquakes (Panagiotopoulos & Papazachos, 1985; Papazachos, 1994; Papazachos et al., 1995).

Maps of the Moho topography derived from gravity data imaged the variations of the crustal thickness in the area of Greece and Aegean Sea (Lepichon & Angelier, 1979; Makris & Stobbe, 1984; Tsokas & Hansen, 1997; Tiberi et al., 2001; Tirel et al., 2004). The more complete Moho map including Aegean, Greece and the island of Crete was obtained from gravity data along six profiles within Aegean by Tsokas & Hansen (1997). They estimated the mean crustal thickness for the area of Greece to be 32 km, whereas it thins to 20 km and 25 km in the central Aegean Sea and north Aegean region, respectively. Their results showed the thickness of 40-49 km beneath the Hellenides in western Greece (Fig. 2.7).

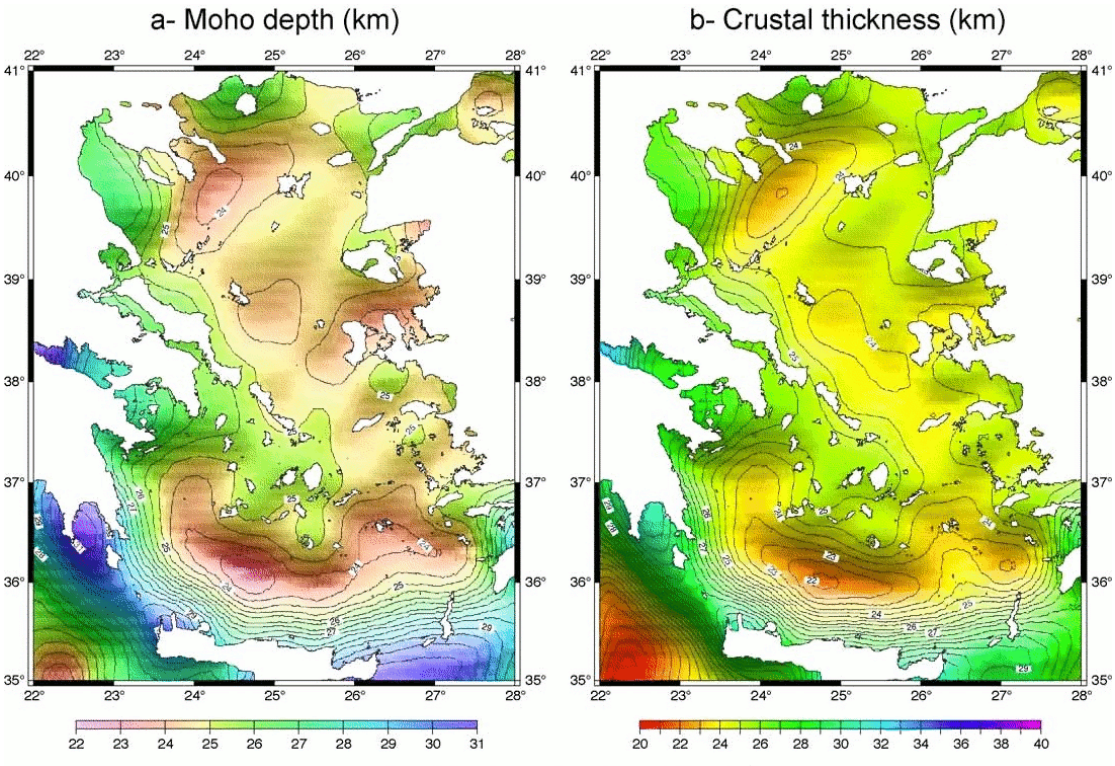

Fig.2.8. Moho depths and crustal thicknesses in the Aegean region deduced from gravity inversion by Tirel et al. (2004).

The more recent work of Tirel et al. (2004) inferred from gravity inversion across the Aegean Sea revealed a homogeneous and relatively thin crust about 25 km in this region, with variations of only +2 km near continental Greece and Anatolia, and -2

km across the North Aegean trough and Cretan Sea (Fig. 2.8). The most homogeneous image of the Aegean velocity structure is deduced from tomographic studies (Spakman, 1986, Christodoulou & Hatzfeld 1988, Spakman et al., 1988; Ligdas et al., 1990; Drakatos & Drakopoulos 1991; Ligdas & Main 1991; Ligdas & Lees 1993; Spakman et al., 1993; Papazachos et al., 1995; Papazachos & Nolet, 1997; Karagianni et al., 2003, 2005). Karagianni et al. (2005) used the Rayleigh wave group velocities to infer a 3-D tomographic image of the shear wave velocity structure of the crust and upper mantle in the Aegean Sea using regional events (Fig. 2.9). This work is complemented with a group and phase velocity study at longer period using teleseismic events (Bourova et al., 2005).

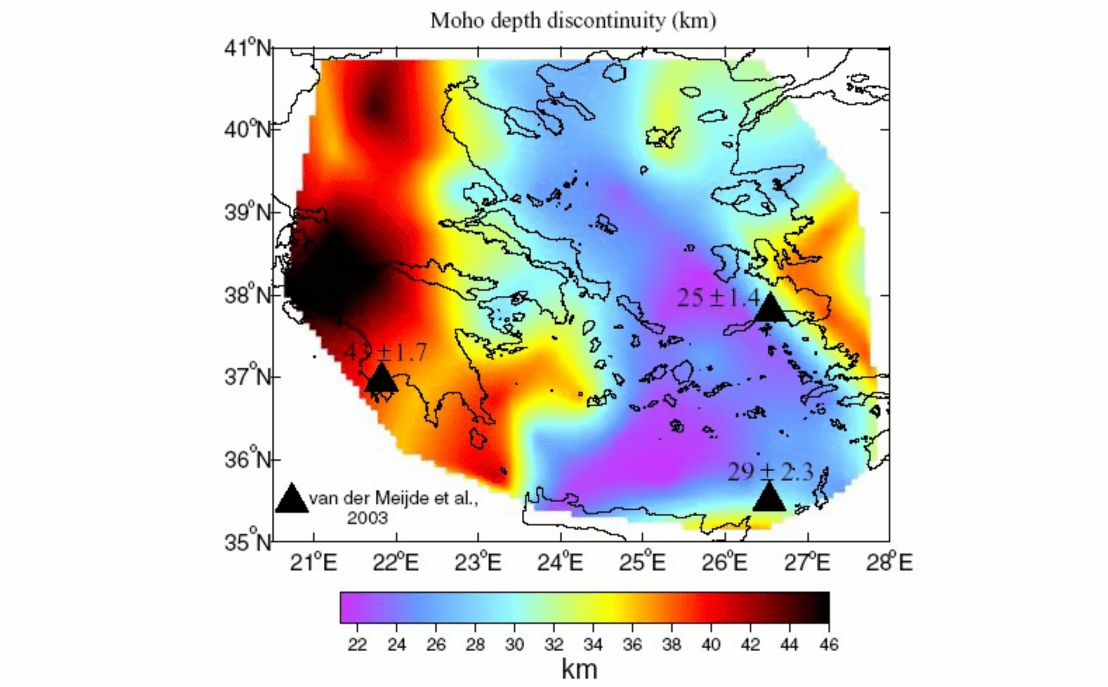

Fig. 2.9. Moho depth map estimated from dispersion of Rayleigh wave group velocities by Karagianni et al. (2005).

They found different crustal thicknesses in the Aegean Sea and Greece, which are in agreement with the general characteristics estimated from previous works in this area. According to their works, a thick crust (40-45 km) has been found for the western Greece and the Peleponnesus along the Dinarides-Hellenides mountain range, while in

Tabel 2.1. Moho depths obtained from previous works in the Aegean region.

Authors	Method	Crete	Cretan Sea	Cyclades	North Aegean	Greece	Hellenides
Papazachos (1966)	seismic wave velocity	-	-	20-35	33	-	43
Makris (1975) (1976)(1977)	deep seismic sounding and gravimetry	30-32	20	28	-	30-32	46
Makris and Vees (1977)	refraction	30-32	20	26	-	-	-
Calcagnile (1982)	surface wave dispersion	-	35	-	35	-	36-42
Panagiotpoulos et al. (1985)	earthquake seismology	-	24-30	-	-	-	30-35
Papazachos et al. (1995)	seismic tomography	30-40	25	25-30	25-30	-	35-40
Tsokas and Hansen (1997)	gravity	28-30	26	19-32	26-28	-	40-49
Tiberi et al. (2001)	gravity	-	-	-	-	25	40
Bohnhoff et al. (2001)	reflection refraction	24-32.5	15	-	-	-	-
Vigner (2002)	reflection	-	-	26-25	25	-	-
Karagianni et al. (2002)	surface wave dispersion	-	22-24	-	32	-	42-46
van der Meijde et al. (2002)	receiver function	-	29	25	-	-	43
Li et al. (2003)	receiver function	31-39	-	25	-	-	-
Tirel et al. (2004)	gravity	28-31	23	25	24-26	-	-
Karagianni et al. (2005)	surface wave tomography	-	20-22	24-26	26-32	30-34	40-46

the eastern part of Greece crustal thickness has been estimated to be 30-34 km. In the southern Aegean Sea, the crust is approximately 20-30 km thick, whereas the northern Aegean Sea exhibits a crustal thickness of about 25-30 km. The complexity of the crustal structure beneath the island of Crete, probably due to its location in the forearc of the subduction zone has been shown by many studies (Makris, 1978; Knapmeyer, 2000; Bohnhoff et al., 2001; Li et al., 2003; Endrun et al., 2004). The average crustal thickness has been estimated to be 28-30 km. Li et al. (2003) applied P receiver function method for the stations on the island of Crete and observed significant converted phase with a negative amplitude for most stations. It has been interpreted as a reversed Moho velocity contrast, caused by the hydration and serpentinization of

mantle mineral in the forearc.

2.4.2 The oceanic Moho of the subducting African plate

The dipping high-velocity zone was recognized by the early work of Spakman (1985, 1986) as the blurred image of the African slab that penetrates deep into the Aegean upper Mantle.

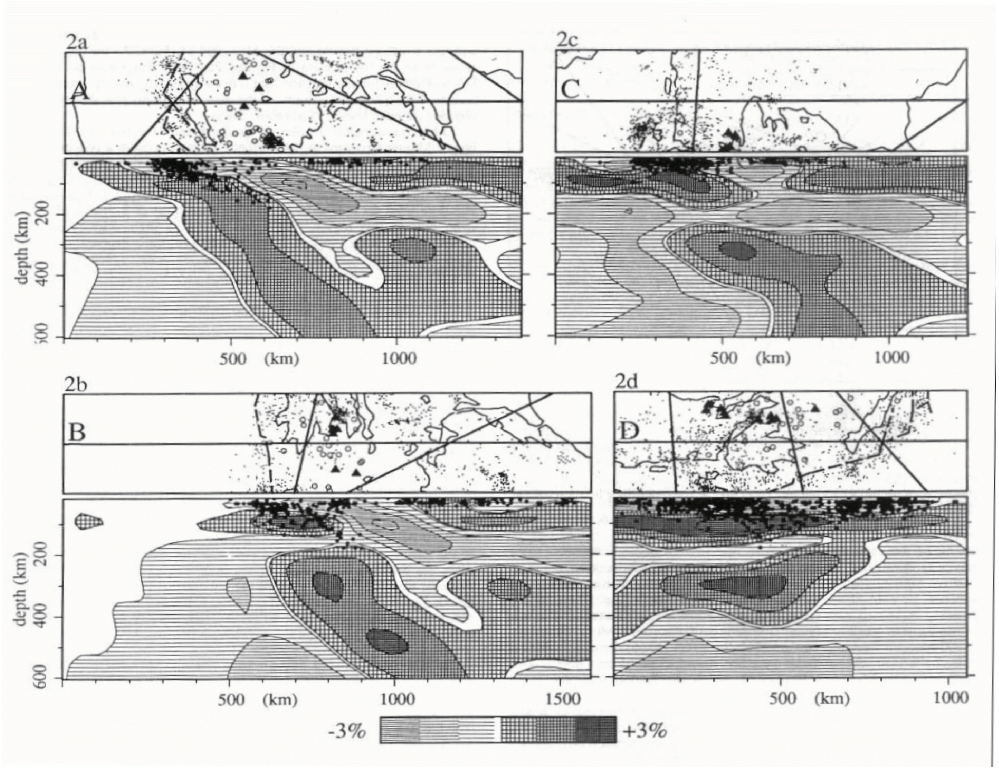

Fig. 2.10. Results of the early tomographic study in the Aegean by Spakman et al. (1988) show reliably the existence of the subducted African plate beneath Aegean to depths of at least 600 km.

Tomographic images of the Hellenic subduction zone by Spakman et al. (1988) demonstrated slab penetration in the Aegean upper mantle to depths of at least 600 km (Fig. 2.10), while the seismicity shows a maximum depth of 150-180 km. They imaged the descending slab up to northern Greece. Their results indicated a continuous slab beneath Crete. Although under Greece, on the western segment of the

subduction (approximately section of the arc which is located NW of the Kefallonia island-SW Peloponessus area), it seems to be intersected by a low velocity zone at depths around 200 km. They interpreted this zone as a level where the detachment of the lower part of the slab occurred. Papazachos et al. (1995) inverted residuals of the first P arrivals from earthquake across Aegean and showed that the velocity anomaly in the mantle under the southern Aegean extends much further and deeper to the northeast than the Benioff zone of the intermediate depth earthquakes indicates. However, Bijwaard & Spakman (1998) could image the oceanic African lithosphere up to depths of 1200 km beneath Greece. A large number of regional- or local-scale tomographic results have been also presented for several sub-regions or the broader Aegean area (e.g. Martin, 1988; Christodoulou and Hatzfeld, 1988; Drakatos, 1989; Ligdas et al., 1990; Drakatos and Drakopoulos, 1991; Ligdas and Lees, 1993; Papazachos et al., 1995; Papazachos & Nolet 1997).

Recently, Papazachos and Nolet (1997) presented new tomographic results for the P and S-wave velocity distribution in the Aegean area using non-linear inversion of travel times through 3-D ray tracing, which allowed the detailed description of the regional 3-D structure of the crust and uppermost mantle (up to ~160km).

Figure 2.11 shows the spatial distribution of P-velocities along three cross-sections, where strong crustal thickness variations and mid-crustal low velocity layers are found. Moreover, the signature of the relatively thin subducted slab in the upper mantle, as well as its detailed geometric characteristics are clearly identified. The subducted African lithosphere resolved from seismicity (Makropoulos & Burton, 1984; Papazachos, 1990; Hatzfeld & Martin, 1992) shows an unusual shape with an increasing dip from west to the east. The derived Benioff zone, which was identified through the accurate location of intermediate-depth (60km≤ h ≤180km) earthquakes, defines the boundary between the Eurasian and African lithospheric plates along the Hellenic arc.

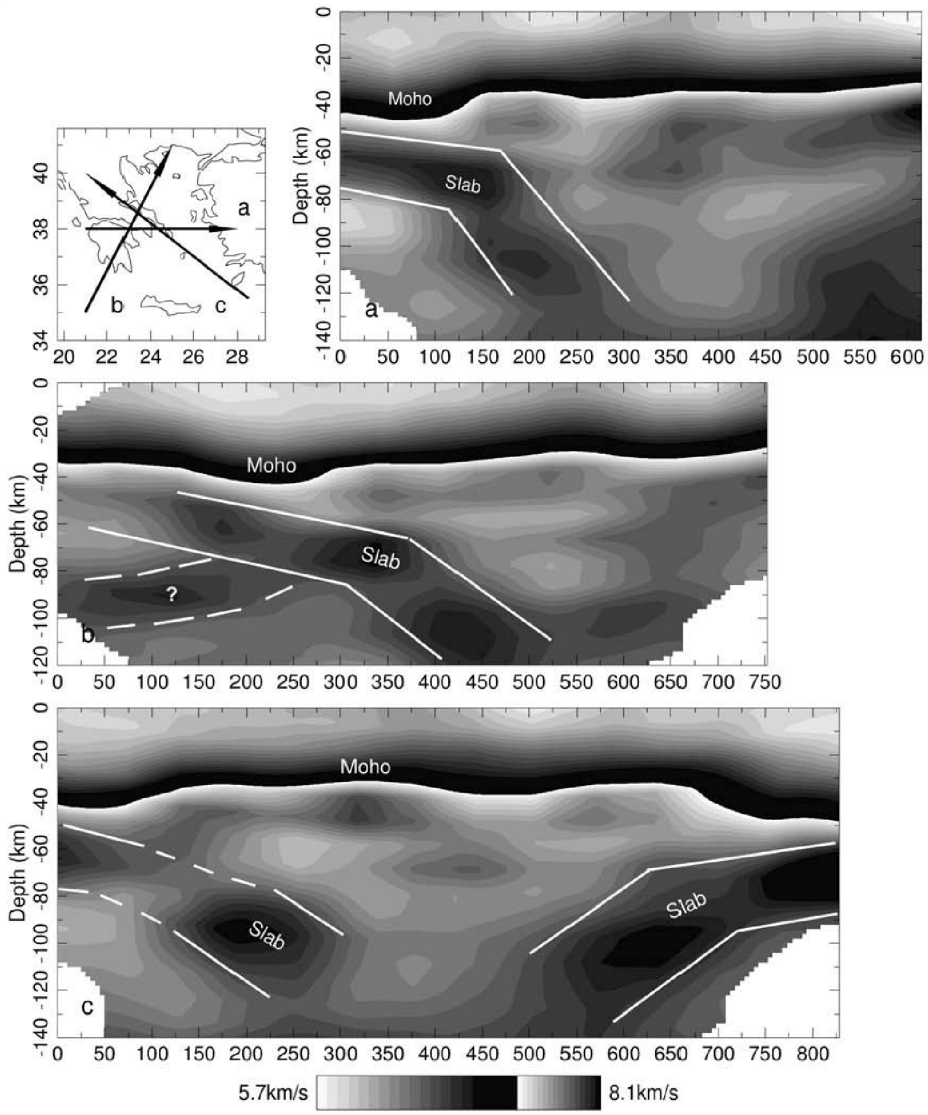

Fig. 2.11. Tomographic images of the subducted African plate along three profiles in the Aegean by Papazachos & Nolet (1997).

It has been shown that the Benioff zone consists of the shallow part (h<100km), which dips at a low angle where earthquakes with magnitudes up to 8.2 occur and of the deeper part (100km≤ h ≤180km), which dips at a larger angle where earthquakes with magnitudes up to 7.0 occur (Papazachos, 1990; Kiratzi and Papazachos, 1995; Papazachos, and Nolet, 1997; Papazachos et al., 2000). Figure 2.12 shows a map with well-located epicentres of shallow and intermediate-depth earthquakes in the southern Aegean area (Papazachos et al., 2000) as well as three cross-sections where the foci of

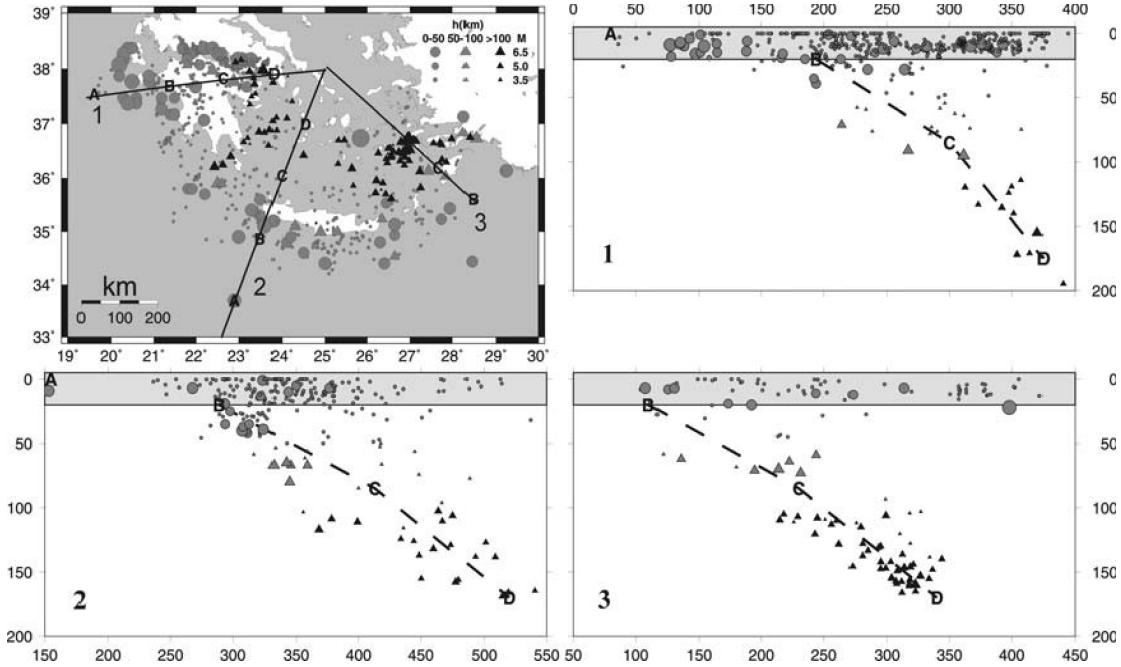

Fig. 2.12. Maps of accurate located epicenters of earthquakes in the southern Aegean Sea along three profiles shown on the top-left map by Papazachos et al. (2000).

these shocks have been projected on vertical planes (along the lines shown on the map). Receiver function analysis of the lithospheric structure in the Aegean area and Greece are more limited. The early work of Knapmeyer (2000) using P receiver functions in western Crete showed a downgoing oceanic Moho at a depth of 40-70 km, while Li et al. (2003) mapped it down to a depth of 100 km beneath Santorini island in the volcanic arc.

CHAPTER 3

In this chapter, the methods, which were applied to the data are briefly introduced.

3. Methods

Two different methods were used in this thesis to study the lithospheric structure at the study area.

3.1 P-to-S receiver function method

The teleseismic P receiver function method has become a popular technique to constrain crustal and upper mantle velocity discontinuities under a seismic station (e.g. Langston, 1977; Owens et al., 1984; Kind and Vinnik, 1988; Ammon, 1991; Kosarev et al, 1999; Yuan et al., 2000). Telesismic body waveforms recorded at a three-component seismic station contain a wealth of information on the earthquake source, the earth structure in the vicinity of both source and the receiver, and mantle propagation effects. The resulting receiver function is obtained by removing the effects of source and mantle path.

The basic aspect of this method is that a few percent of the incident P wave energy from teleseismic events at significant and relatively sharp velocity discontinuities in the crust and upper mantle will be converted to S wave (Ps), and arrive at the station within the P wave coda directly after the direct P wave (Fig. 3.1). Ps converted waves are best observed at epicentral distances between 30° and 95° and are contained

largely on the horizontal components. The amplitude, arrival time, and polarity of the locally generated Ps phases are sensitive to the S-velocity structure beneath the recording station.

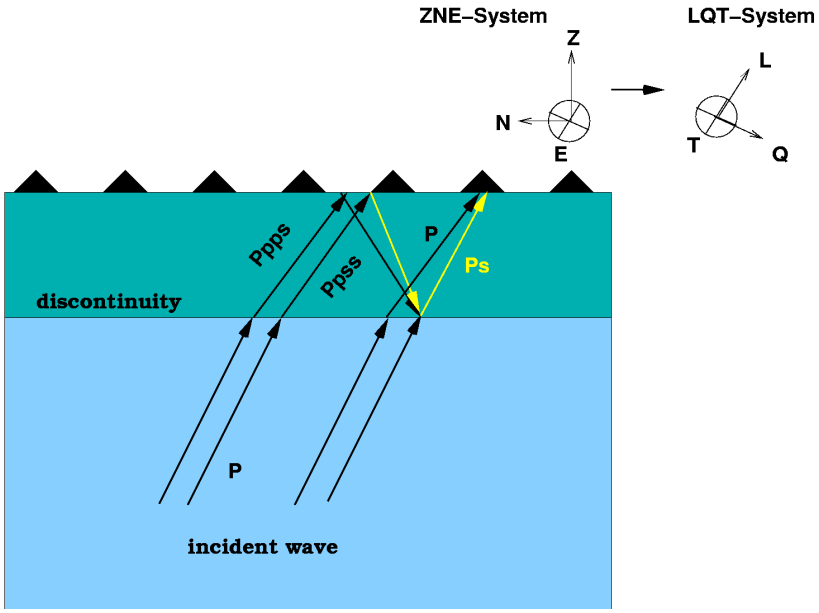

Fig. 3.1. Sketch illustrating P-S converted phase for an incident P wave from below on a homogeneous, isotropic layer with velocity V1>V2. Asides from primary Ps converted phase, two multiples (indicated by Ppss and Ppps) arriving later than Ps at the station are observed. To isolate the converted Ps wave from the direct P wave, the seismograms (ZNE) are rotated into an LQT ray-based system. The L component is in the direction of the incident P wave; the Q component is perpendicular to the L and the T component is the third component of the LQT right hand system.

By calculating the time difference in arrival of the converted Ps phase relative to the the direct P wave, the depth of the discontinuity can be estimated using a reference velocity model (in this thesis, the IASP91 reference velocity model is used). After rotating the coordinate system into a local LQT (P-SV-SH) recording system (Fig. 3.1), in which the L component is in the direction of the incident P wave, the Ps energy is mostly observed on the Q component perpendicular to the L component. The Q components (P receiver functions) contain Ps converted waves as well as related S type multiples. To obtain the P receiver function, the following steps are

generally used.

3.1.1 Restitution

Different seismographs are usually deployed to record earthquakes. Our data set(Table1, Appendix A), due to using several networks, consists of various instruments with quite different frequency responses.

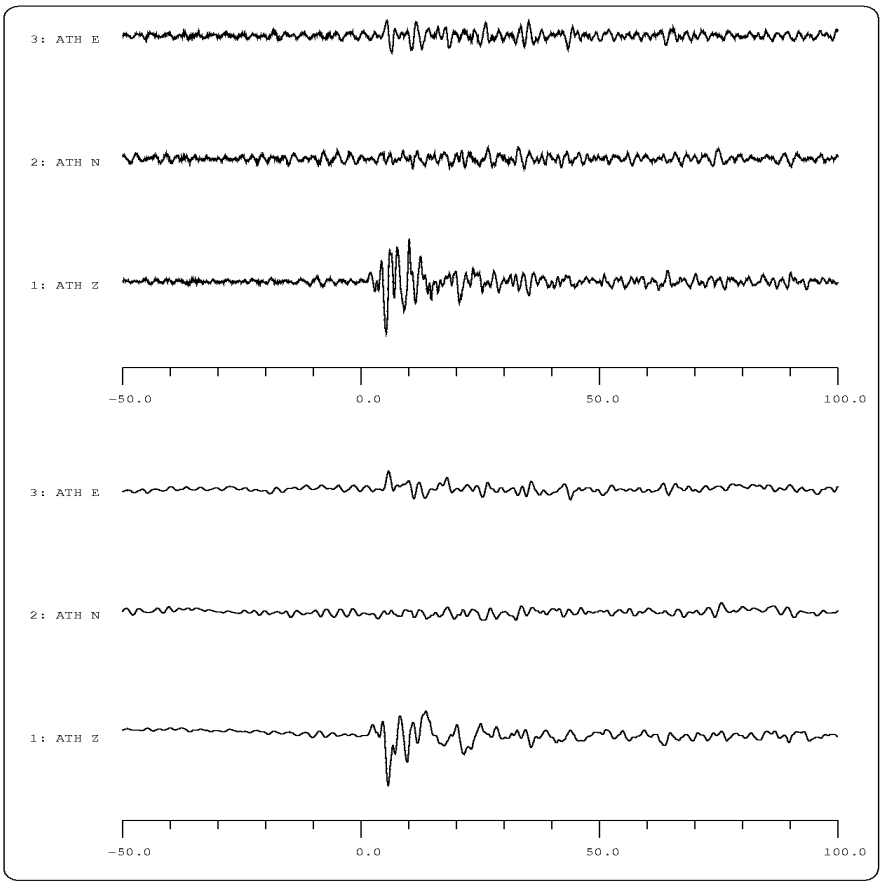

Fig. 3.2. Three components seismogram before and after restitution. The upper panel shows an original recording of the earthquake recorded at station ATH. Lower panel indicates the components after restitution of the instrument response. The P onset is assumed to be as zero time.

To utilize data recorded at different types of seismometers, the instrument responses have to be deconvolved. The main frequency range of teleseismic body waves is

between 1-0.1 Hz. Figure 3.2 shows an example of a three components record before and after restitution.

3.1.2 Rotation

Firstly, the two horizontal components N and E are rotated to radial (R) and tangential (T) directions. Most of the energy of the direct P and Ps waves are dominating the Z and R components, respectively. To isolate the converted Ps wave from the direct P wave, the ZRT components are rotated into an LQT (P-SV-SH) ray-based coordinate system, in which the L component is in the direction of the incident P wave; the Q component is perpendicular to the L component and is positive away from the source; the T component is the third component of the LQT right hand system. The L component is dominated by the P wave, while the Q and T components contain mainly the converted S wave energy (Fig. 3.3). For horizontally layered homogeneous media, the converted S wave energy is exclusively contained in the Q component. Presence of significant energy in the T component indicates dipping and/or anisotropic structure.

However, a correct estimation of the incidence angle of arriving P wave is the main requirement to perform a perfect rotation. Overestimation or underestimation of the incidence angle can result in some P wave energy on the Q component of the receiver functions at the time of direct P wave (P-onset). Fortunately, these uncertainties only affect the observed delay times of the P-to-S conversions from very shallow conversions (the first 1-2 s).

The azimuth and incidence angle of incoming P waves can be either theoretically calculated or actually measured. Theoretical back azimuth and incidence angle are calculated from the locations of the recording station and the earthquake hypocenter, and are usually used in the case of low signal-to-noise P wave signals.

If the incidence angle and azimuth of the incoming P wave are correctly estimated and the conversion phases do not originate from discontinuities dipping more than 10° (Langston, 1977), the isolating of the SV energy in the P coda is achieved and there

will be no P wave energy left on the Q and T components. Moreover, since the first onset on the Q component is the converted Ps phase from a shallow discontinuity below the surface, it is theoretically possible to detect discontinuities even at shallower depth (sediment layer) in contrast to the radial component where the direct P arrival usually covers Ps conversions from very shallow reflectors. Figure 3.3 indicates the rotated seismograms of the event shown in Figure 3.2.

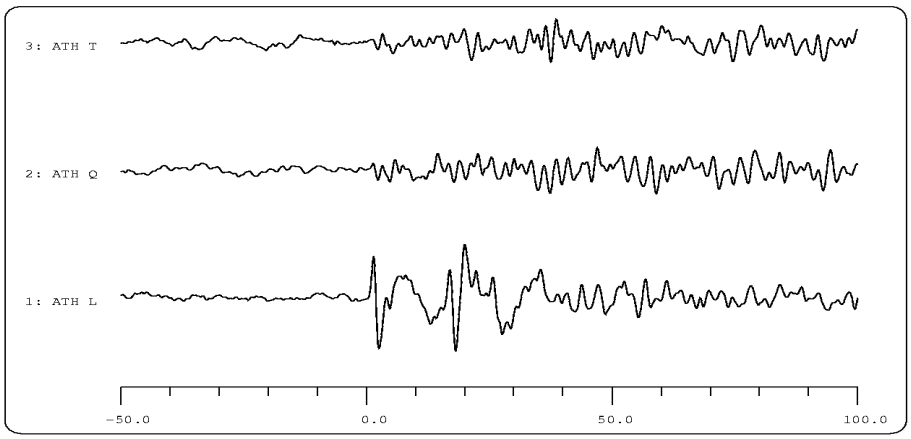

Fig. 3.3. Three components record shown in Figure 3.2 after rotation into LQT ray-based system. P waves and converted S waves dominate the L and Q components, respectively. The T component shows information about dipping or/and anisotropy.

3.1.3 Deconvolution

To eliminate the influence of the source and ray path, an equalization procedure is applied by deconvolving the Q and T component seismograms with the P signal on the L component (Yuan et al., 2000, 2002).

The resulting Q component data are named P receiver functions and are mainly composed of the P-to-S converted energy and contain information on the structure beneath a seismic station (Fig. 3.4). The arrival time of the converted Ps phase in receiver functions depends on depth of the discontinuity, whereas the amplitude of the converted phase depends on the S-wave velocity contrast across the discontinuity.

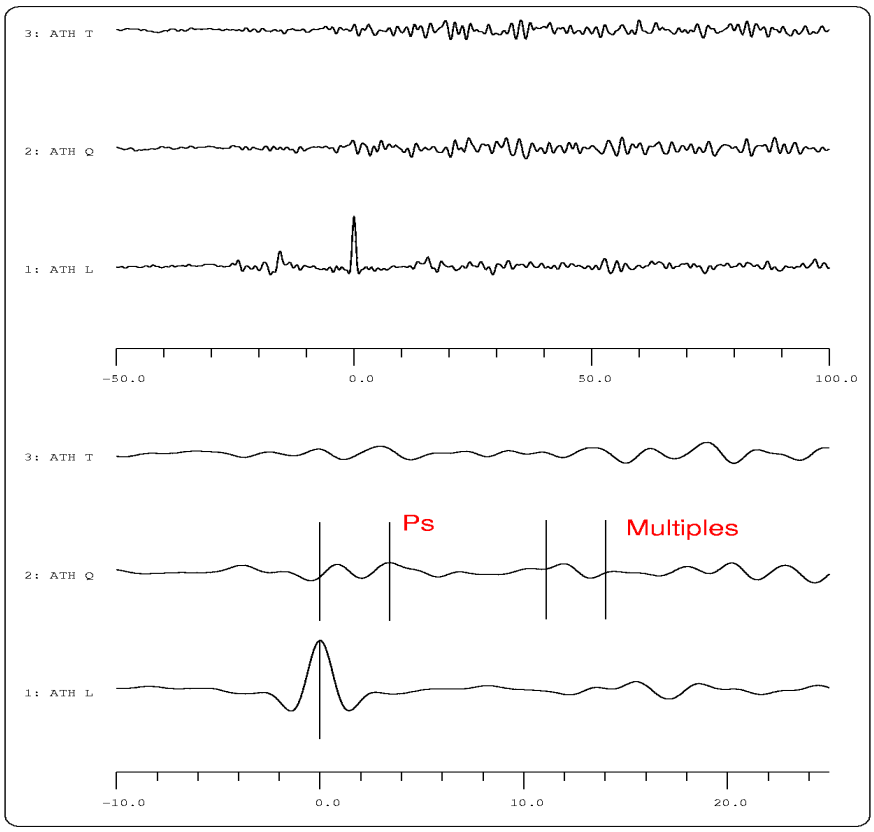

Fig. 3.4. P waveform is deconvolved from all three components. The L component indicates a spike waveform and the most converted Ps energy is contained on the Q component called P receiver function. The P onset is shifted to be as zero time. The three components are shown in the lower panel in the time window of -10-25 s. The first converted Ps phase at 3.5s represents the conversion from the Moho, while the multiples arrive at 11-14s delay time.

The final P receiver function contains, aside from the primary converted phases, multiple phases generated by each velocity discontinuity and reflected between the earth's surface and these discontinuities (Fig. 3.5). As an example, Figure 3.5 shows a simple isotropic and homogeneous model with one discontinuity at 30 km. Vs and depth values are represented in the upper panel.

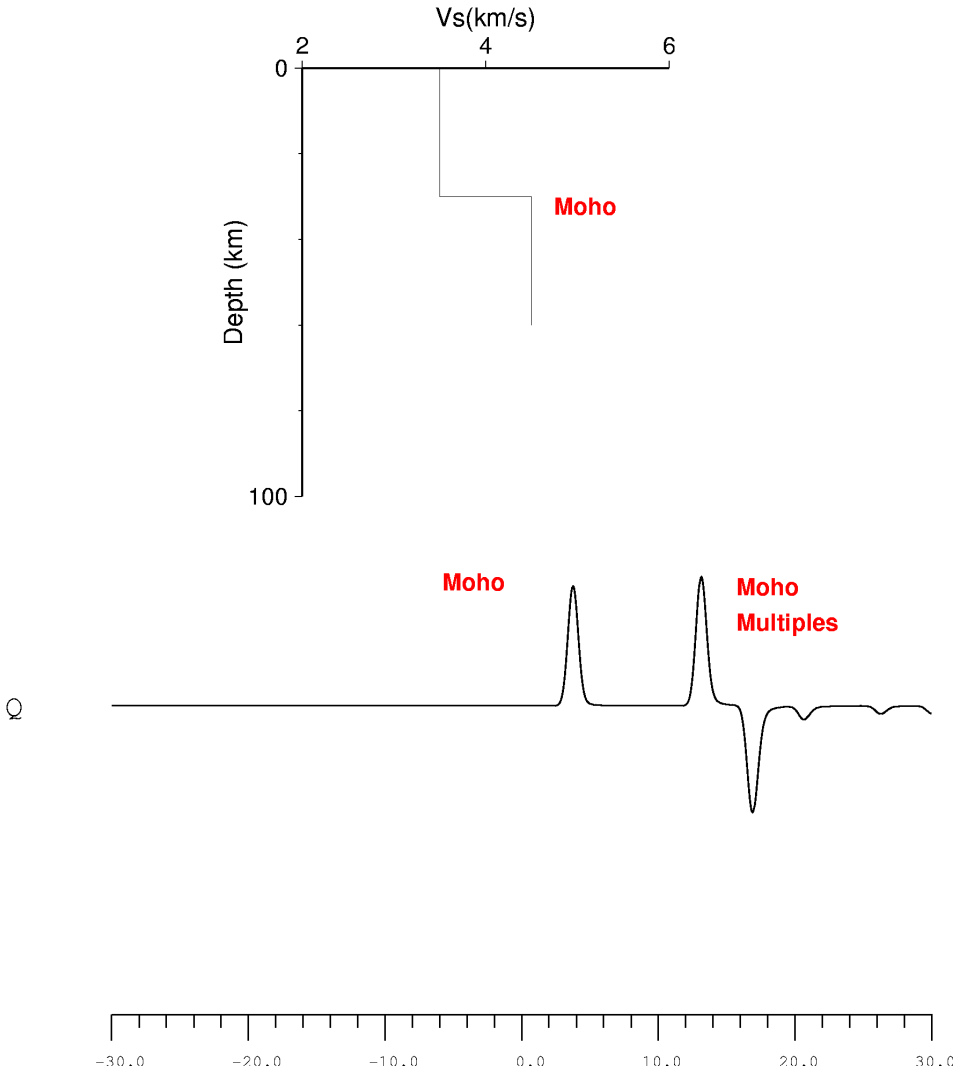

Fig. 3.5. Synthetic P receiver function produced for a layer over a half space shown in the upper panel. The Moho discontinuity lies at 30 km. The P receiver function reveals a very strong phase with positive amplitude at 3.5 s which is the converted Ps phase at the Moho. The multiples arrive at 13 s and 16 s delay time and show the Ppss and Ppps reverberations between earth's surface and the Moho.

The obtained synthetic P receiver function shows three strong phases; the first phase is the converted Ps phase from the Moho boundary at 30 km, which arrives at about 3.5 s; two other phases indicate multiples which reverberate between earth's surface and discontinuity and arrive at about 13 and 16 s delay time, respectively. Positive amplitudes in the receiver function reveal a velocity increase with depth, while

negative amplitudes indicate a velocity decrease with depth. Including multiples paths in the receiver function analysis (it they are properly identified) gives additional information about the exact depth of the Moho discontinuity and the crustal Poisson's ratio (Zandt et al., 1995; Zhu and Kanamori, 2000; Yuan et al., 2002). However, the presence of significant sediments may alter the primary Ps converted phases and make the estimation of the discontinuity depth difficult. An other problem occurs if a dipping interface changes the ray geometry or an anisotropic layer causes shear wave splitting effects. In both cases converted energy is expected to be observed on the T components. However, the major structure can be detected by analyzing the Q components. The energy on the transverse components gives additional information on the crustal heterogeneity or anisotropy (Cassidy, 1992; Levin and Park, 1997).

3.1.4 Moveout correction (distance equalization)

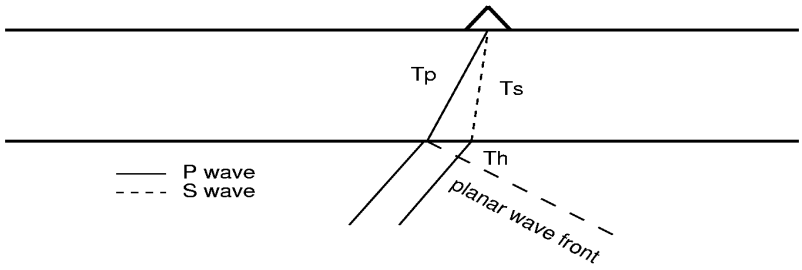

Fig. 3.6. Scheme showing the ray paths of direct P wave and converted Ps wave for a layer over a half space. Tp and Ts indicate the arrival times of P and S waves, respectively. The same ray parameter is assumed for both phases.

The converted Ps phases are usually weak and of low amplitude. In order to increase signal-to-noise, it is necessary to align and stack receiver functions from different epicentral distances at each station. However, successful alignment and constructive summation of conversion phases requires that the receiver functions be equalized in terms of their ray parameters.

For simplicity, a single layer over a half space is considered in Fig. 3.6. The ray paths

of the incident P and the converted Ps phases are also shown. Regarding to epicentral distances (>30 °), it is acceptable to approximate the incoming P waves as plane waves and accordingly formulate the Ps-P delay time as:

$$Tps - Tp = Ts + Th - Tp \qquad (3.1)$$

Assuming that the ray parameter is the same for P and Ps it can be shown (Kind & Vinnik, 1988) that,

$$Tps - Tp = h((Vs^{-2} - p^2)^{1/2} - (Vp^{-2} - p^2)^{1/2} \qquad (3.2)$$

and following the same line of argument the delay times for important crustal reverberations (multiples) are calculated as follow:

$$TPpPs - Tp = h((Vs^{-2} - p^2)^{1/2} + (Vp^{-2} - p^2)^{1/2} \qquad (3.3)$$

$$TPpSs/PsPs = 2h(Vs^{-2} - p^2)^{1/2} \qquad (3.4)$$

$$TPsSs = h(3(Vs^{-2} - p^2)^{1/2} + (Vp^{-2} - p^2)^{1/2} \qquad (3.5)$$

The conversion from crust-mantle boundary, its crustal multiples and the upper mantle 410 km and 660 km discontinuities arrive at the recording station with different slowness values (Fig. 3.7).

An approach similar to familiar normal move-out correction in exploration seismology, is taken to adjust the times of Ps conversions of all receiver functions with respect to the arrival time of the Ps conversion at a reference epicentral distance of 67° (corresponding to ray parameter of 6.4 sec/°) according to a global one dimensional velocity model (IASP91 reference velocity model).

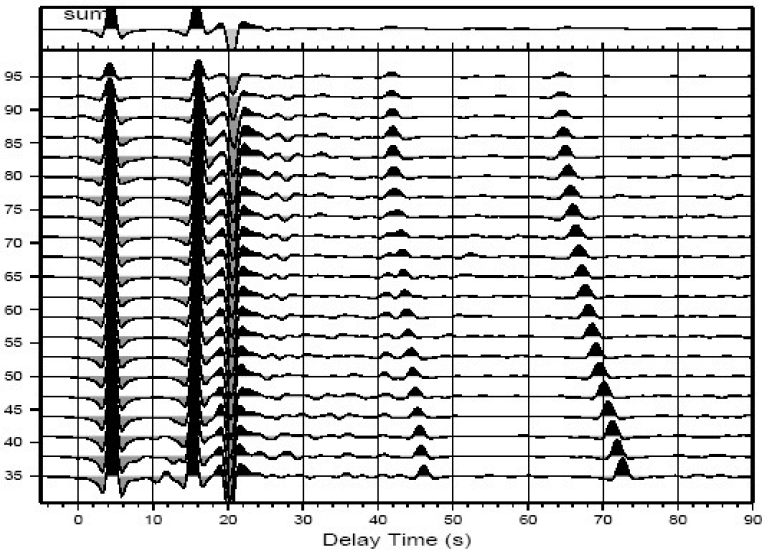

Fig. 3.7. Synthetic P receiver functions at a single station are computed using the reflectivity method. The IASP91 model is modified to contain a 40 km thick crust. Crustal Vp and Vs are assumed to be 6.5 and 3.75 km/s, respectively. Epicentral distances range between 35-95° and the focal depth is fixed at 600 km. By increasing epicentral distance, the delay times of Ps conversion decrease, while those of the multiples increase.

After correction, all direct conversions from Moho and upper mantle appear as straight lines, whereas crustal multiples become more inclined (Fig. 3.8). Stacking the moveout corrected receiver functions (for Ps) enhances the direct conversions, while the multiples are considerably weakend.

Move-out correction, as described before, can also be applied to crustal multiples. Applying the correction to each multiple and aligning the corrected seismograms by epicentral distance leads to straight appearance of the multiples whereas the direct conversions are more inclined. In this case, after correction, the multiples which have similar ray parameters appear parallel to each other.

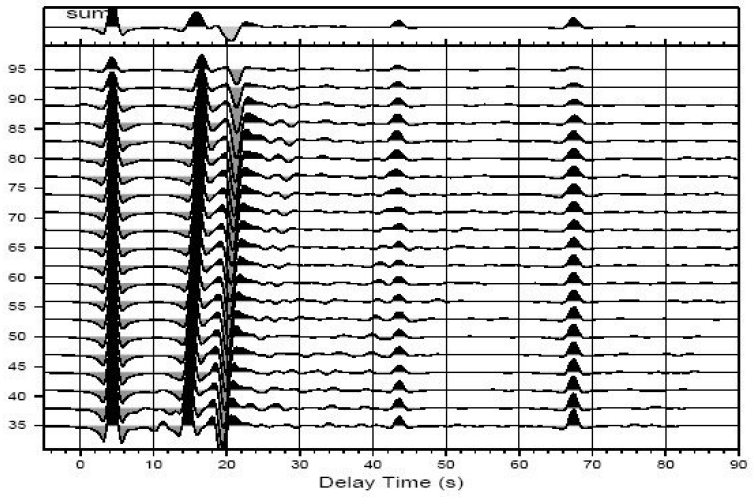

Fig.3.8. Ps moveout corrections for P receiver functions shown in Fig. 3.7. Move-out time corrections for Ps waves are applied to each sample in the receiver functions. IASP91 reference model and reference slowness of 6.4 s/ ° are used. Ps converted phases of Moho and upper mantle discontinuities at 410 and 660 km are aligned vertically, while the multiples are inclined. The summation trace in the upper panel shows the enhanced amplitudes of the primary converted phases and weakend amplitudes for multiples.

3.1.5 Migration

To improve the spatial resolution and convert the delay times into depths, the Ps amplitudes on each receiver function can be back projected along the ray path onto the spatial locations of the conversion points to their true locations in a process similar to migrating in exploration seismology (Kosarev et al., 1999)(Fig. 3.9). The ray paths are calculated using a one dimensional global velocity model (IASP91) with assumption that conversions are produced from planar interfaces. Sometimes a spatial smoothing filter is used to improve the spatial correlation so that the space is gridded and back projected amplitudes originating from adjacent boxes are stacked to improve signal to noise ratio.

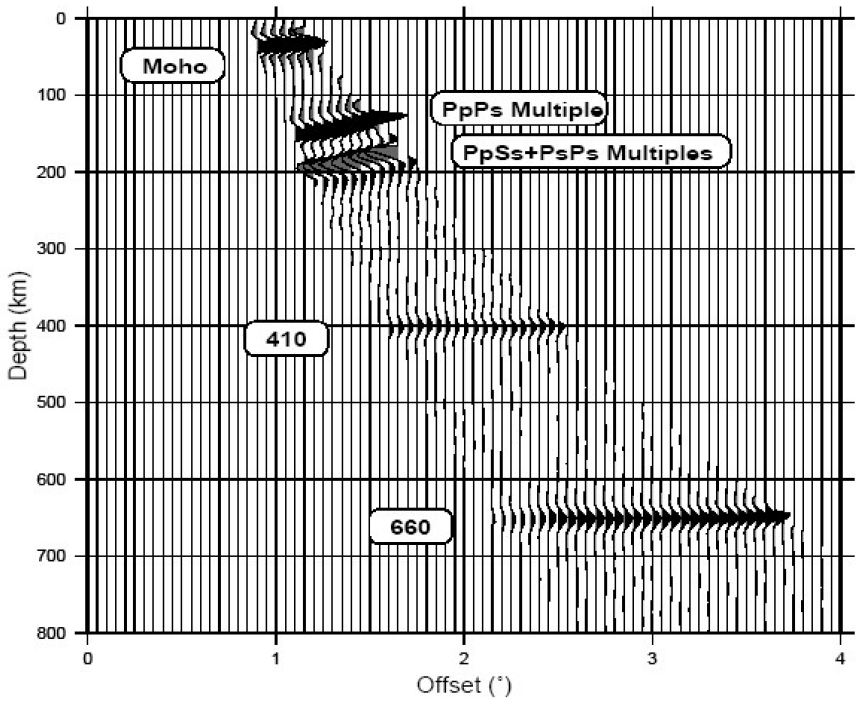

Fig.3.9. Migrated receiver functions of synthetic traces shown in Figure 3.7. Ps conversions are back-projected to horizontal images. The phases are labeled. The straight appearance of direct converted phases helps to distinguish them from oblique crustal multiples.

Applying the method to data from stations and networks where ray paths from neighboring stations, specially at large depths cross one another, improves the signal quality significantly. Besides, projection of 3-D data along desired 2-D sections can further amplify the conversion amplitudes while suppressing the reverberations due to their oblique appearance (Fig. 3.9). The technique can also be applied to reverberations of conversions and thus provide an additional possibility for detecting direct conversions.

3.1.6 Estimation of crustal thickness and Vp/Vs ratio

The converted Ps phase and crustal multiples (PpPs, PpSs and PsPs) contain a wealth of information concerning the average crustal properties such as the Moho depth and the Vp/Vs ratio.

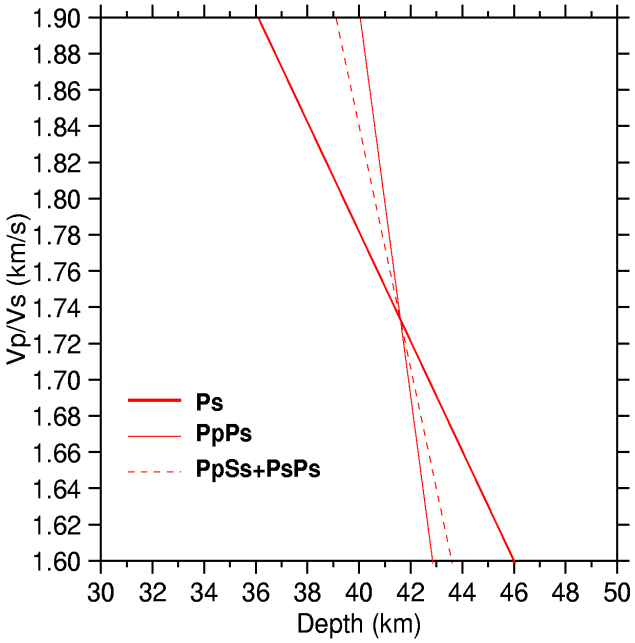

Fig. 3.10. Contributions of Ps and its multiples to the stacked amplitude as a function of crustal thickness (h) and Vp/Vs ratio.

The delay times of the primary converted Ps phase from the Moho and its crustal multiples can be used to determine the crustal thickness by a given average crustal P velocity. In presence of clear multiples, the Moho depth and Vp/Vs ratio can be computed using the stacking method of Zhu and Kanamori (2000).

This algorithm stacks the amplitudes of receiver functions at the predicted arrival time of the Moho conversion (Ps) and its multiples (PpPs and PpSs+PsPs) for various crustal thicknesses h and Vp/Vs ratios. The time domain receiver functions are then plotted by means of crustal thickness versus Vp/Vs ratio (Fig. 3.10). Regarding the higher signal to noise ratio of the primary converted phase (Ps) in comparison to its multiples, amplitudes of phases are weighted and stacked as following:

$$S(h,Vp,Vs) = w1Q(t1) + w2Q(t2) - w3Q(t3) \quad (3.6)$$

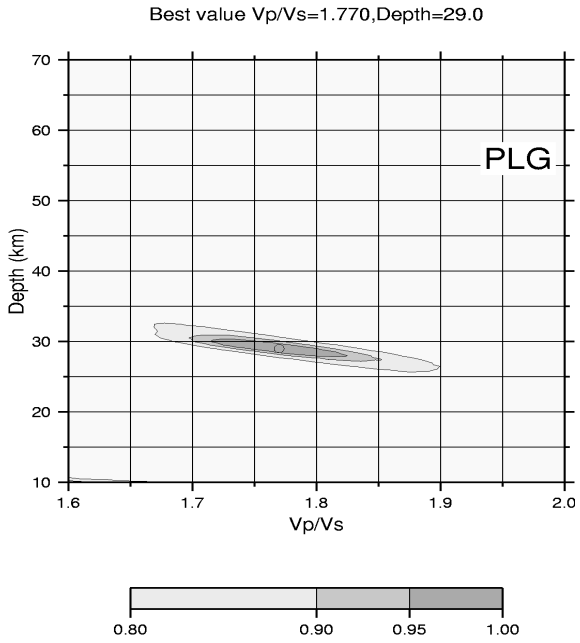

Fig. 3.11. Applying Zhu and Kanamori method for station PLG. The amplitude is shown in the lower part and ranges from 0.8 to 1. The optimal combination of the crustal thickness and Vp/Vs ratio is defined where the largest amplitude (1) occurs. The circle shows a Moho depth of 29 km and Vp/Vs of 1.77 for this station.

where Q(ti) are the receiver function amplitudes, t1, t2 and t3 are the predicted travel times for Ps, PpPs and PpSs+PsPs corresponding to crustal thickness h and Vp/Vs ratio and w shows the weighting factor for each phase. The highest weighting factor is associated with the direct conversion (w1>w2+w3), as the slopes of crustal multiples are very similar. The function S(h,Vp,Vs) reaches a maximum when all three phases (Ps,PpPs and PpSs+PsPs) are stacked coherently. The obtained h (crustal thickness) and Vp/Vs ratio are also considered as the best combination underneath the assumed station if the multiples are clear enough. As an example, Fig. 3.11 indicates the computed crustal thickness and Vp/Vs ratio for station PLG.

3.2 S-to-P receiver function method

Although P-to-S receiver function analysis has become a routine method to detect the Moho and upper mantle discontinuities underneath a seismic station, S-to-P receiver function technique is still not developed.

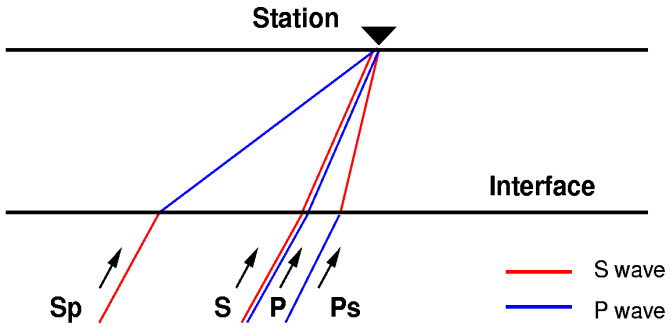

Fig. 3.12. Ray paths of Sp and Ps converted phases.

The P receiver function technique looks for the P-to-S conversions at seismic discontinuities beneath stations, while S receiver function analysis searches for the S-to-P conversions at the seismic discontinuities.

A Sp phase is generated when an incoming S phase crosses a velocity discontinuity beneath a seismic station and is converted to the P wave (Fig. 3.12). For a particular station, the converted Sp phase arrives earlier than the direct S phase (e.g. Faber and Müller, 1980; Bock, 1991; Farra and Vinnik, 2000; Li et al., 2004 ; Kumar et al., 2005). Converted Sp phases from shallow discontinuities (like crust-mantle and lithosphere-asthenosphere boundaries) are best observed at epicentral distances between 60-85° (Faber and Müller, 1980). In the case of larger distances (larger than 85°), SKS phases arrive earlier than S waves and these converted phases have to be considered.

The method used to compute P receiver functions can be also performed for S receiver functions. This method includes coordinate rotation and deconvolution. Similar to the P receiver function technique, the Q component is perpendicular to the L component, which is located in the direction of the incident S wave. It is positive away from the source. The sign of the receiver function amplitude is also related to the velocity contrast. Positive amplitudes show velocity contrasts with velocity increasing downwards, while negative amplitudes showing that the velocity decreases with depth. S receiver functions are much noisier than P receiver functions primarily because they arrive after the P wave. They also have longer periods in comparison with the P receiver functions and do not resolve the fine structure within the crust and mantle lithosphere. However, they are precursors to S waves, whereas all the multiple reverberations appear later than S. This advantage, that they are free of multiples enables them to separate the primary converted phases from the disturbing multiples, which are not more visible. The boundaries, which are normally covered by multiples arriving at nearly the same time in the P receiver functions, can also be identified in the S receiver functions.

Fig. 3.13 demonstrates a simple two layered model over a half space containing crust-mantle and lithosphere-asthenosphere boundaries at about 30 and 125 km, respectively. The synthetic P and S receiver functions are computed and compared. The P onset (for P receiver function) and S onset (for S receiver function) are fixed to be on zero. While Ps converted phase arrives later than direct P phase, the converted Sp phase is precursor of direct S wave and arrives earlier. As Figure 3.13 shows, all multiples arrive after direct S wave, therefore they can not disturb the major conversions. The computed P receiver function shows the converted Ps phase at Moho as well as its multiples. The converted phase from lithosphere-asthenophere boundary is covered by the multiples arriving at the same time on the P receiver function, even though this boundary is significantly observed on the S receiver function at 13 s (reversed time). Assuming the same ray parameter, the arrival time of the converted Sp phase at Moho is similar to that of P receiver function but in the reversed time (3.5 s). Different sign of the S-to-P conversion coefficients relative to those of P-to-S

conversion makes a reversed polarity for Sp converted phase.

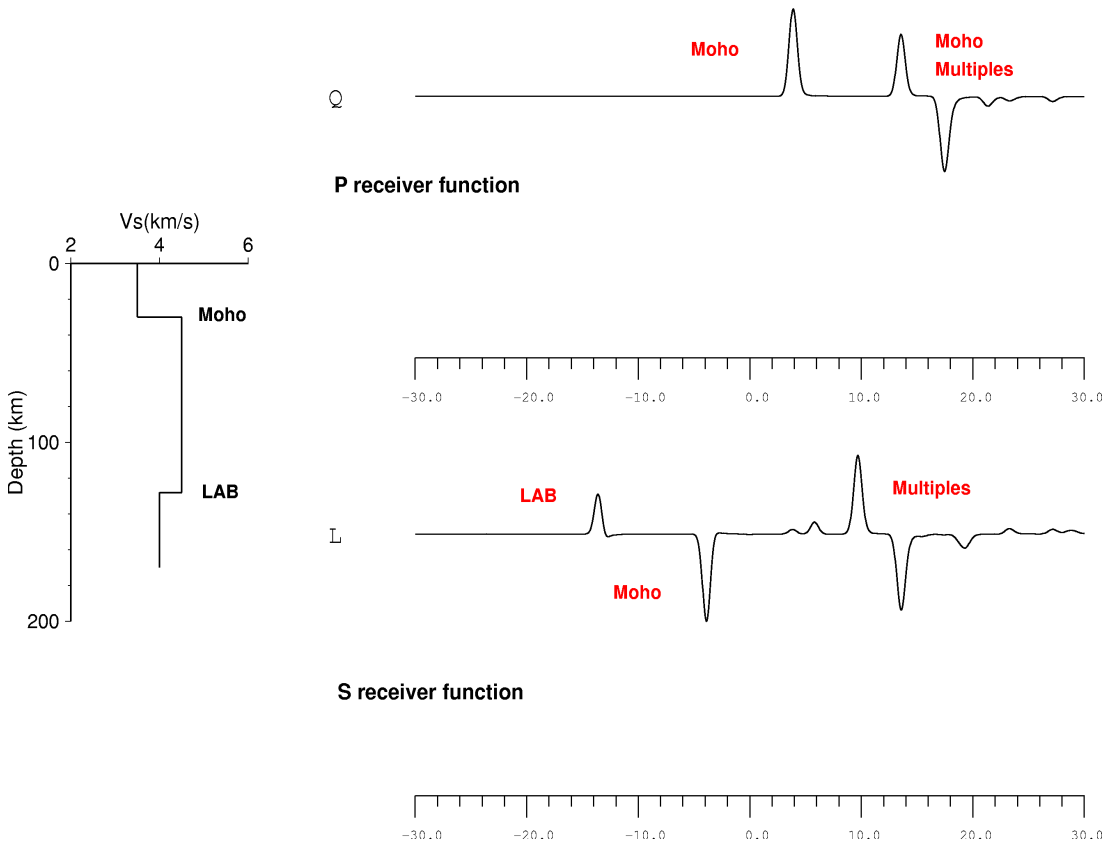

Fig. 3.13. Synthetic P and S receiver functions are computed for a two layered model over a half space shown in left part of the Figure. Two discontinuities are defined in the model as crust-mantle and lithosphere-asthenophere boundaries at 30 and 125 km, respectively. The S velocities are considered to be 3.5 km/s in the crust and 4.5 s in the upper most mantle. The P onset for P receiver function as well as S onset for S receiver function are fixed to be as zero time. P receiver function significantly reveals the Ps conversion and its multiple phases from the Moho, while the lithosphere-asthenosphere boundary (labeled with LAB) is masked by the crustal multiples. In contrast, S receiver function reliably shows the Sp converted phase from the Moho as well as that from the LAB. Sp phases arrive earlier than direct S waves, whereas all the multiples appear later. With this advantage the S receiver function separates the primary converted phases from disturbing multiples. The polarity of the Sp converted phase is reversed due to the different sign of its conversion coefficient comparing to that of Ps.

3.2.1 Lithphosere-asthenosphere boundary

The Earth's tectonic plates constitute the lithosphere so no proper understanding of plate tectonics can be achieved without reference to the lithosphere, and this requires an understanding of its essential difference from the asthenosphere. The lithosphere is generally divided into two different parts. The crust lithosphere includes the upper part of the lithosphere, whereas the mantle lithosphere located in the lower part moves as the high velocity lid on the top of the asthenosphere. High viscosity lithospheric plates moving over a lower viscosity asthenosphere is one of the basic aspects in studying plate tectonics. Observations of low seismic velocities in the upper mantle are generally associated with the lithosphere-asthenosphere boundary named LAB. This boundary appears as a negative contrast in which the seismic velocities decrease with depth. In contrast to the Moho depth which is usually observed at high resolution by different techniques such as P receiver function method, the lower boundary of the mantle lithosphere is generally considered not sharp enough to be well observed by seismic body wave observations. The thickness of the lithosphere has been mostly obtained from low resolution surface wave observations. The lithosphere has a global average thickness of 80-100 km, ranging between zero and 200 km beneath mid ocean ridges and stable cratons, respectively. However, the recently developed S receiver function technique (Li et al., 2004; Kumar et al., 2005) can be optimally used to identify the LAB boundary using higher resolution body waves, since this method is free of multiples. This boundary is almost invisible in the P receiver functions due to the crustal multiples, which arrive at the same time and heavily disturb the time window of the LAB arrival.

3.2.2 Processing

The new S receiver function technique complements the well known S-to-P receiver function method and adds only some new steps in its processing. The first step to

apply the S receiver function method is to collect the suitable events with magnitude larger than 5.7 and epicentral distances between 60-85°, which show a clear S wave. Figure 3.14 shows an event recorded at a three components broadband station. The arrival time of S wave can be clearly identified on the horizontal components (N,E). The seismograms can be also restituted, like in P receiver function technique, to have the same frequency response.

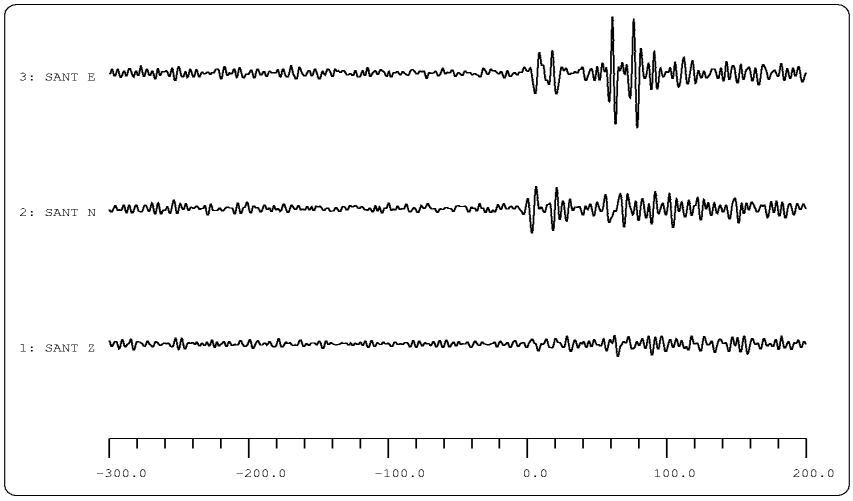

Fig. 3.14. Restituted three components seismogram shows a clear S arrival time on the horizontal components. The S onset time is shifted to be on zero.

3.2.3 Rotation

Similar to P receiver function method, the two horizontal components (N,E) are firstly rotated around the theoretical back azimuth to the radial and tangential directions (R,T). In the next step, the components are rotated into the LQT (P-SV-SH) system, as described in P receiver function method. However, rotation around the incidence angle in S receiver functions is even more important than in P receiver functions. A very accurate procedure has to be performed to choose the correct incidence angle. For this aim, a subroutine was used, which rotates components with a series of incidence angles.

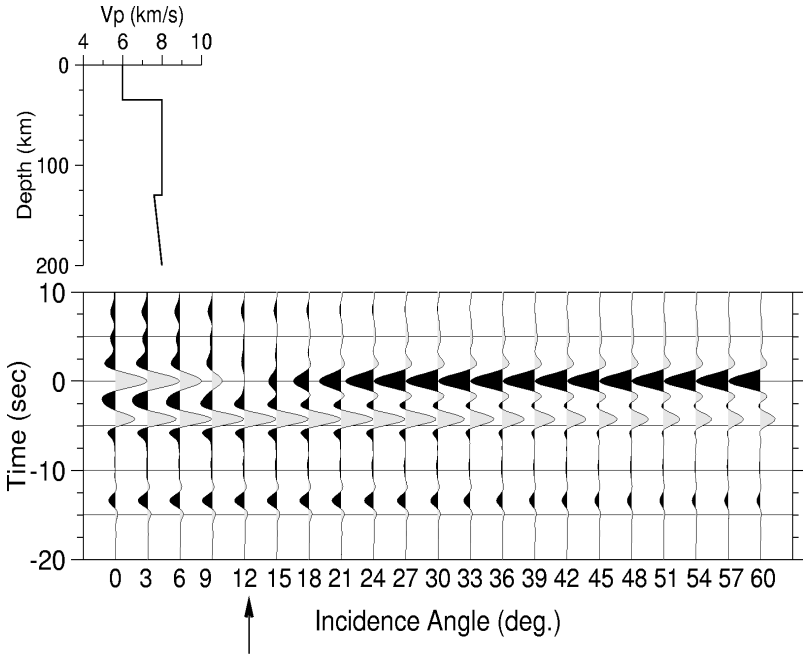

Fig.3.15. Determination of the incidence angle for synthetic seismograms for the shown model by rotating the vertical and radial components around the incidence angle. The synthetic seismograms are computed using reflectivity method for a simple model shown at the top. S receiver functions have been computed using different incident angles ranging between 0-60°. The theoretical incidence angle agrees well with the observed one (shown with arrow). The amplitude at the S arrival time (zero time) changes sign at that angle.

The method aims at having the least energy on the L (P) components at the time of S arrivals (S-onset). Figure 3.15 shows a simple model consisting of two discontinuities, a positive contrast at 30 km (Moho) and a negative contrast at 130 km (LAB). The synthetic seismograms have been generated using the reflectivity method (Kind, 1985) and the S receiver functions have been computed using different angles of incidence ranging between 0-60°. The lower panel shows the L (P) components obtained from various rotations. The deconvolution has also been applied to the L components (described in the next part). As the figure shows, the amplitude at the S arrival time (zero time) changes sign. The best incidence angle is chosen, where the minimum energy is observed on the zero time.

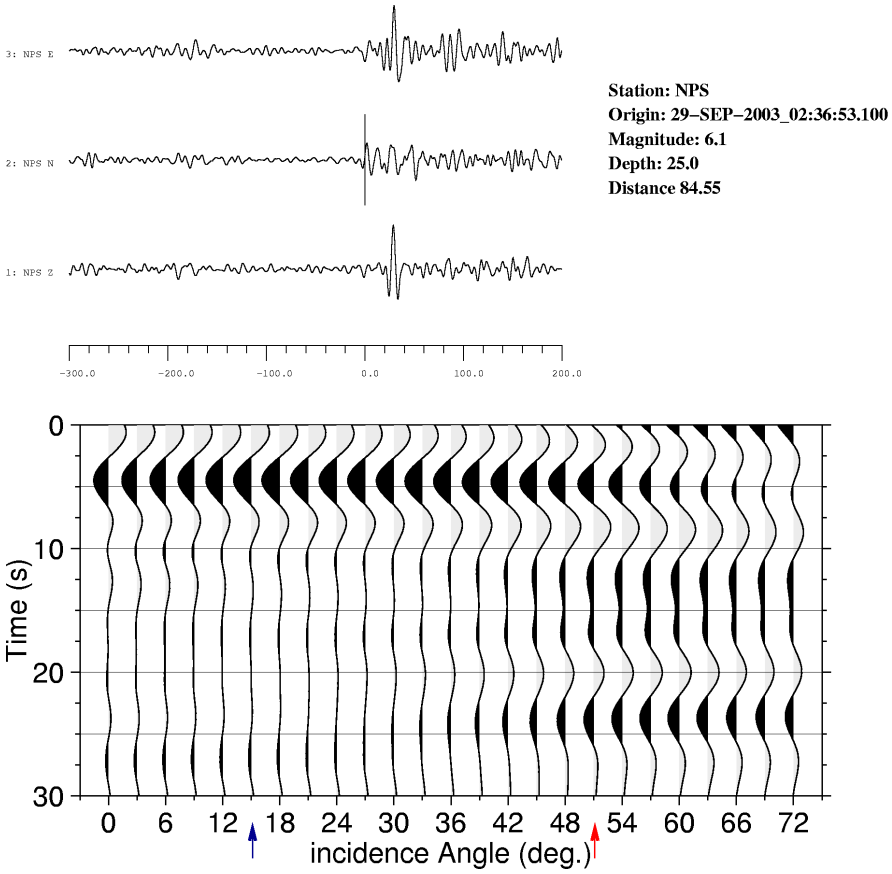

Fig.3.16. The L component has been rotated around different incidence angles ranging between 0-72°. The three components of the short period station as well as the event parameters are shown at the top of the Figure. The theoretical and observed incidence angles are indicated with blue and red arrows, respectively. The best incidence angle is defined where no energy on zero time occurs (51°), while the theoretical angle is at 15°.

For such a simple model, the theoretical incidence angle agrees well with the observed one (marked with arrow at 12°). However, in contrast to the P receiver function method, the selected incidence angle has a significant role in detecting the other major Sp converted phases. Taking an incorrect angle of incidence can enhance a noise phase and weaken a major converted phase in the whole seismogram. While in the P receiver function method, only the first 1-2 s of the seismogram will be affected by an incorrect incidence angle (shallow deep discontinuity).

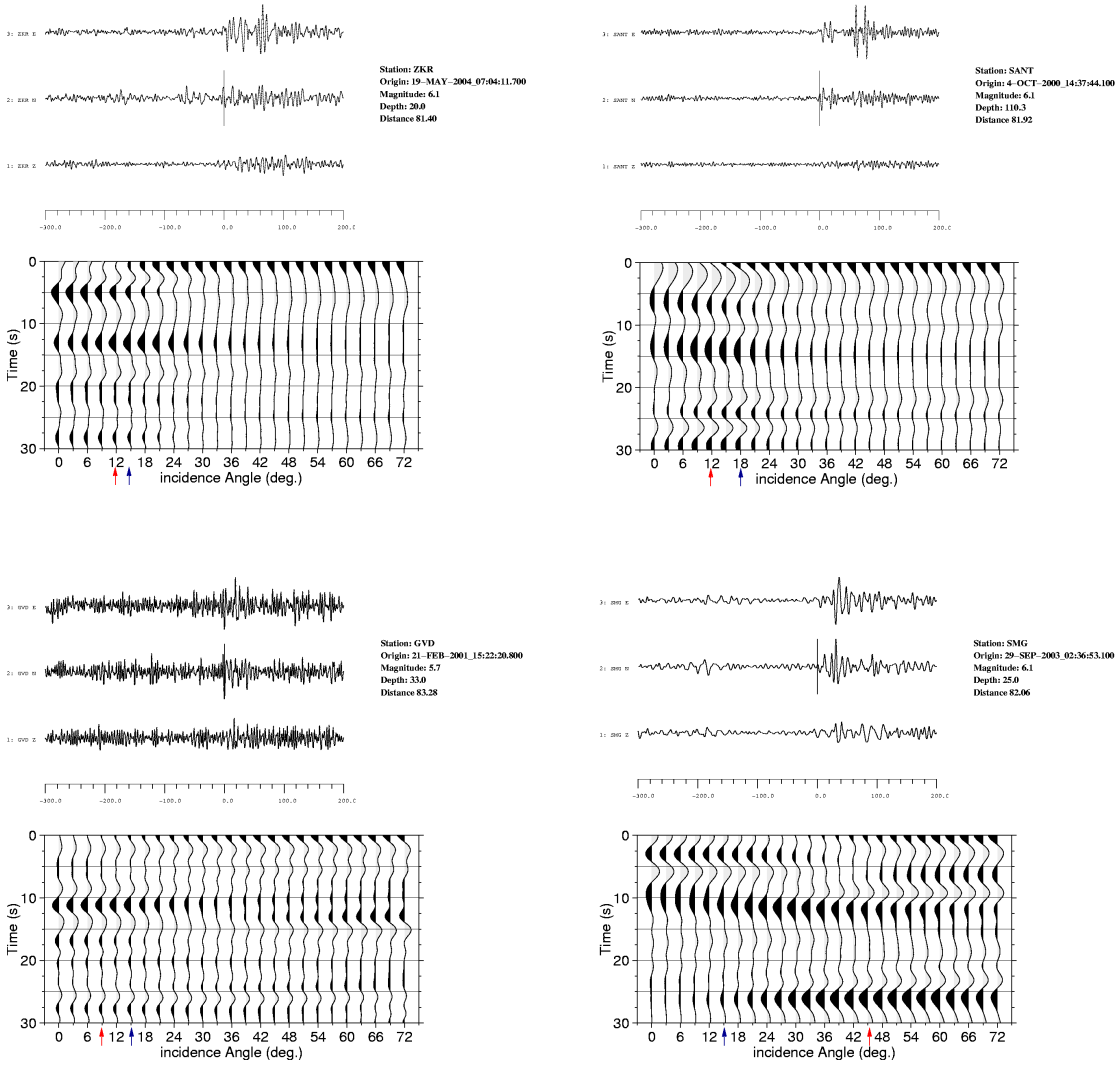

Fig.3.17. Some examples of rotation procedure used to estimate the best incidence angle. The blue and red arrows show the theoretical and observed incidence angle, respectively. This procedure results in a minimum P energy on the zero time and strong appearance of the major Sp converted phases in the whole seismogram.

Some examples shown in Figures 3.16-3.17 display the application of the rotation subroutine for different events. Figure 3.16 represents an event at 85° distance with magnitude of 6.1 recorded at short period station NPS. The S wave is quite sharp on the horizontal components. The S-onset arrival time is shifted to be as zero time. The lower panel shows the L components obtained from rotation around incidence angles of 0-72°. While the theoretical angle at 15° leaves some energy on zero time, a greater incidence angle at 51° shows the least energy on zero time and additionally enhances

the amplitude of the LAB converted phase at about 13 s. Therefore, a perfect rotation will be achieved if asides from the minimum energy on S-onset time, the major conversions are also well displayed on the L component.

3.2.4 Deconvolution

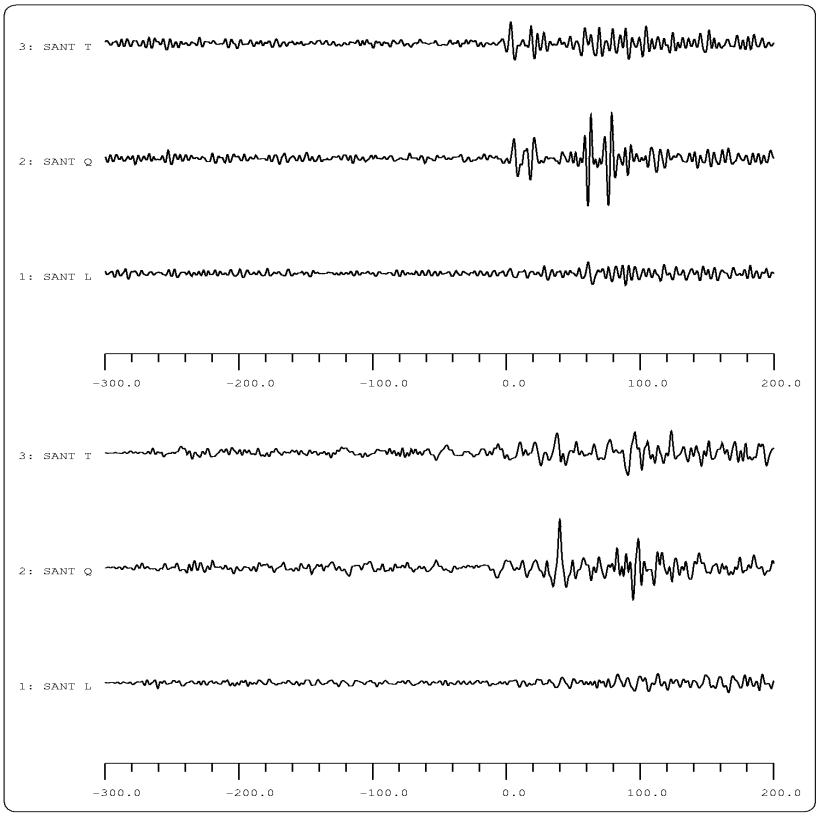

Fig. 3.18. The three components record shown in Figure 3.14 after rotation and deconvolution. The upper panel shows the rotated components around the theoretical back azimuth and observed incidence angle. In the lower panel all components are deconvolved with the S signal on the Q component. The most Sp energy dominates the L component.

After rotation, the converting Sp phases mostly dominate the L (P) components. In order to remove the S signal from the L components, the L components are deconvolved with the S signal on the Q components. The resulting L component, which contains only converted Sp phases (no multiples) is named S receiver function.

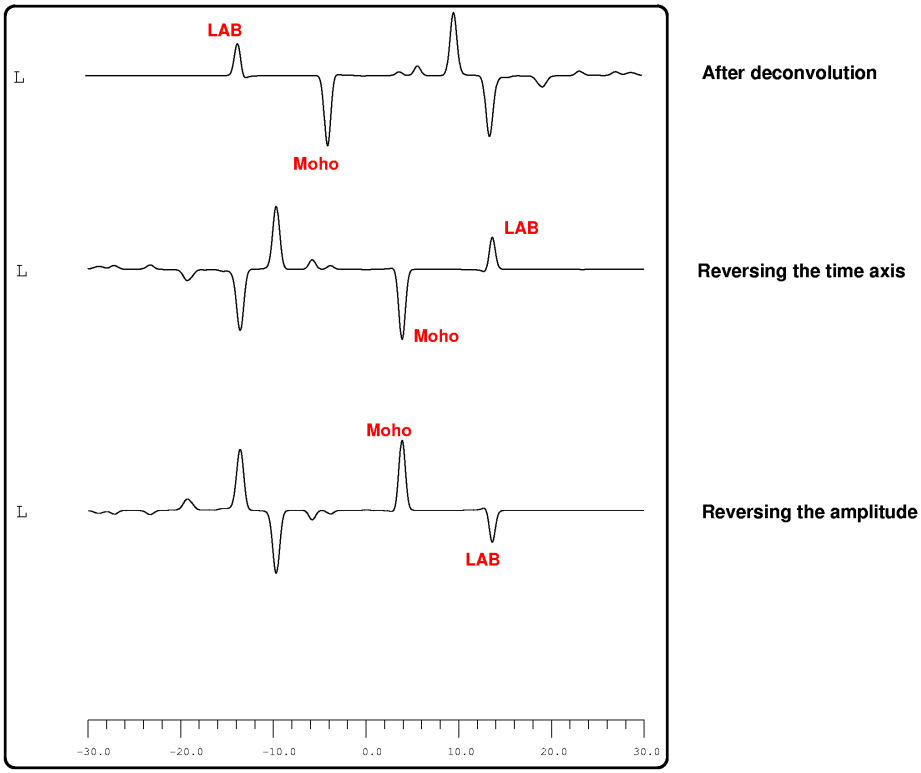

Fig. 3.19. Synthetic S receiver function after deconvolution has a reversed form comparing with the P receiver function. To compare it directly with P receiver function, the time axis as well as the amplitudes are reversed.

Figure 3.18 shows the seismograms indicated in Figure 3.14 after rotation and deconvolution. However, the coefficients of the S-to-P conversions have different signs than those of the P-to-S conversions. Figure 3.19 represents the computed S receiver function for the model shown in Figure 3.13. To make the S receiver function look like conventional P receiver function, some changes are needed. As Figure 3.19 shows, the resulted S receiver function has a reversed time axis compared to the P receiver function time axis. Therefore the time axis of the S receiver function has to be reversed in the first step. The different sign of the S-to-P conversion coefficients results in the reversed polarity of the S receiver function amplitudes. To remove this effect, the polarity of the S receiver function also has to be reversed. Finally, the resulted S receiver function can be directly compared with the P receiver function.

3.2.5 Moveout correction and stacking

The dependence of the arrival time of the Sp converted waves on the S wave slowness (move-out) has to be corrected for by using a reference slowness and a reference earth's model (like P receiver function). To directly compare the Sp and Ps receiver functions, the same reference slowness of 6.4 s/° (corresponding to epicentral distance of 67°) is also applied to S receiver functions, although this value is not realistic for S waves. Figure 3.20 shows the computed synthetic S receiver functions using the reflectivity method for a single station.

The IASP91 model is modified to contain the crust and lithosphere at 35 and 120 km, respectively. The P velocity is assumed to be 6.20 km/s in the crust and 8.0 km/s in the uppermost part of the upper mantle, which is reduced 5% at the lithosphere-athenosphere boundary. The S receiver functions of different events have been sorted according to their epicentral distances ranging between 60-110°. As Figure 3.20a shows, the variations of moveout curves get stronger with increasing conversion depth. For a shallow depth (Moho) the variation is very small, while delay time variations at LAB and upper mantle discontinuities become significantly larger. However, using a movout correction for Sp according to the reference slowness of 6.4 s/° helps to enhance the major Sp converted phases. Figure 3.20b indicates the S receiver functions after moveout correction. Moveout time corrections for Sp waves (reference slowness 6.4 s/°) are used for each sample in S receiver functions. After moveout correction, the converted Sp phases from the major discontinuities like Moho and LAB are aligned vertically, while the upper mantle discontinuities are not well aligned and have slightly oblique appearances. Since Sp conversion phases are usually weak signals, a number of records must be summed to obtain a good signal-to-noise ratio. The sum trace of the moveout corrected S receiver functions presents strong direct conversions from all major discontinuities, as shown at the top of Figure 3.20. Finally, the time difference between converted Sp and S waves can also be converted into the depth domain using a reference velocity model (e.g. IASP91).

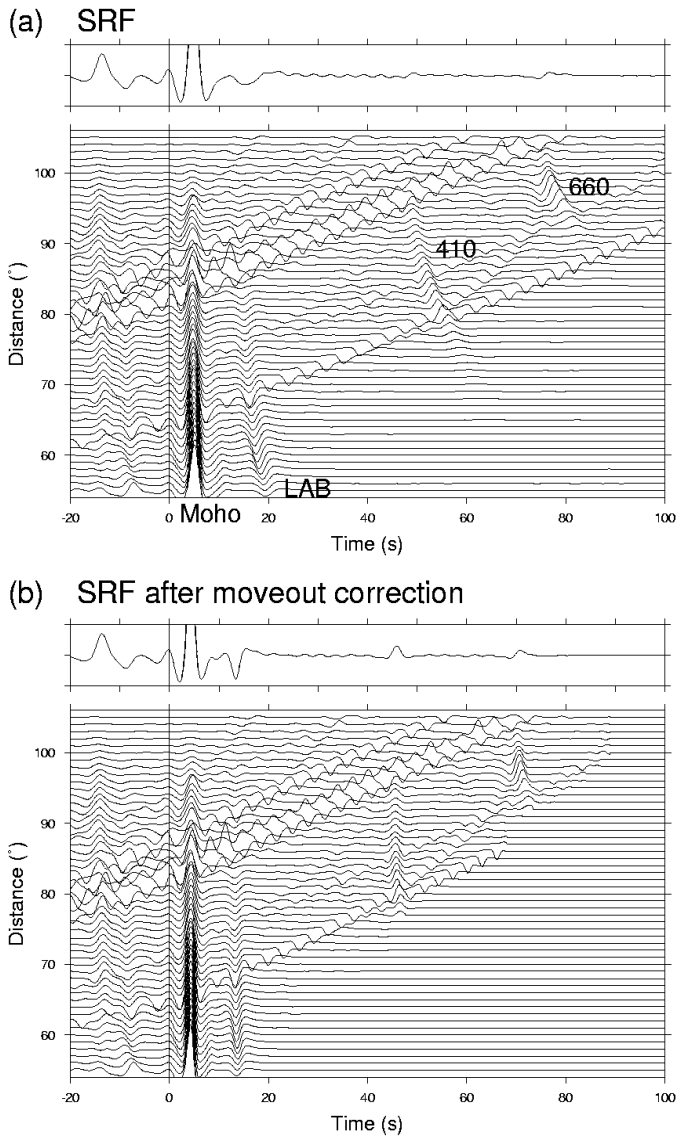

Fig. 3.20. Synthetic S receiver functions at a single station are computed using reflectivity method for a model containing a 35 km thick crust and 120 km thick lithosphere. The P velocity is considered to be 6.2 km/s in the crust, 8.0 km/s in the upper mantle with 5% reduction into the asthenosphere. Epicentral distances range between 60-110. a) By increasing epicentral distance, the delay times of Sp conversion decrease. b) Moveout corrections for Sp waves are applied to each sample. Reference slowness of 6.4 s/° is used. Sp converted phases are aligned vertically and their amplitudes are enhanced on the summation trace shown at the top.

The S receiver function as described before leads us to obtain the LAB with a resolution so far only known for the Moho.

CHAPTER 4

In this study, the teleseismic earthquakes recorded by various permanent and temporary stations have been utilized to compute P and S receiver functions. Descriptions of each data set as well as spatial distributions of stations are presented in this chapter.

4. Data

Due to various constraints for applying P and S receiver function techniques, a number of data sets are used.

4.1 Data set for P receiver function analysis

4.1.1 Seismic stations

In order to reach an optimum station coverage across the Aegean, various networks were deployed. The first one consisted of 21 stations, which had been installed across the Aegean during the "Seisfaultgreece" experiment from January 1997 to July 1997 to record teleseismic and regional earthquakes. They were equipped with Lennartz LE5S (5 s), Güralp CMG40 (20 or 60 s), and Güralp CMG3 (60 or 100 s) seismometers and Reftek 72A06 and Agecodagis TitanDat data loggers, which recorded continuously at a sample frequency of 50 or 62.5 samples per second, respectively. Stations were installed in permanent observatories of the National

Observatory of Athens, of the Seismological Network of Thessaloniki, and in temporary shelters. They are indicated with triangles in Figure 4.1. Their coordinates and equipments are also given in Table A.1, Appendix A.

Fig. 4.1. Location of the seismic stations used for P receiver function technique. NOA stations are represented by circles, Seisfaultgreece stations by triangles, GEOFON stations by cubes and MEDNET stations by star. Hexagons denote both NOA and Seisfaultgreece stations.

8 permanent broad band stations of GEOFON network located on the island of Crete and in the southern Aegean Sea were also used to compute P receiver functions. The stations were equipped with STS-2 seismometers and have been in operation since 1996 by the GFZ Potsdam. More records were available from GEOFON stations, since they are operating for several years. In Figure 4.1 the GEOFON stations are

shown as cubes. Deploying one permanent MEDNET station located on the island of Crete could improve the spatial coverage on this island. IDI, shown with star in Figure 4.1, was equipped with STS-2. The station distribution was significantly enhanced using the 21 permanent stations of the National Observatory of Athens, which were equipped with either Lennartz LE20S or Güralp CMG40 seismometers. These stations have been utilized since March 2003 for a period of 11 months. The distribution of the stations is represented with circles in Figure 4.1.

4.1.2 Prerequisites for P receiver function method

The data which satisfied the following conditions have been used to compute P receiver functions.

1. Epicentral distances between 30-95°
2. Magnitude larger than 5.5 (mb)
3. clear P onset with high signal-to-noise ratio

A total number of 343 teleseismic earthquakes (Table B.1-B.3, Appendix B) recorded by 43 broad band and short period stations have been used to estimate lithospheric structure in the Aegean area using P receiver function technique. The epicenter distribution of the earthquakes is shown in Fig. 4.2.

4.2 Data set for S receiver function analysis

4.2.1 Seismic stations

In order to have a high resolution data in the central and southern Aegean Sea, The CYC network located in the Cyclades area, operated by Bochum University has been deployed since 2002 for a period of 23 months.

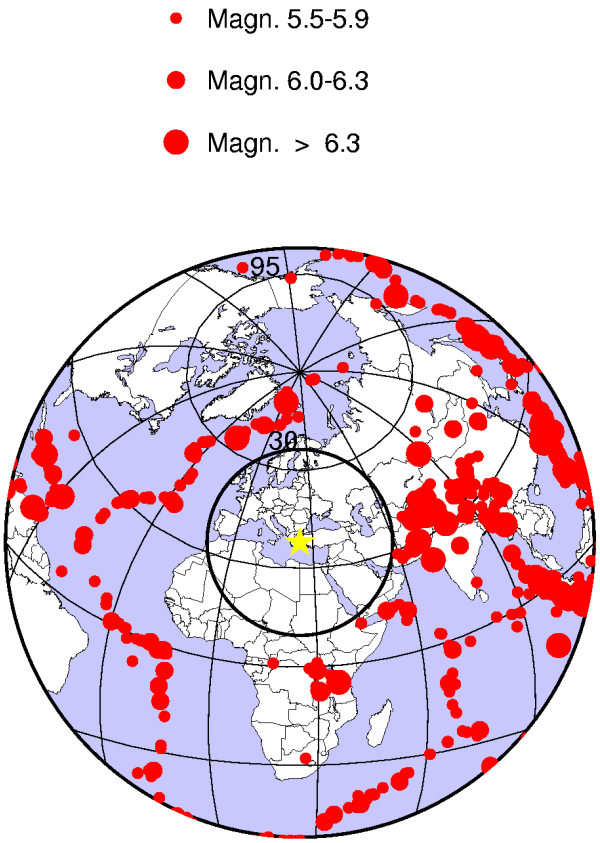

Fig 4.2. Epicenter distribution of earthquakes used to determine P receiver functions. The events have magnitude larger than 5.5 (mb) with epicentral distances between 30-95°.

The CYC-NET consisted of 22 temporary short period stations equipped with Mark L4-3D and in some cases STS2 seismometers. The coordinates of the stations as well as the equipments used are detailed in Table A.1, Appendix A. This network together with 8 broad band GEOFON stations as well as 21 NOA stations and one MEDNET station have provided a homogeneous station distribution within the study area, as shown in Figure 4.3.

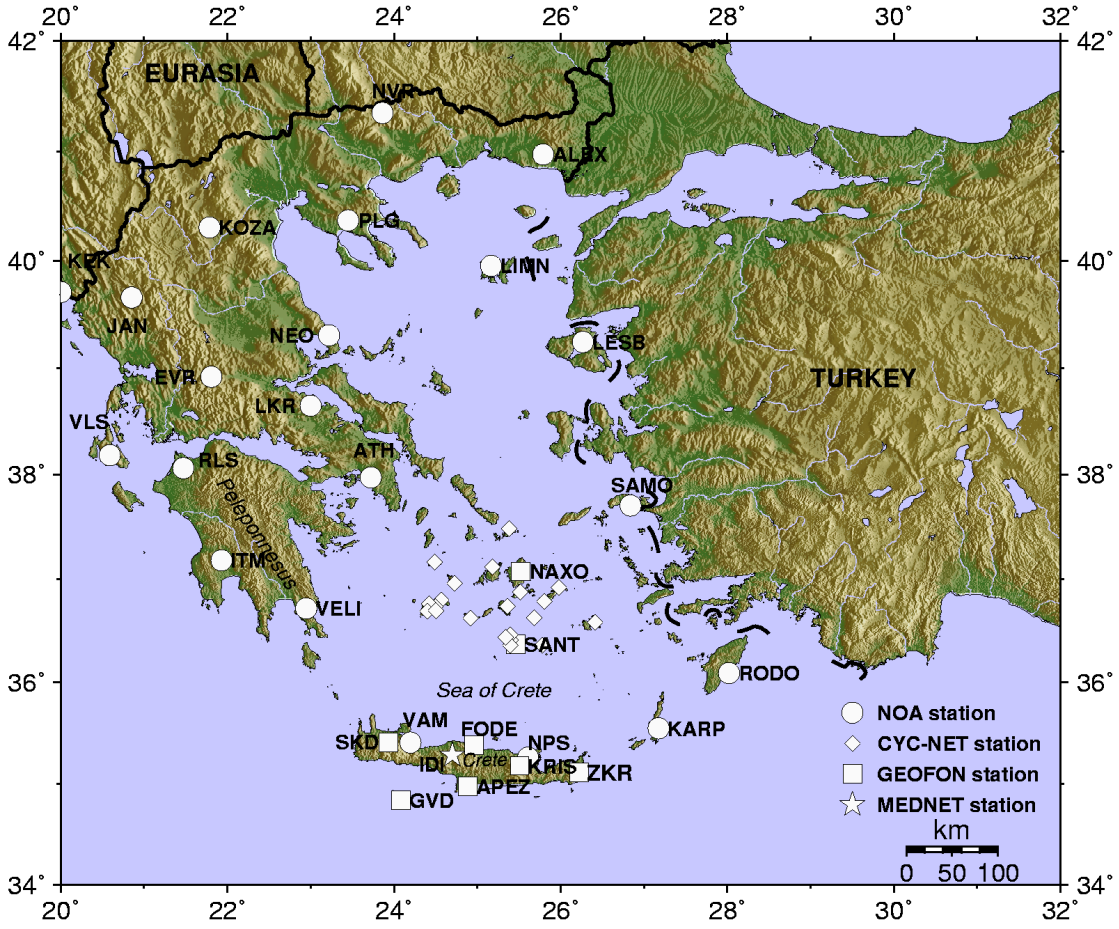

Fig.4.3. Location map of the seismological stations utilized to compute S receiver functions. The CYC-NET stations are represented with diamonds in central Aegean. Cubes and circles denote GEOFON and NOA stations, respectively. The MEDENET station located on the island of Crete is shown with star.

4.2.2 Prerequisites for S receiver function method

To obtain lithospheric structure by S receiver function technique, the data were selected according to the following criteria:

1. Epicentral distances between 60-85°
2. Magnitude larger than 5.7
3. A clear S onset with high signal-to-noise ratio

The Data of 21 temporary stations of the Seisfaultgreece were not included to compute S receiver functions, since they had low signal-to-noise ratio. A total number of 294 teleseismic earthquakes (Table B.4-B.6, Appendix B) recorded by 52 broad band and short period stations have been also utilized to investigate lithospheric structure in the Aegean area using S receiver function technique. The earthquakes distribution is shown in Figure 4.4.

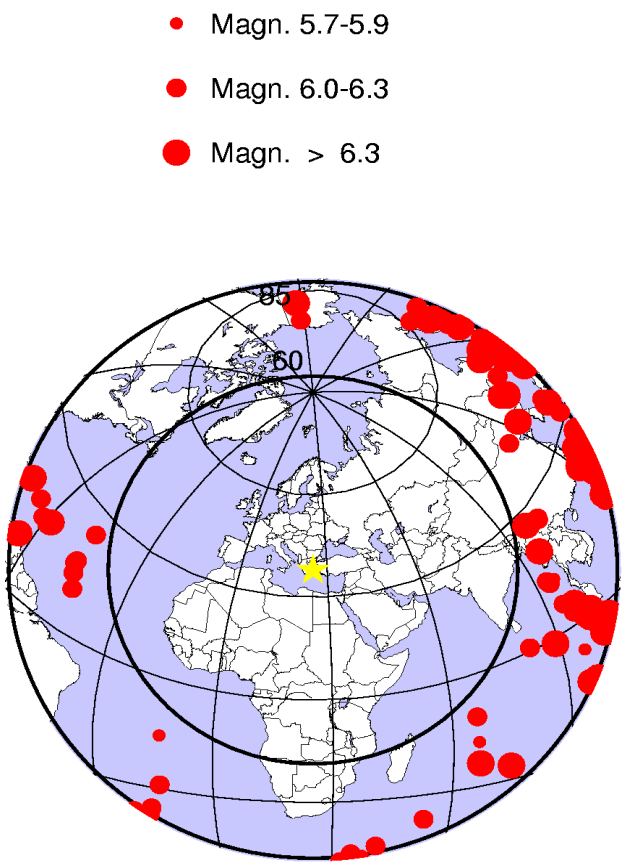

Fig. 4.4. Epicenter distribution of the events used to estimate S receiver functions. The selected data have magnitude larger than 5.7 with epicentral distances between 60-85°.

CHAPTER 5

In this chapter, the results obtained from P and S receiver function analysis are presented and discussed. The receiver functions have been derived using the three-component seismological data in the study area in order to delineate the crustal and upper mantle structures beneath Greece and Aegean Sea.

5. Results and Discussions

Since two different methods used in this thesis, the results were also divided into two parts. Firstly, the crustal and upper mantle structures are deduced from P receiver function method and in the second part, results obtained from S receiver function method are shown and discussed. The results are interpreted in a unified way and compared with previous works.

5.1 Results from P receiver functions

5.1.1 Observed P receiver functions

Teleseismic P receiver functions were computed by using theoretical back azimuth and incidence angle as explained in chapter 3 for each station. A distance (moveout correction) correction was applied prior to stacking to achieve high signal to noise ratio. Figures 5.1-5.3 show P receiver functions for six stations located in different parts of the study area.

Distance-corrected receiver functions using a reference distance of 67° for station LIMN, LESB located in northern Aegean Sea and ALEX and NEO located in mainland Greece are shown in Figure 5.1-5.2. The P receiver functions were sorted according to their increasing back azimuth. Red cubes indicating back azimuth, while epicentral distances are plotted with black circles. The data have been filtered between 1 and 10 s and are plotted in a time window of -5 to 20 s in order to give information for both continental and oceanic lithospheric structures.

Positive amplitudes are shaded in black and indicate (if caused by direct conversion) an increasing velocity with depth, whereas negative amplitudes (shaded in gray) demonstrate velocity decreasing downwards. The P onset is fixed to be as zero time. The sum traces in the upper panels present the stacked P receiver function for each station. At stations shown in Figure 5.1-5.2, P receiver functions exhibit clear primary Ps conversion from the Moho and multiply-reflected phases, which reverberate between earth's surface and Moho discontinuity. The Ps conversions from the Moho arrive at delay time of about 3-4 s, while the multiples are observed at 10-14 s delay time. However, the arrivals of the multiple phases are not clear shown in receiver functions. Another Ps conversion observed at about 0.5 s is attributed to the sedimentary layer, which is significantly located below the surface. P receiver functions for two other stations KARP and ZKR located at the forearc of the subduction; in the southern Aegean Sea and on the island of Crete, respectively, show another feature (Fig. 5.3). Asides from the clear Ps conversion from a sedimentary layer, which can be observed at about 1 s, a very stable and dominant converted phase can be also identified at about 6 s delay time. This phase is clearly related to the oceanic Moho of the subducting African plate, which can be clearly observed beneath forearc area of the subduction. The absence of the converted Moho phase (Fig. 5.3) with positive amplitude is however clearly demonstrated by receiver functions.

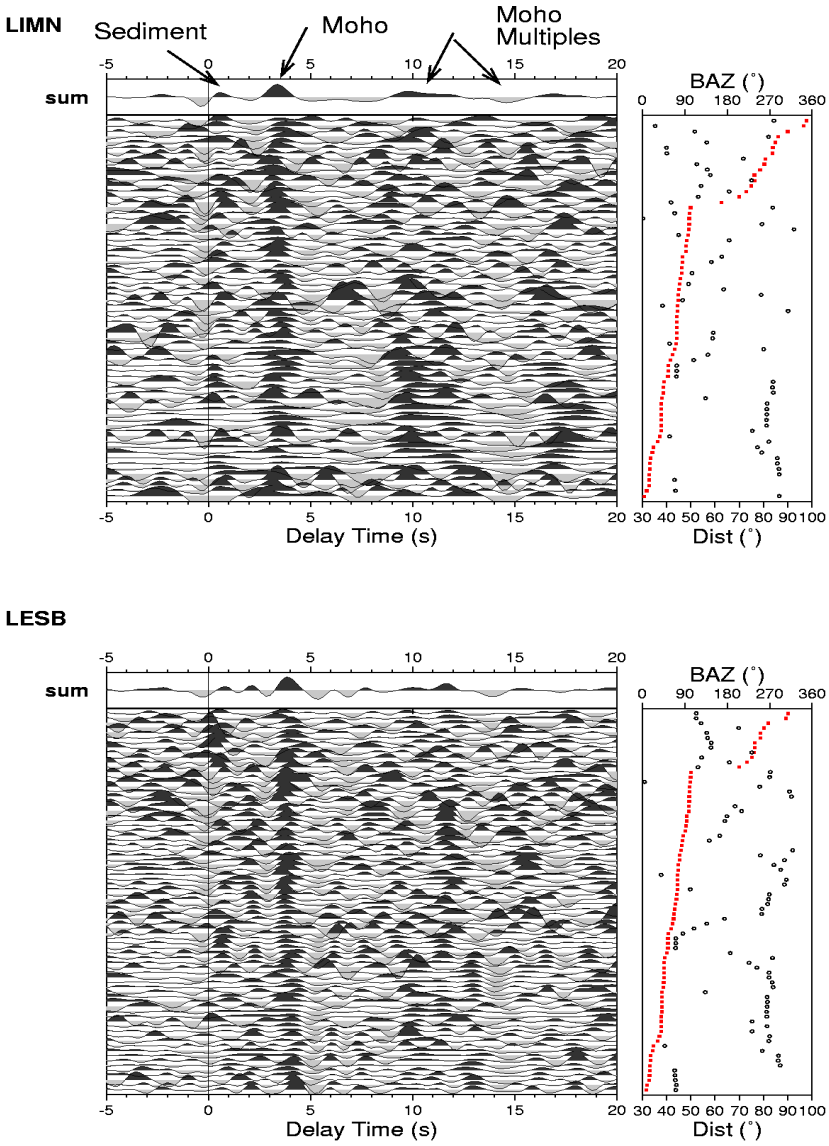

Fig. 5.1. Individual P receiver functions for the two stations LIMN and LESB located in northern Aegean Sea. The moveout-corrected receiver functions are sorted by their back azimuth and filtered with bandpass filter 1-10 s. Red cubes show back azimuth and epicentral distances are indicating by black circles. The summation traces at the top of the figures represent clearly the Ps converted phases from sediment at ~ 0.5 s, whereas Ps conversions from Moho arrives at 3-4 s delay time. The Moho multiples are not well identified in the data, but arrive near 10-14 s delay time.

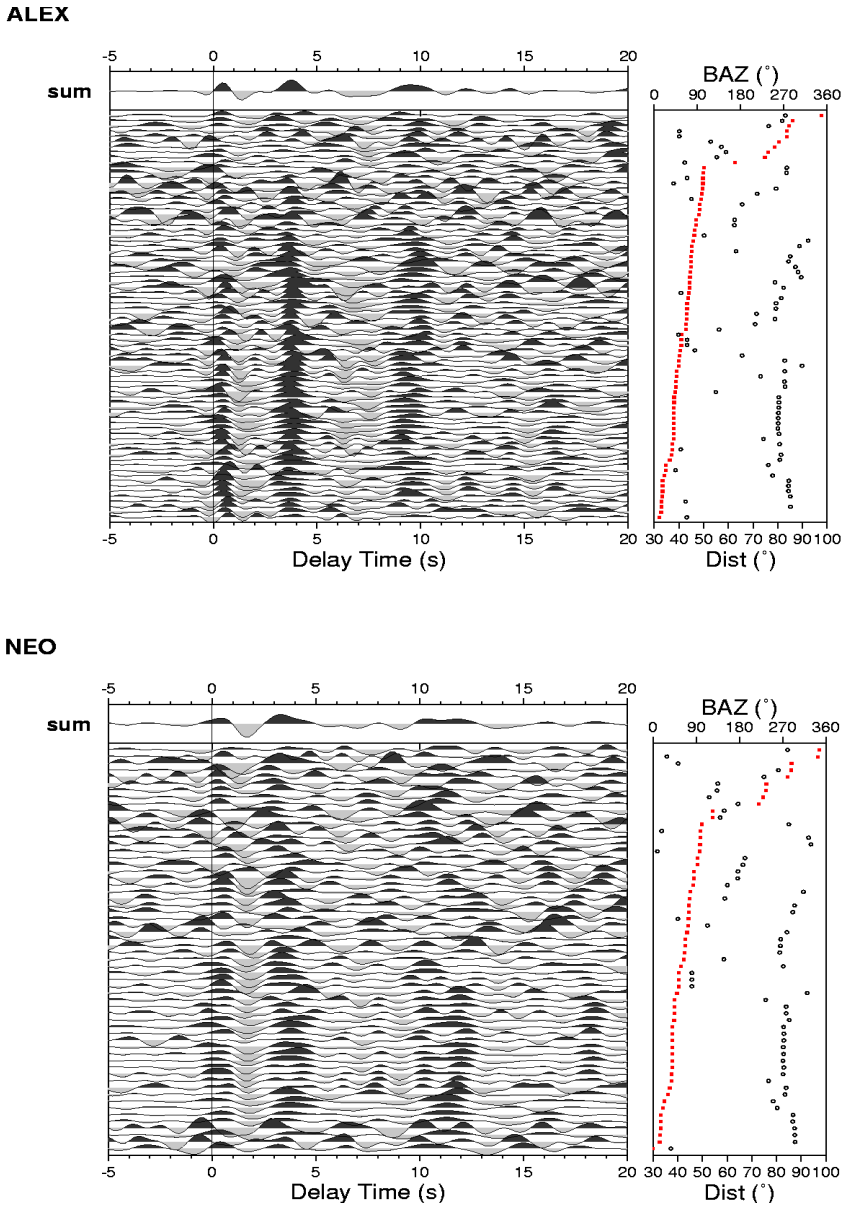

Fig. 5.2. Individual P receiver functions for the two stations ALEX and NEO located in mainland Greece. The arrival times of the Ps converted phase from sediment and Moho boundary as well as Moho multiples can be clearly seen in the summation traces shown at the top of the figures.

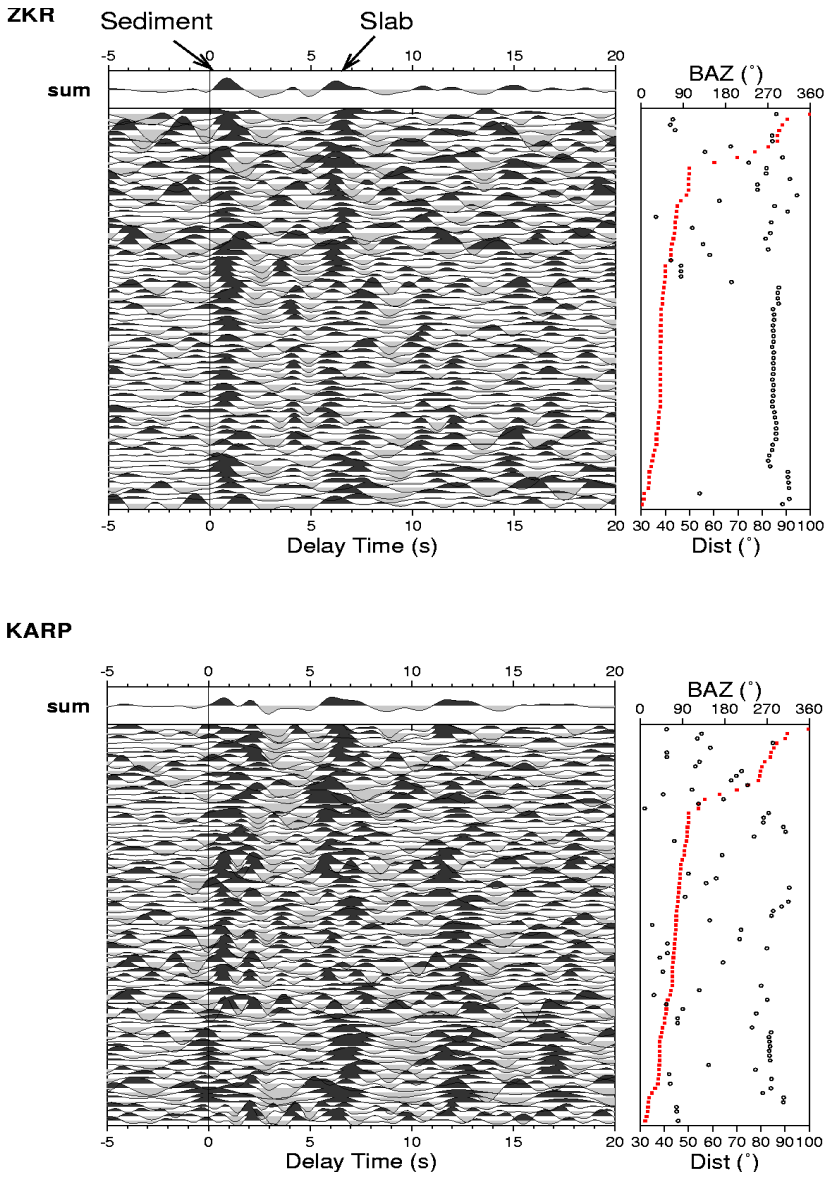

Fig. 5.3. Moveout-corrected P receiver functions obtained from the two stations ZKR and KARP located at the forearc area of the subduction show no clear conversion from the Moho boundary, while the arrival times of the Ps conversion from sediment and African Moho (slab) are well imaged.

This phase can not be identified for these two stations, while it was well observed at the other stations located in northern Aegean Sea and continental Greece.

5.1.2 Reversed Moho contrast in the forearc

To have a glimps of the crustal structure in the entire area, the results from P receiver functions for all stations are summarized in Fig. 5.4. The stacked P receiver functions obtained from each station are sorted by their relative distance to the Hellenic trench, from south to north, and provide an average thickness beneath each station. They were filtered between 1-20 s. The number of receiver functions stacked is also indicated with the station code in parenthesis. The observed energy at time 0 for some stations suggests that either the rotation of the components is not optimal or that local sediments generate some energy.

Regarding Figure 5.4, the receiver functions obtained for stations in the southern Aegean and on the island of Crete (labeled with FA in Figure 5.4) reveal clearly an increase of Ps delay time toward the north, reaching a 10 s delay time beneath the volcanic arc. This phase is related to the oceanic Moho of the subducted African plate, which will be referred to as "slab" hereinafter. This phase can be followed from 4.5 s beneath station VLS in western Peleponnesus to 11 s beneath station SANT at the volcanic arc (labeled with VA). However, further north, the identification of this phase is not clear anymore. Under the stations located in the northern Aegean Sea and in continental Greece (labeled with NA and CG, respectively), the converted Ps energy is clearly observed between 3 and 4.8 s. This phase is related to the Moho of the continental Aegean plate, which will be referred to as "Moho" hereinafter. This phase is however not well observed under the southern part of the region (FA). Of interest, a significant converted phase with a negative amplitude is observed at some stations located in the forearc (marked with a dashed red box). This negative phase observed for the most stations at Crete, (Knapmeyer, 2000; Li et al., 2003; Endrun et al., 2004) has also been reported in the Cascadia subduction zone (Bostock et al., 2001) and was interpreted to be due to a reversed Moho velocity contrast caused by the hydration and serpentinization of mantle minerals in the forearc.

Since serpentinite has shear wave velocity lower than the crustal velocities, it causes a reversed Moho contrast in the mantle wedge. However, this phase can not be followed beneath stations located in northern Aegean Sea and continental Greece.

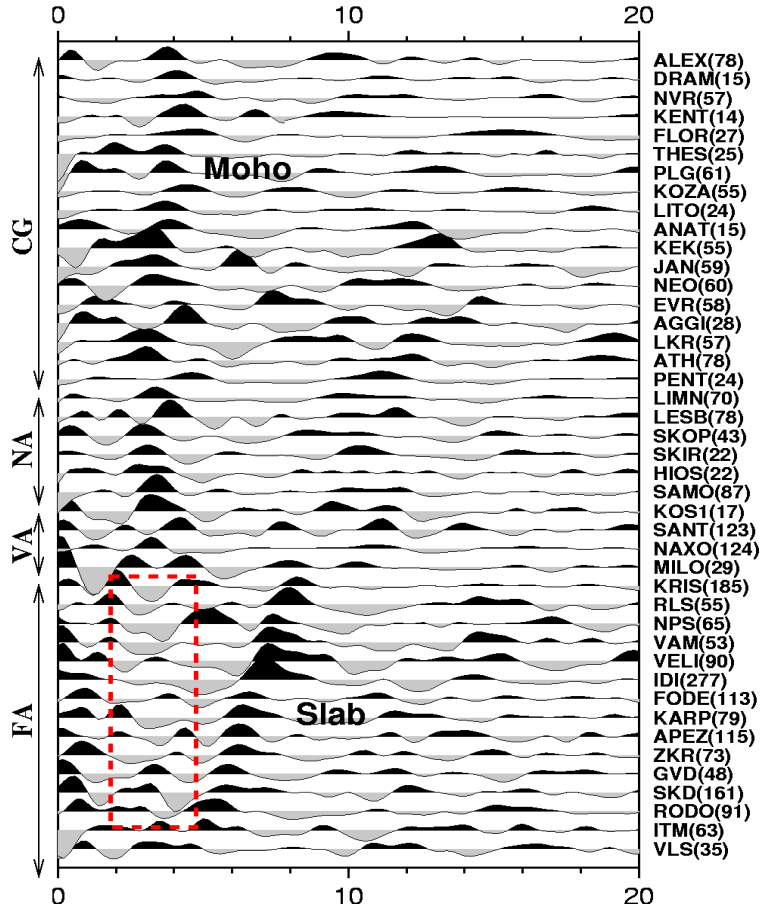

Fig. 5.4. Stacked P receiver functions sorted according to their distance from the Hellenic trench from forearc to mainland Greece. The north dipping phase in the southern part labeled "Slab" indicates Ps conversions from the Moho of the subducting oceanic African plate. This phase can be traced from station VLS in western Peleponnesus to the station SANT at the volcanic arc (or may continue till 13 s) . Ps conversions from the Moho of the continental Aegean plate are observed in the northern part beneath NA and CG and disappears southward. Red dashed line underlines clear negative conversions observed beneath FA at the expected Moho times. The number of P receiver functions for each station is also shown in brackets. FA = forearc, VA = volcanic arc, NA = northern Aegean and CG = continental Greece.

5.1.3 Calculating Moho depth from Ps conversions

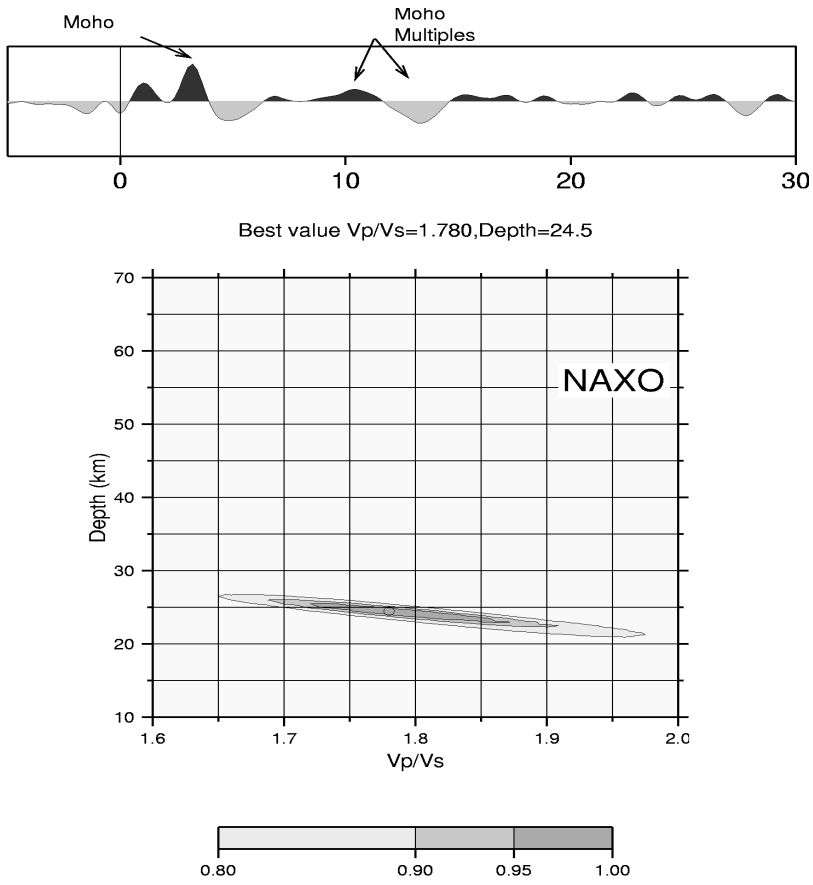

Fig. 5.5. Successful application of Zhu and Kanamori method for station NAXO with relatively clear multiple phases shows a Moho depth of 24.5 km and average Vp/Vs ratio of 1.78.

To compute the Moho depth, the Zhu and Kanamori method could not successfully be utilized for all stations. Since this method looks for the primary conversion of the Moho as well as multiples , in absence of clear multiples, the computed Moho depth and Vp/Vs ratio will be unrealistic. However, in presence of good multiple phases the crustal parameters have been derived in some cases. Figure 5.5 shows an example of successful application of Zhu and Kanamori method for station NAXO located in the Cyclades where the clear multiples are observed. The Moho depth and Vp/Vs ratio are

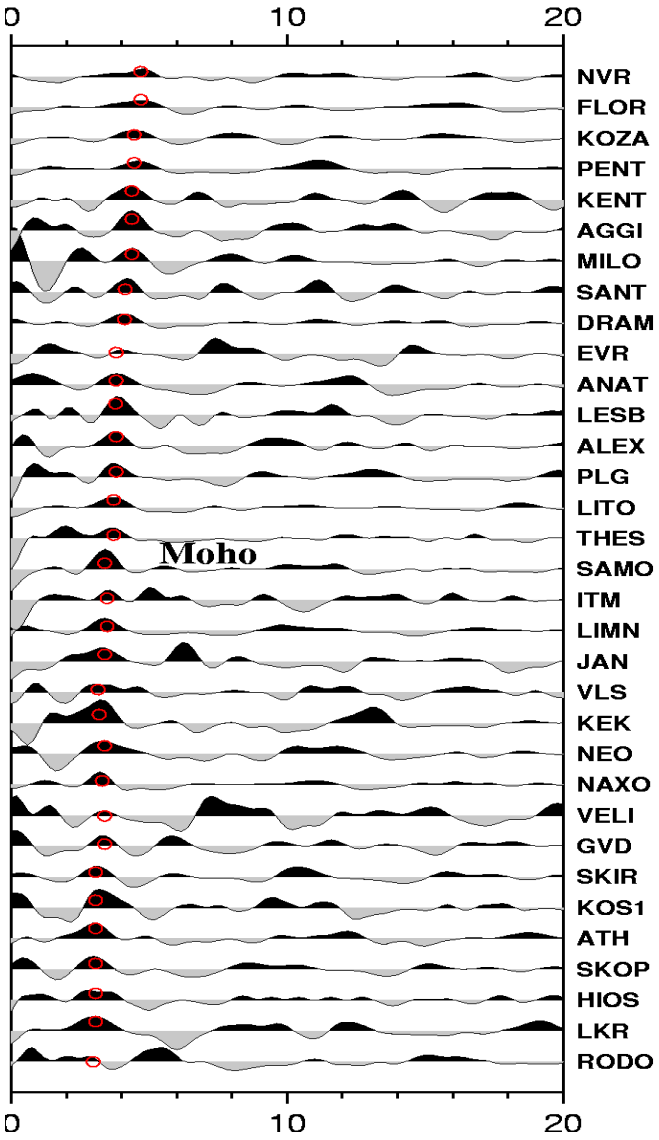

Fig. 5.6. The stacked P receiver functions for stations with observed normal Moho contrast are sorted according to the increasing time of their Moho conversions. No clear multiples can be seen in the data. Moho arrival times are converted into depth values using Vp of 6.2 km/s and Vp/Vs ratio of 1.73.

computed using the arrival times of Ps converted phases from the Moho as well as its multiples, which are marked on the stacked receiver functions. But to construct a homogeneous Moho map for the whole area, a unique method is needed, which could

be similarly performed for all stations without considering the multiples. In Figure 5.6, the stacked P receiver functions are sorted by increasing time of the converted Ps Moho phase. The data show clear primary Moho conversions with arrival times ranging between 3-4.8 s, even though Moho multiples are not significantly visible in the data. To compute the Moho depth for the stations with observed positive Moho phase, a reference crustal velocity of 6.2 km/s and Vp/Vs ratio of 1.73 (similar to the IASP91 reference model) were used. The calculated Moho depths are shown in Table C.1, Appendix C. No estimation of the delay times of Moho converted phase obtained from stations in the forearc was attempted, due to their negative amplitudes.

5.1.4 Calculated Slab depth from Ps conversions

The delay times of the observed slab phase are also converted into depth, using the IASP91 reference model. The delay time of the slab phase is estimated from the P receiver functions if it is clearly visible in the data. The delay times of the slab phase and corresponding depth values are listed in Table C.1, Appendix C.

5.1.5 Receiver function migration

To generate a depth section, the receiver functions for each station are migrated in space and projected onto three vertical profiles (Fig. 5.7) trending normal to the Hellenic trench in the western, central and eastern part of the Hellenic arc. Also included in Figure 5.7 is the epicenters of shallow and intermediate depth earthquakes occuring in this region (mb >= 4.5) along the Hellenic arc (Engdahl et al., 1998). As the seismicity shows, the deep earthquakes (~ 180 km) are located in the southeastern part of the Aegean beneath the Dodecanese islands.

The obtained 2D migrated sections along three profiles are represented in Fig. 5.8. Positive amplitudes of receiver functions are plotted in red, while negative amplitudes are in blue.

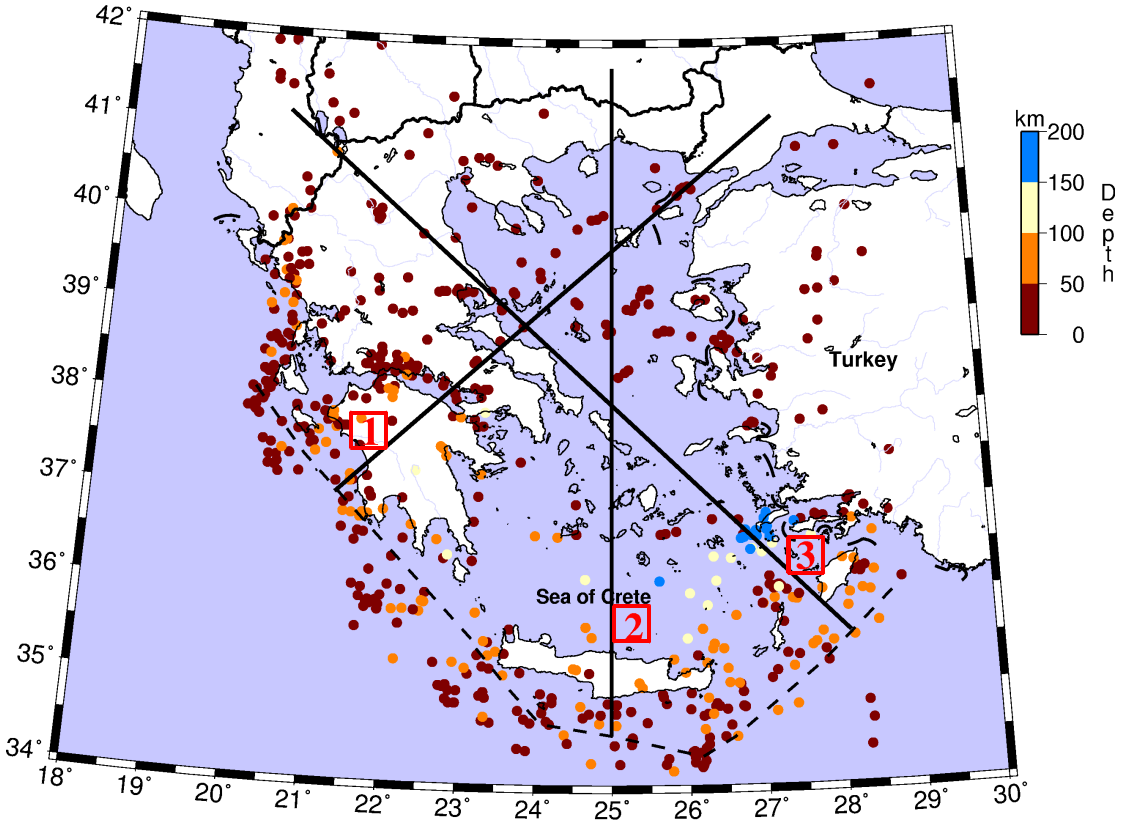

Fig. 5.7. Epicenters of the shallow and intermediate depth earthquakes (mb >= 4.5) across the whole Aegean shows that the deepest earthquakes are located in the southeastern part of the Aegean beneath Dodecanese islands (~ 180 km). Three vertical profiles normal to the Hellenic trench are considered to image the Hellenic slab beneath each part of the area.

The seismicity along the profile is also plotted on each section as an evidence for the presence of the subducted slab. The subducted African slab can not be well identified by these cross-sections, however, the seismicity reliably shows an increasing in the slope of the downgoing slab towards east.

A 2D migrated receiver function section obtained from the summation of all three profiles, displays an average image of the continental Moho and of the descending slab (Fig. 5.9). The seismicity could not be plotted on this migrated section, due to the summation of three different profiles with varying geometry for the subducted oceanic plate.

The converted phase associated with the continental Moho is observed under the northern Aegean Sea and mainland Greece (labeled with NA and CG, respectively) at depths ranging from 30 to 40 km, while further south this phase disappears. The subducting oceanic Moho is reliably imaged from ~ 35 to about 100 km depth in the volcanic region. However, this image can not be considered as the absolute shape of the slab because the summation is affected by data quality and the number of events, which are not the same along all the three profiles, and insufficient for a meaningful migration.

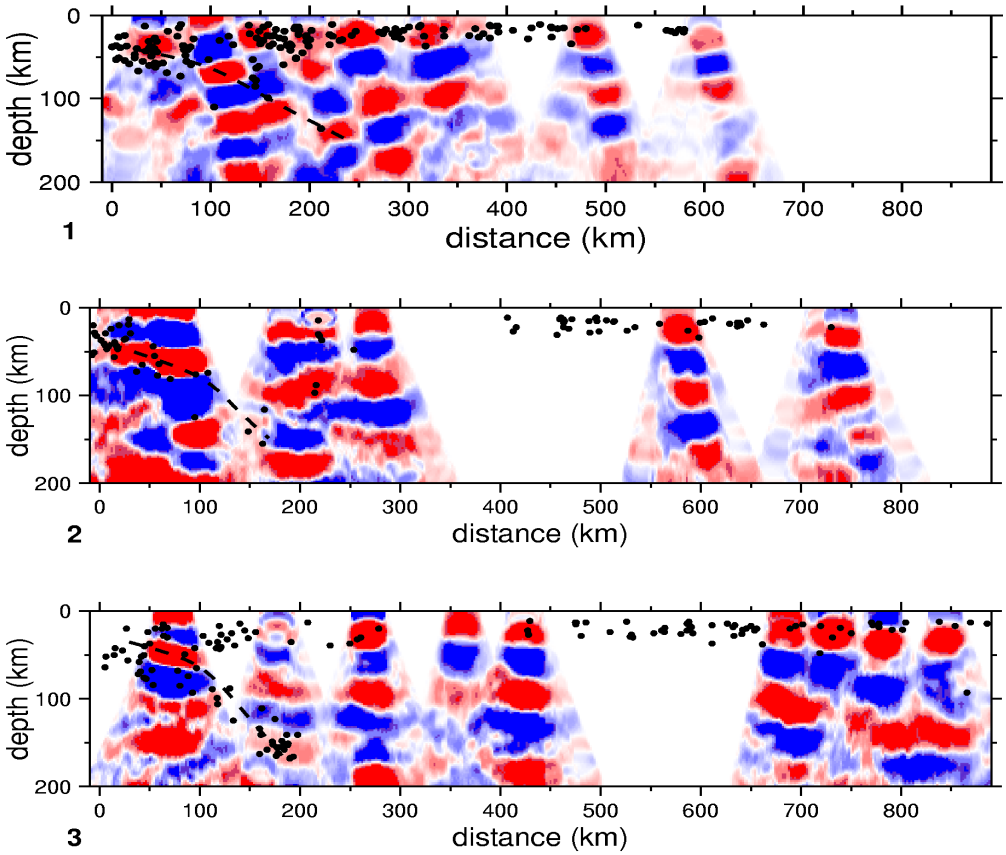

Fig. 5.8. 2D migrated P receiver function sections along three profiles located in the western, central and eastern part of the Hellenic arc shown in Figure 5.8. The positive amplitudes of receiver function are plotted in red, while blue color shows negative amplitudes. The seismicity is also projected on each cross-section. Although the descending African slab is not well resolved on the cross-sections , seismicity shows reliably an increasing in the slope of the subducted slab towards east.

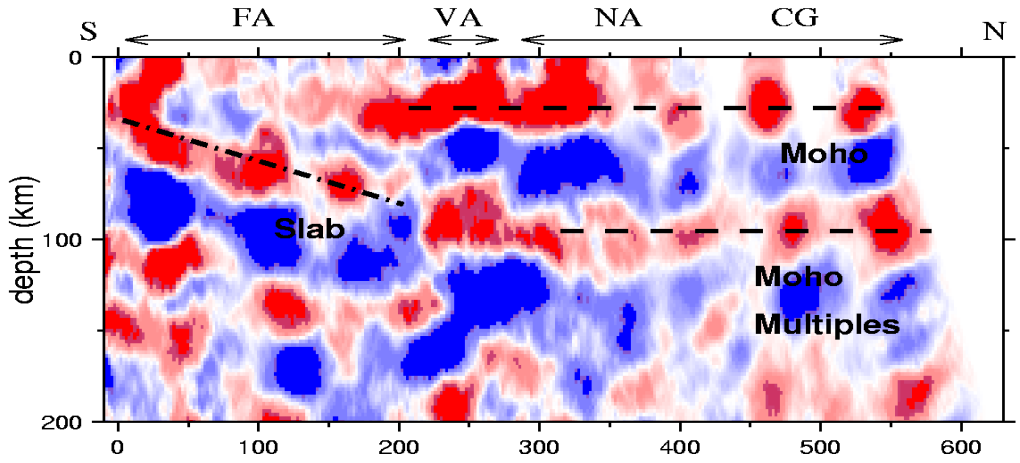

Fig. 5.9. 2D migrated P receiver function section obtained from the summation of the three profiles normal to the Hellenic trench, shown in Figure 5.8. The continental Aegean Moho and its multiples as well as the subducted oceanic African Moho are indicated by labeled dashed lines. The slab can be identified beneath forearc area and volcanic arc (shown with FA and VA), which reaches the depth of 100 km under volcanic arc. The Moho boundary beneath northern Aegean Sea and continental Greece (NA and CG) is clearly imaged at 30-40 km. The continuation of the continental Moho due to negative amplitudes in the forearc is less clear.

5.2 Results from S receiver functions

5.2.1 Observed S receiver functions

The new technique of S receiver functions (Kumar et al., 2005) has been applied to different datasets across the whole study area. The theoretical back azimuth and observed incidence angle were used to calculate the S receiver function (as shown in chapter 3). Moveout and bandpass filtered (6-20 s) S receiver functions of the GEOFON station KRIS located on the island of Crete is shown in Figure 5.10. In order to compare receiver functions obtained from both the methods, the S receiver functions are plotted in reversed time and the polarities are also reversed. The negative

amplitudes are plotted in black and indicate velocity decreasing downwards, while positive amplitudes in gray show an increasing velocity with depth. The S receiver functions are sorted by their back azimuth marked at the right.

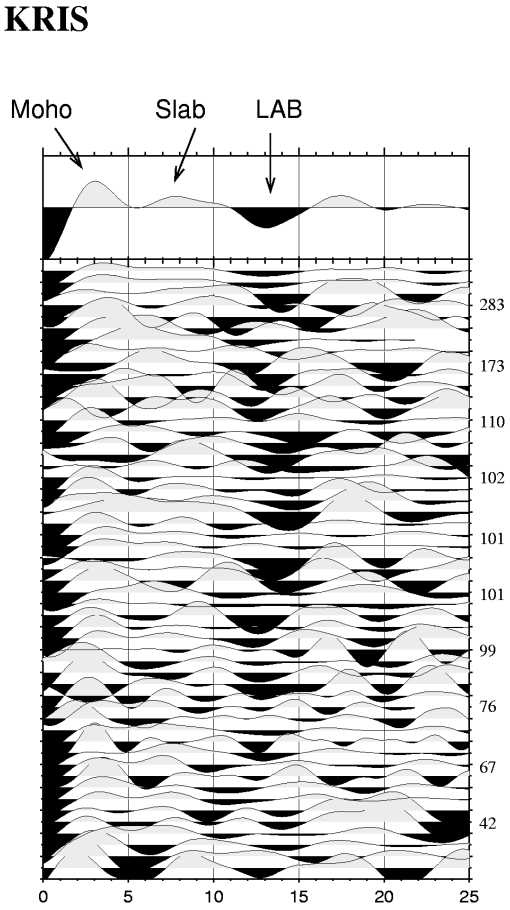

Fig. 5.10. Individual S receiver functions for station KRIS on the island of Crete are sorted by their back azimuth (shown at the right). Negative amplitudes are plotted in black and indicate velocity decreasing downwards. The S receiver functions are plotted in reverse time in order to compare with P receiver functions. The arrows on the stacked trace show the average time of the Sp conversions generated by the continental Moho, the oceanic Moho of the subducted slab and the lithosphere-asthenosphere boundary, respectively.

Three phases are visible on the records, which are marked on the summation trace at the top in Figure 5.10 . The first phase, at about 3 s, shows the converted Sp phase due to the Moho discontinuity, the second phase at about 8 s is related to the oceanic Moho of the descending slab. The third phase, which has a strong negative amplitude

(velocity decreasing downwards) at about 13 s delay time is interpreted as due to the lithosphere-asthenosphere boundary (labeled with LAB). This phase is usually not seen in P receiver functions because it is masked by crustal multiples arriving at nearly the same time.

5.2.2 Distribution of piercing points

S receiver functions are computed for all stations in a same way. Unlike P receiver functions, the Sp conversions are not located close to the stations and show additionally significant overlapping with the Sp conversions obtained from adjacent stations. In Figure 5.11 the location of the piercing points at 80 km depth (likely to be approximately the thickness of the LAB) for the Ps and Sp conversions are plotted. While P piercing points are located (laterally) close to the recording stations, S piercing points are located much farther away. The lack of P receiver function data in the Sea of Crete can be seen clearly in Figure 5.11, which makes the P receiver function map of the Moho and downgoing slab less certain under this region. However, the Sea of Crete and central Aegean are well covered with S receiver function data. Due to the wider lateral distribution of piercing points for the S receiver functions compared to those of P receiver functions as well as the overlap of S piercing points from neighbor stations, the crustal and upper mantle structure can not be studied by considering S receiver functions from individual stations.

5.2.3 Descending oceanic African Moho

To illustrate the slab geometry from S receiver functions, two sets of cross-sections are considered. The whole study area can also well be covered by selected cross-sections. The first set consists of three N-S trending cross-sections parallel to each other across the Aegean and continental Greece (Fig. 5.12). The profiles A and B are located in the eastern and middle part of the Hellenic arc, respectively, while profile C

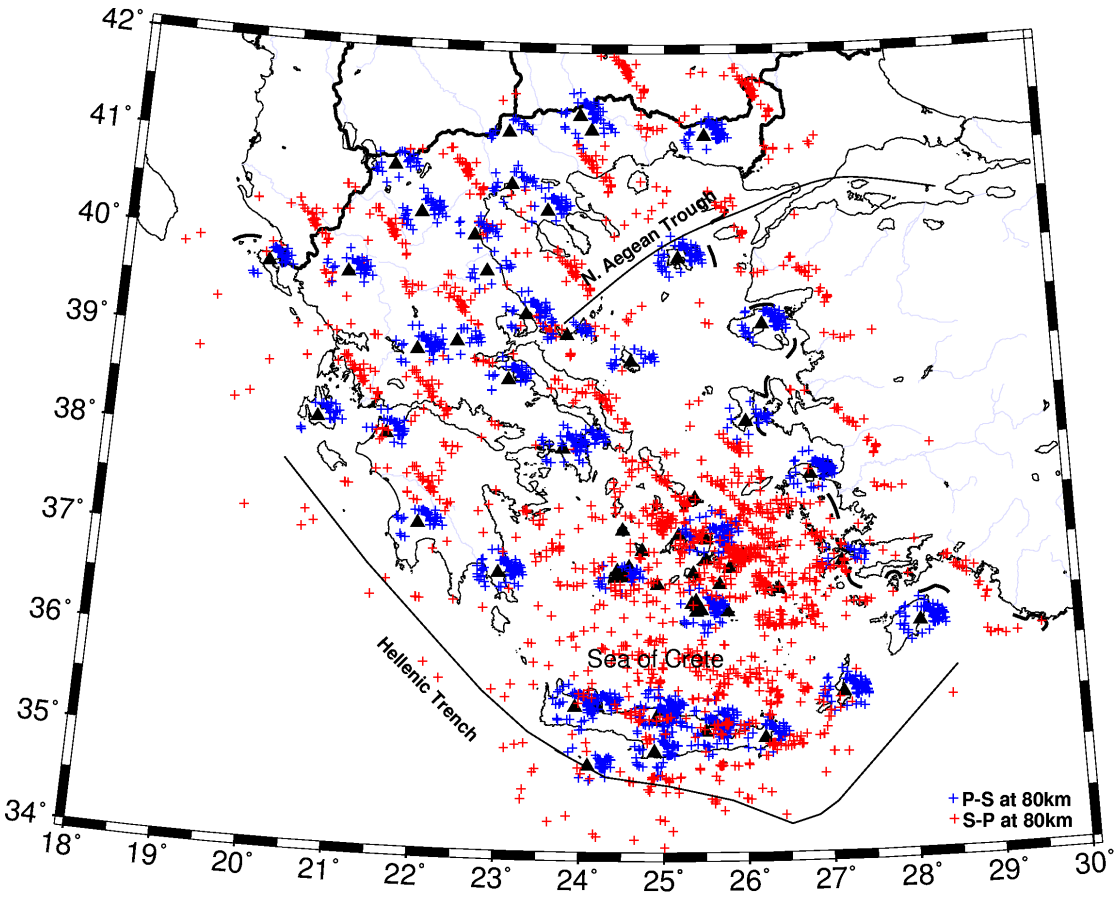

Fig. 5.11. Location of piercing points of P and S receiver functions at 80 km depth. Stations are indicated by triangles. While P piercing points are located close to the stations, the S piercing points occurred much farther away. The Sea of Crete is well covered with S piercing points.

crosses Peleponnesus and western continental Greece. The next set consists of three profiles perpendicular to the Hellenic trench, shown in Figure 5.13. The profiles D, E and F are located normal to the trench in the eastern, middle and western part of the Hellenic arc, respectively. Individual S receiver functions are sorted by the latitude of their piercing points at 80 km depth along each profile, shown in Figures 5.14 and 5.15. Positive amplitudes are plotted in black. Although the individual traces are much noisier than stacked data, they allow a more detailed image of the Moho and of the subduction.

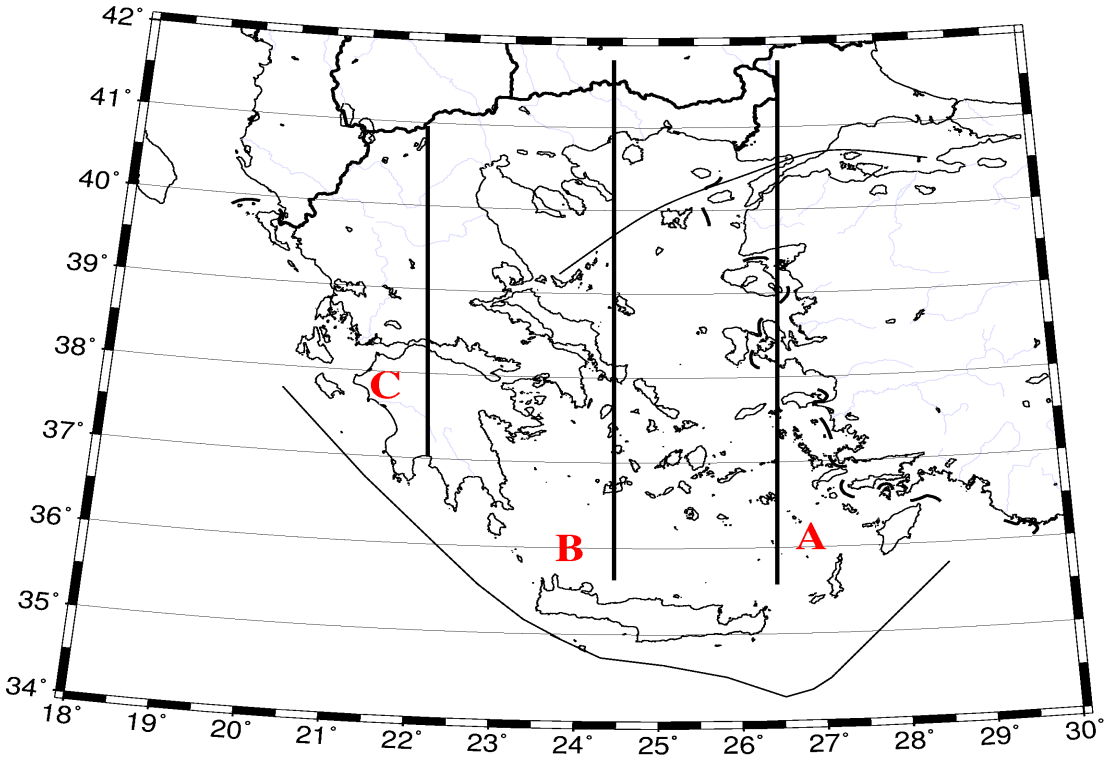

Fig. 5.12. Positions of three parallel cross-sections (A, B, C) in the eastern, central and western part of the Hellenic trench.

5.2.4 Slab geometry obtained from Profiles A-C

As Figure 5.14 shows, asides from the primary converted phase from the Moho discontinuity, which can be seen between 2.5 to 4 s along profile A, a very strong and coherent phase can be also followed from 6 s (~ 50 km deep) in the southern Aegean down gradually to about 25 s (~ 230 km deep) in the northern Greece. This dipping phase is clearly related to the oceanic Moho of the subducting African plate. Due to the lack of seismological stations in the Aegean Sea the oceanic Moho could be only imaged by P receiver functions to 10 s beneath station SANT in the volcanic arc.

Along profile A, the downgoing slab has a noticeably variable slope. It starts at low angle in the southern Aegean and becomes steeper under the volcanic arc. It flattens out beneath the central Aegean and then steepens again beneath the northern Aegean Sea and continental Greece.

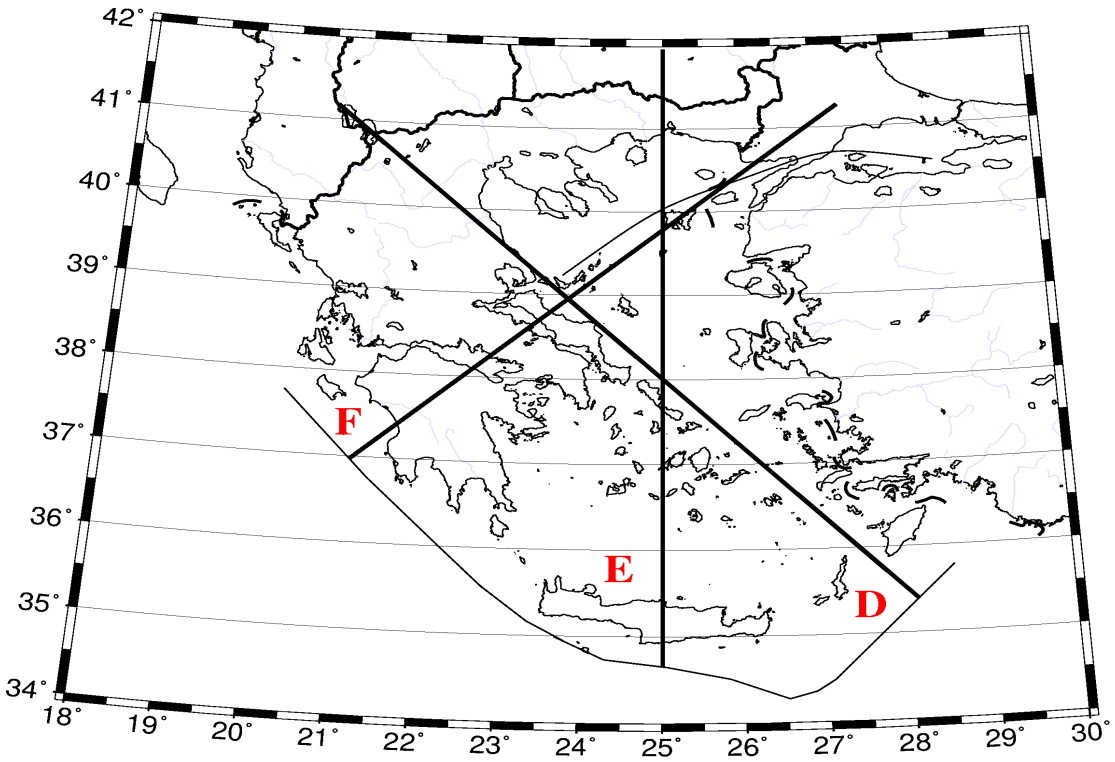

Fig. 5.13. Positions of next three profiles (D, E, F) normal to the Hellenic trench in the eastern, middle and western part of the arc.

In the central part of the Hellenic subduction zone, along profile B, the slab is clearly deeper than in the eastern part. It can be followed from 9 s in the southern Aegean down to 23 s beneath the northern Greece. It also dips gradually at a low angle to the northern Aegean and becomes horizontal towards mainland Greece. Beneath western Peleponnesus and western Greece, along profile C, the Hellenic slab is shallow and arrives at delay time of 5-6 s. The arrival of this slab converted phase is very close to that of the Moho converted phase, which seen at about 3 s. However, according to Figure 5.14 (C), there is no doubt that the converted phase at 5 s beneath Peleponnesus is associated with the Hellenic slab. The slab is almost horizontal beneath Peleponnesus, dips steeply (~ 45°) beneath the Gulf of Corinth and flattens out under continental Greece.

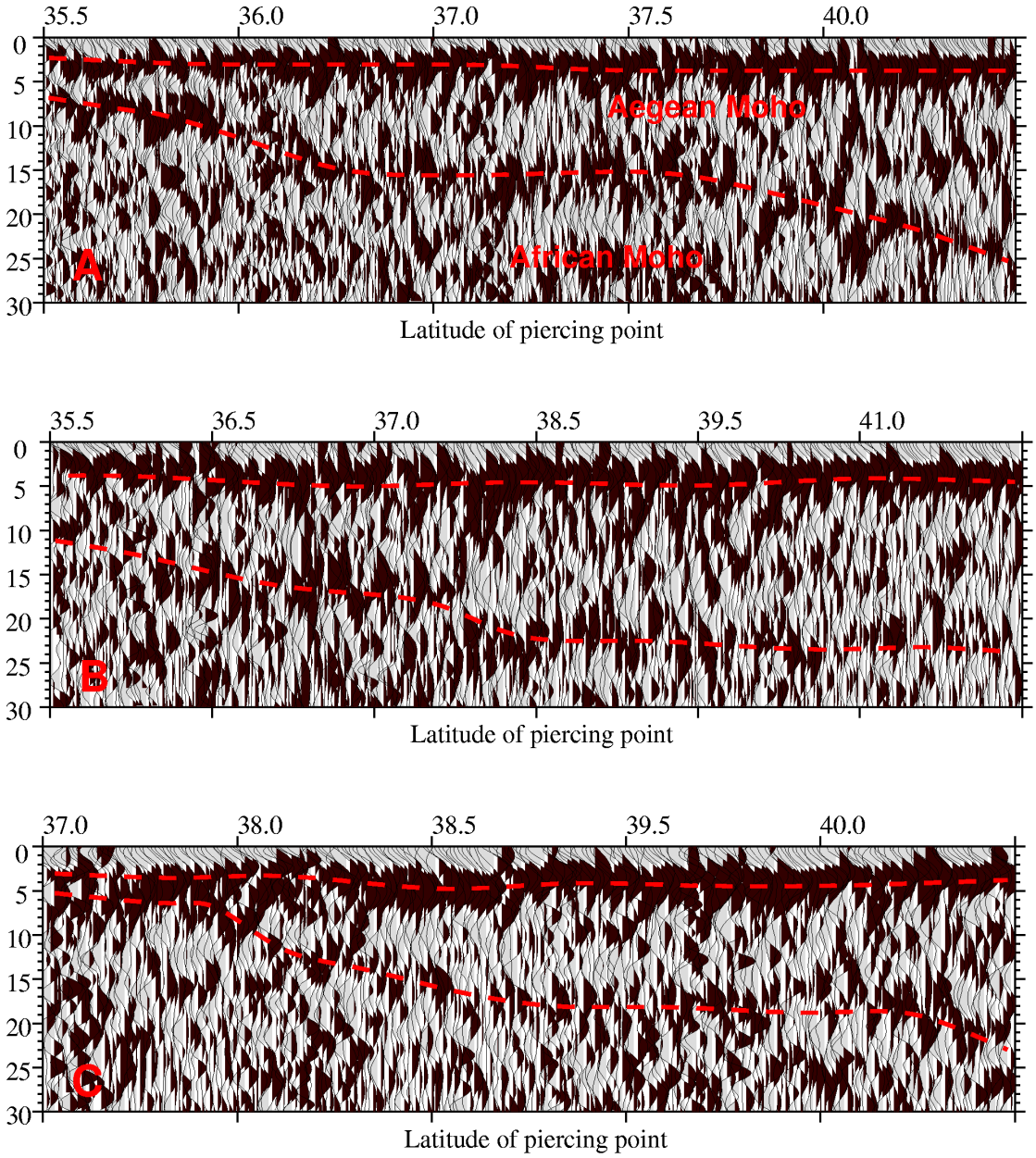

Fig. 5.14. The imaged structures deduced from individual S receiver functions along NS trending profiles A-C. The converted phases are underlined with a red dashed line. The first converted phase is related to the continental Aegean Moho and the second phase to the subducting African slab. A) individual S receiver functions sorted after latitude of S piercing points at 80 km along eastern profile A. The Moho and the downgoing slab are well demonstrated up to northern Greece. B) same for profile B in the middle part of the Hellenic arc. C) same for profile C located in the western part of the arc, which shows a shallower slab than the other parts of the arc. Towards north the slab shows a more straight form in comparison to its shallower part.

5.2.5 Slab geometry obtained from profiles D-F

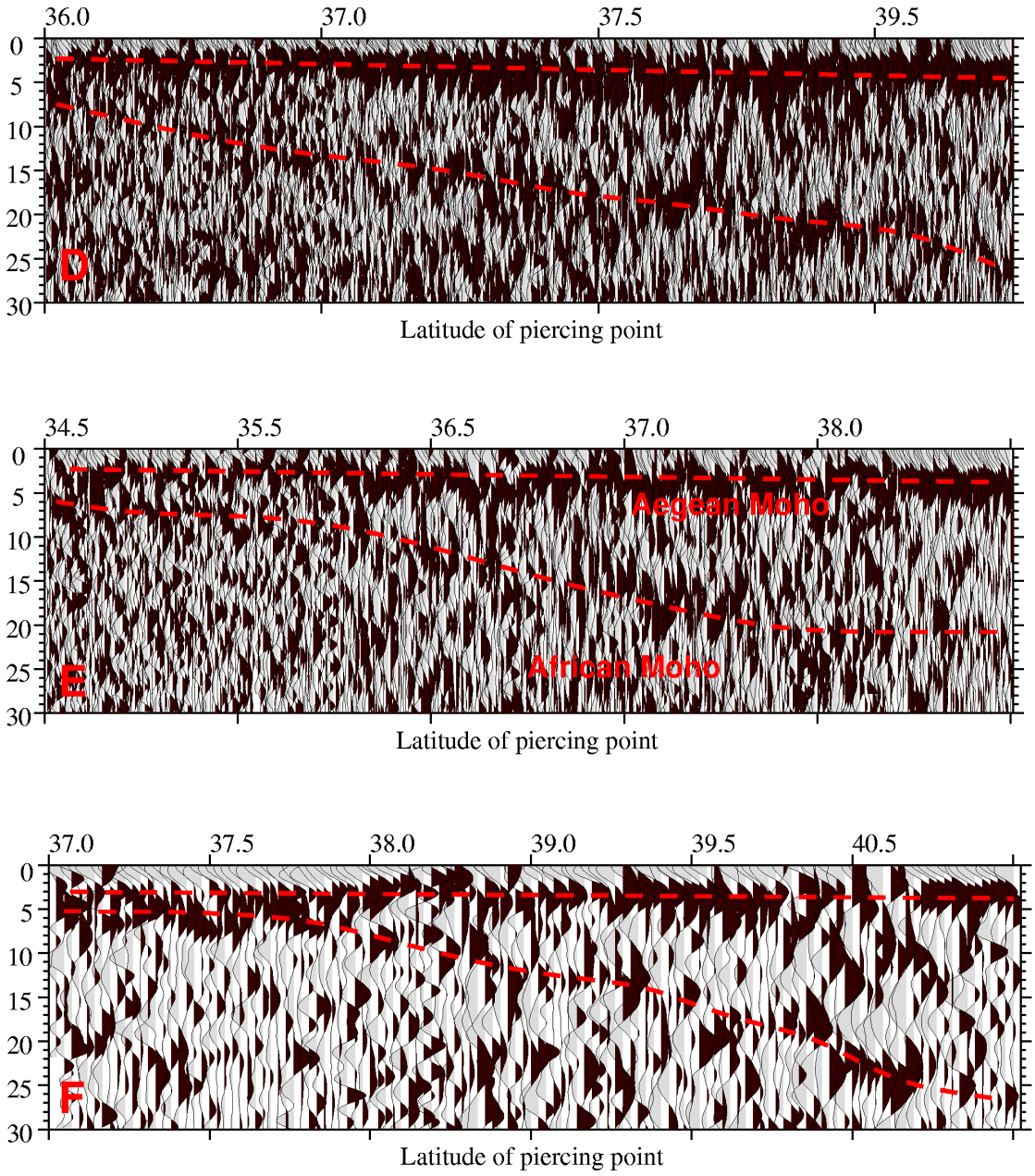

Fig. 5.15. Same as Figure 5.14 along profiles D-F located perpendicular to the trench. D) individual S receiver functions along profile D in the eastern part of the Hellenic arc. E) same for profile E in the middle part of the arc, which crosses the central Crete. F) same for profile F in the western part of the Hellenic arc. The slab is shallower imaged along profile F than along profiles D and E.

In profiles D-F, shown in Figure 5.15, the subducted slab is not as easily resolved as it is shown along profiles A-C. It is interesting to note although all three profiles begin from the Hellenic trench and include the forearc area, they demonstrate a significant Moho phase with positive amplitude in the forearc region, while P receiver functions exhibited a reversed Moho velocity contrast beneath stations located in the forearc.

Profile D located in the eastern part of the Hellenic arc indicates a steep subducted plate in this part in comparison with other parts of the arc. The continuity of the subducted plate up to northern Greece is well illustrated along this profile. This phase can be followed from 6 s beneath southeastern Aegean gradually down to 25 s under northwestern Greece.

Along profile E in the middle part of the Hellenic arc, the slab is identified at shallower depth (at about 5.5 s delay time) comparing with the eastern part of the arc. The dip of the subduction is low in the Cretan Sea and steepens significantly under the volcanic arc and reaches the delay time of about 20 s.

The slab is almost horizontal and is visible to about 24 s (220 km) beneath continental Greece. The slab depth along profile F is consistent with that from profile C in Figure 5.14. It shows a sub-horizontal slab beneath Peleponnesus at about 5 s and a sudden dipping in the northern Aegean Sea to a delay time of about 25 s. The main difference in slope of the slab can be also clearly seen along this profile.

5.2.6 Lithosphere-Asthenosphere boundary

The whole study area was divided into 39 non-overlapping boxes with respect to the distribution of Sp conversions at 80 km (Fig. 5.16). The size of each box corresponds roughly to the number of S receiver functions crossing that box. Since the Sp conversions are generally weak, a stacked S receiver function was computed for each box from many individual records. Prior to summation, the moveout correction for a reference slowness of 6.4 s/deg was applied. In Figure 5.17, the stacked S receiver functions computed in each box along profiles D-F (shown in Fig. 5.13) for piercing point at 80 km depth are plotted.

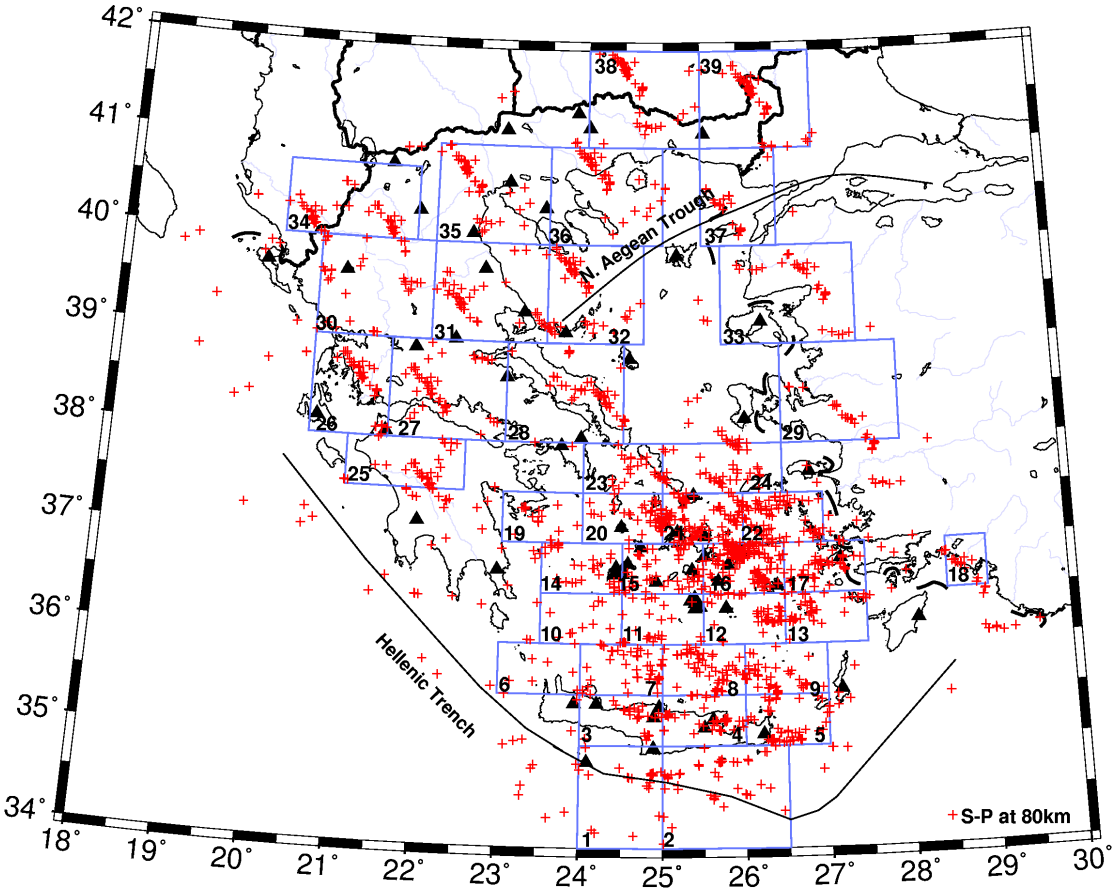

Fig. 5.16. The study area is divided into 39 non-overlapping boxes with respect to the Sp conversion points at 80 km. S receiver functions were computed for each box and a stacked S receiver function was obtained from many individual traces box by box.

Negative (positive) amplitudes, plotted in black (gray) indicate a velocity decrease (increase) with depth. A clear negative phase (labeled LAB) at ~ 12-25 s is apparent in sections D-E and is identified as a converted phase from the lithosphere-asthenosphere boundary. Figure 5.17 (D-F) show a consistent LAB phase beneath the Aegean to the continental Greece along different profiles. This phase is observed along profiles D and E located in the eastern and middle part of the Hellenic arc at a delay time of about 12 s under southern Crete, where it steepens significantly under the volcanic arc (Cyclades area) and arrives at about 25 s.

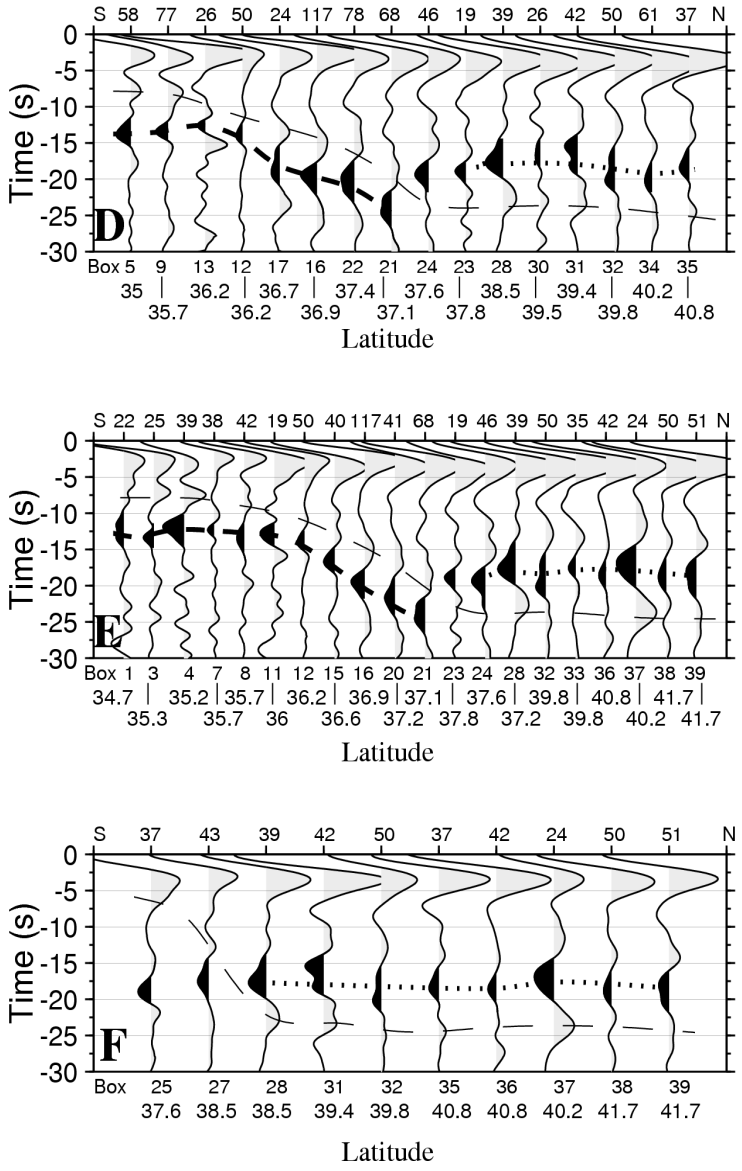

Fig. 5.17. Imaged lithosphere-asthenosphere boundary estimated by stacked S receiver functions, box by box, along profiles D-F (shown in Fig. 5.13). The box number and number of S receiver functions for each box are indicated in the lower and upper parts of the figures, respectively. The latitude of the center of the boxes are also shown below. Negative amplitudes of S receiver function (in black) show a velocity decreases with depth. Different types of dashed lines are used to demonstrate continental (dot-dashed) and oceanic (thick dashed) LAB. D) stacked S receiver functions, along profile D in eastern part of the trench, showing a clear negative phase dipping from 12-25 s beneath volcanic arc (box 21), which is interpreted as subducting African LAB. The continuity of LAB could not be imaged further north. Beneath northern Greece, LAB shallows to 17 s, interpreted as continental Aegean LAB. E) same along profile E in central part. F) same along profile F located in mainland Greece reliably shows the continental Aegean LAB at 17 s. The slab phase deduced from Fig. 5.14 & 5.15 is also shown with a thin dashed line, although it can not be well identified.

It shallows towards continental Greece and arrives at time of about 17 s. The observed slab phase deduced from Figures 5.14 & 5.15 can be also seen in the stacked S receiver functions, labeled with African Moho. Section F located in the western part of the arc, in mainland Greece reveals reliably another feature. A very strong negative phase at an almost constant time of 17 s can be significantly identified along this profile.

5.3 Discussions

In this part, the obtained results from P and S receiver functions are discussed and compared with the other current ideas in this region. They are also interpreted and finally three depth maps are presented for the crustal and upper mantle structure beneath the whole study area.

5.3.1 Thickness of the Lithosphere

The delay times of the LAB phase obtained from each box were converted into the depth by multiplication the arrival times of this phase with a factor of 9 using the IASP91 reference model. Figure 5.18 shows that in southern Crete as well as in the southern Aegean Sea the LAB is at about 100 km deep and dips down to 225 km towards central Aegean. Further north, beneath continental Greece, it thins to about 150 km. The average thickness of the lithosphere in the Mediterranean has been estimated to be 90 km (Papazachos, 1969; Payo, 1967,1969) for the Eurasian plate, although Calcagnile et al. (1982) showed that the lithosphere-asthenosphere boundary undulates between 90 and 120 km. The thickening of the LAB (from 100 to 225 km) towards the Aegean Sea can be interpreted as the subduction of the oceanic African lithosphere beneath the Aegean plate. Using S receiver functions, this boundary could be mapped up to the depth of 225 km.

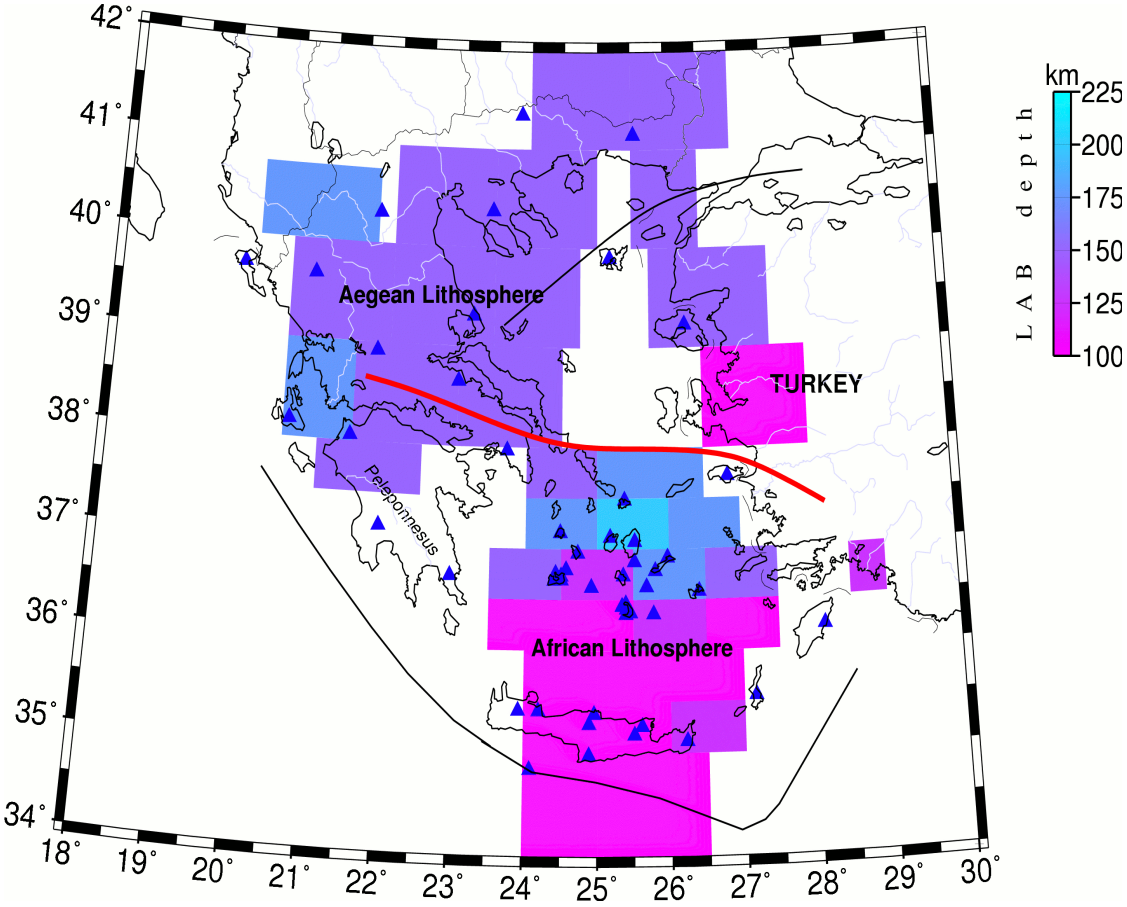

Fig. 5.18. The LAB depth map obtained from S receiver function analysis in Aegean. Time has been converted to depth using IASP91 reference model. The values are given in Table C.2, Appendix C. The heavy red line is a boundary separating the observed continental Aegean lithosphere from the oceanic African lithosphere.

The strong horizontal negative phase along profile F (Fig. 5.17), which is located at about 17 s above the slab phase in mainland Greece, is also interpreted as due to the continental Aegean lithosphere (Eurasian lithosphere), whose thickness is estimated to be about 150 km. It seems therefore that the African lithosphere is thinner than the Aegean (Eurasian) lithosphere at this place. This thicker lithosphere observed in the Aegean compared to Africa is surprising according to the large stretching (a factor of 2) accommodated since the Miocene (Le Pichon et al., 1982). However, most of the primary stretching affected the Sea of Crete where no information could be presented about the Aegean LAB. It may be also attributed to the crustal thickening across western and central Greece during the building process (Hellenides mountain range).

This difference in the LAB depth is therefore consistent with a localized stretching, affecting mostly the southern area of the Aegean, and different than the present day stretching evidenced in northern Aegean by GPS measurements.

5.3.2 Description of the Hellenic subduction zone

To calculate the slab depth from S receiver functions, an averaged delay time of the converted Sp phase due to the slab was determined from the stacked S receiver function obtained from each box and then transformed into a slab depth, using the IASP91 reference model. The delay times of the Sp conversions from the oceanic African Moho and computed slab depths are listed box by box in Table C.2, Appendix C. To construct a homogeneous slab depth map and image the geometry of the descending slab, slab depths obtained from both P and S receiver functions are used (Tables C.1 & C.2, Appendix C).

The results are demonstrated in Figure 5.19 and show the complex geometry of the subducted slab beneath the Aegean up to continental Greece. The depth of the slab is shallowest under western Peleponnesus, southern Crete and southeast of Rhodes and imaged at an average depth of about 40 km, it dips at various angles down into the Aegean Sea. It increases in depth to 160 km under the volcanic arc. Further north, beneath northern Greece, where no seismicity is related to this part of the slab, it is roughly horizontal at a depth of 220 km. Tomographic results (Spakman et al., 1988, 1993; Papazachos et al., 1995) show that the Benioff zone must extend as far north as the northern Greek border. The subducted slab obtained from tomography could be imaged down to 600km (Spakman et al., 1988) and even to 1200 km (Bijwaard et al., 1998) beneath northern Greece, even though the deepest earthquakes are located at depths of approximately 180 km in the eastern part of the trench. It seems therefore that the northern part of the slab is aseismic.

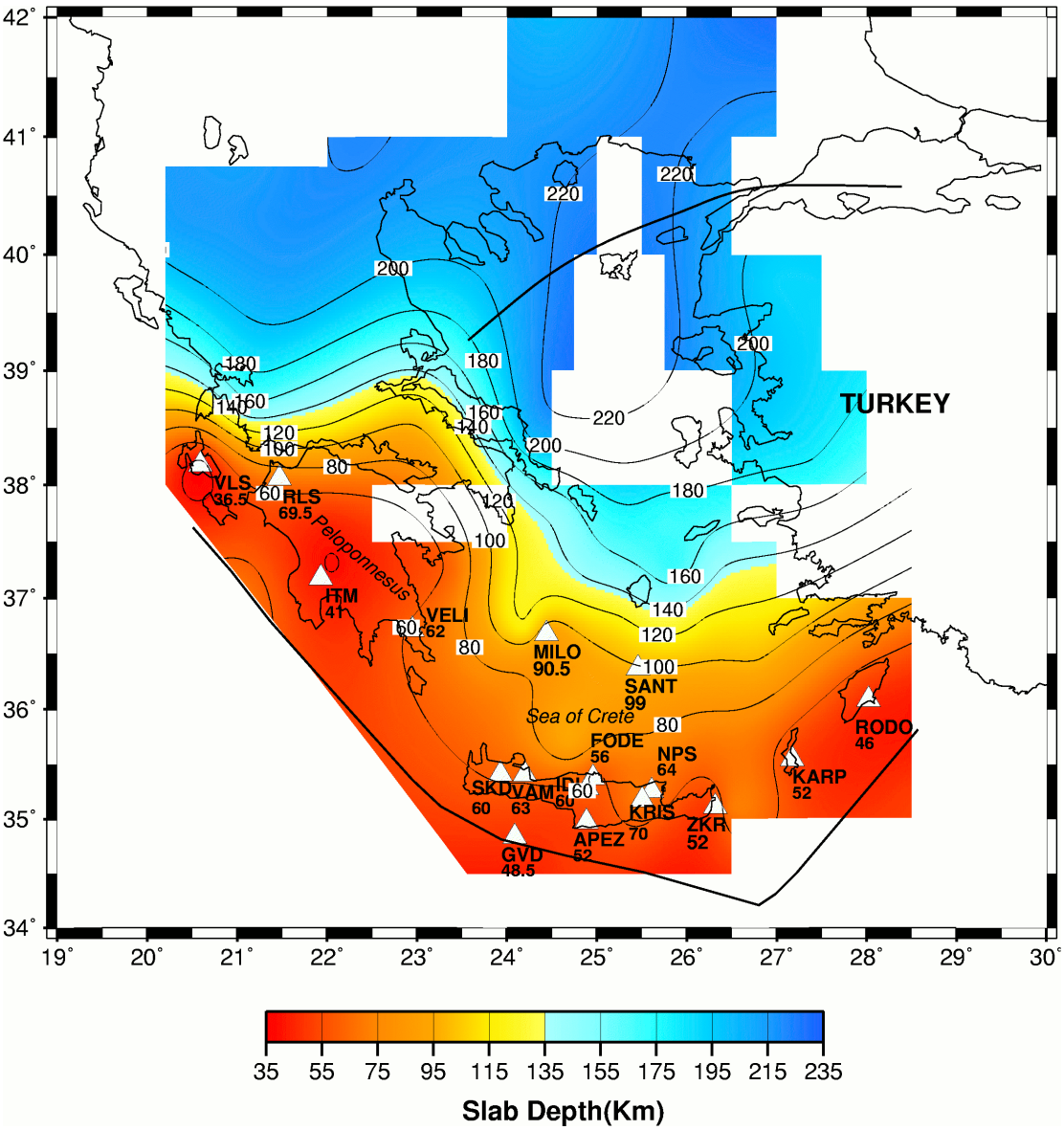

Fig. 5.19. Slab depth map obtained from both P snd S receiver functions. The slab depths for the stations (with clear Ps converted phase from slab) represented by triangles are computed using P receiver functions. The slab depths for the other parts of the area are obtained from the stacked S receiver functions, box by box. White boxes show the areas that not enough S piercing points are available.

It can also be argued that reheating of a downgoing slab can affect its rheological properties and limit, if not suppress seismicity (Wortel, 1982; Hatzfeld, 1994). Comparing the obtained results from this study with the results deduced from tomography may imply that receiver functions may only image the shallow dipping part of the slab down to 200 km.

Furthermore, the observed curvature of the slab seems to be less bent as we go deeper and northward suggesting that the subduction was more linear when it started. This supports the idea that subduction has migrated from the northern Aegean to its present position since Eocene (De Jonge et al., 1993).

The subducted slab is observed much deeper and also steeper in the eastern part in comparison with the western part of the arc, as Figure 5.19 shows. The slab is almost horizontal beneath the western part and observed at depth of ~ 50-60 km under Peleponnesus, it steepens strongly into the northern Aegean Sea and reaches a depth of approximately 200 km. This result is also consistent with the shallow seismicity recorded beneath the Peleponnesus (Hatzfeld et al., 1989; Papazachos et al., 2000).

The observed change in the slope of the slab is in good agreement with independent results in this area. Detailed tomographic results for this region (Papazachos & Nolet, 1997) confirm the change in dip within different parts of the subduction. Hatzfeld & Martin (1992), Hatzfeld et al, (1993), Papazachos et al. (2000) imaged the Wadati-Benioff zone in this area and showed that it dips at shallower angle in the west contrary to the eastern part. It seems also that the subduction occurs easierly in the eastern part, leading to a rapid sinking of the African plate beneath eastern part of the arc in accordance with GPS measurements, which showed a trenchward motion in the southeastern Aegean of 10 mm/yr relative to the whole southern Aegean (McClusky et al., 2000).

It is apparent from results of this study that there is no large tear in the slab resolved by S and P receiver functions. However, due to the lack of the seismological stations in the northern Aegean Sea, the continuity of the slab could not be imaged.

Regarding Figure 5.19, the slope of the slab varies laterally, as well as vertically northward. The lateral change in slope towards the eastern part of the subduction zone can be shown to be significant beneath the volcanic arc. A notable difference can be observed between the western and eastern part of the Cretan Sea, where the subducted slab is much deeper in the western part.

However, Spakman et al. (1988) found a continuous subducting slab along middle part of Hellenic arc, whereas they observed a tear at a depth of about 200 km beneath the

northern Aegean Sea and Greece. The observations of this study confirm the existence of a continuous slab beneath the middle part of the Hellenic arc and in contrast to Spakman et al. (1988) shows no tear in the downgoing slab beneath Greece and Peleponnesus.

The main difference in slope, interpreted as a kink at a depth of about 75-95 km along the western profile, reported by the tomographic images of Papazachos & Nolet (1997), can also be clearly seen by cross-sections C and F shown in Figures 5.14 & 5.15. This study confirms therefore the very shallow dipping slab (slope less than 10°), evidenced as far as northern Greece, that was mapped by Papazachos and Nolet (1997) and at shallower depth than proposed by Spakman et al. (1993).

5.3.3 Reversed continental Moho contrast complication

The derived S receiver function sections, as shown in Figures 5.14 & 5.15, present a clear normal Moho contrast (i.e. with positive amplitude) in the forearc area. To obtain a complete picture and look for the origin of the negative Ps converted phase in Crete, P and S receiver functions recorded in four stations are selected and compared; three of these stations are located in the forearc (SKD, IDI, NPS) and one of them in continental Greece (PLG). P and S receiver functions are then stacked and filtered using the same bandpass filter of 4-20 s. Figure 5.20 shows the computed P and S receiver functions for the four selected stations. However, only Ps and Sp conversions close to each station are selected in order to resolve the same structure beneath each area. Positive amplitudes are plotted in black. On both Ps and the Sp plots, the bold vector indicates the converted phase at the continental Moho, and the thin vector shows the converted phase from the subducted oceanic Moho for stations located along the Hellenic trench. As the Figure shows, no positive amplitude Moho conversions are seen on the P receiver function data at the three selected stations located at the forearc. Instead, strong converted phases with notable negative amplitudes appear at delay times of 3-4 s (marked with bold vector).

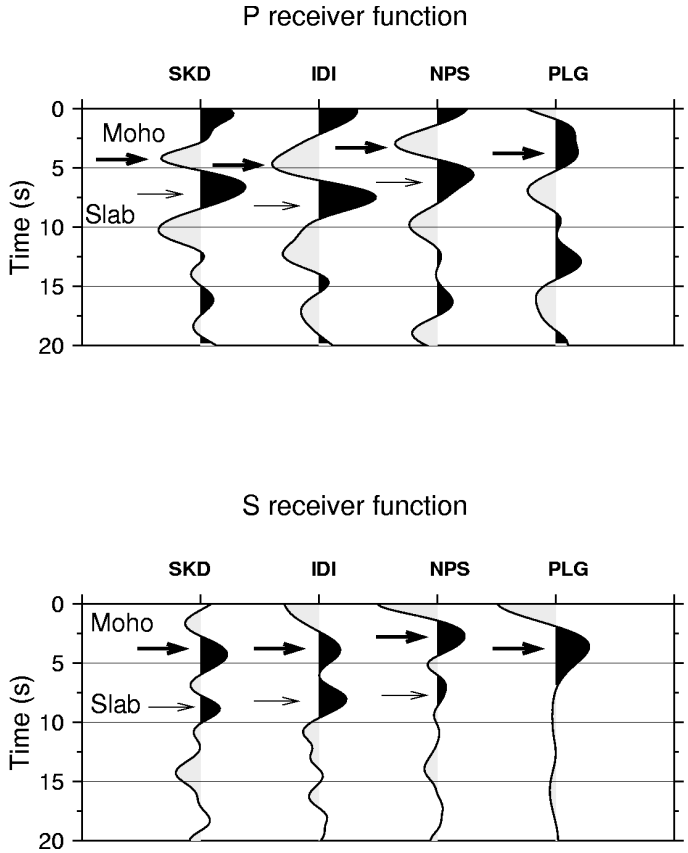

Fig. 5.20. Comparison of P and S receiver functions for four selected stations in order to check their compatibility. Stacked P receiver functions in upper panel show notable negative conversions, indicated with bold arrows at expected Moho times for stations located in the forearc (SKD, IDI, NPS), while this conversion is positive for station PLG in mainland Greece. The interpreted slab phase is indicated with thin arrows. Stacked S receiver functions in lower panel show clear positive conversions at expected Moho times for all four stations. Both type of receiver functions show positive amplitudes for the slab phase. The small difference in arrival times of the slab phase is due to the different locations of the P and S piercing points.

This negative amplitude for P receiver functions recorded in Crete has been a subject of debate. Knapmeyer et al. (2000) interpreted the weak negative signal recorded in western Crete as due to a thick fossil accretionary wedge. Li et al. (2003) interpreted the negative phase recorded in western and northern central Crete as due to a reversed Moho velocity contrast caused by a large amount of serpentinite in the mantle wedge.

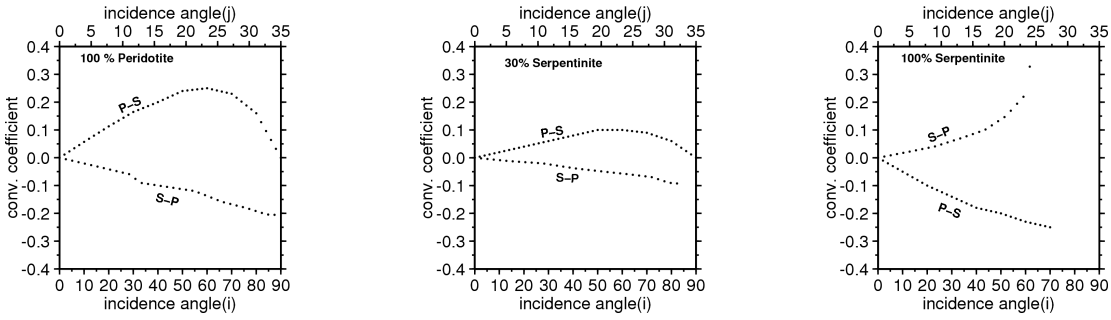

(a) (b) (c)

Fig. 5.21. Calculated Ps and Sp conversion coefficients for different uppermost mantles. a) those for a normal crust overlain by 100% peridotite uppermost mantle. b) if the uppermost mantle consists of 30% serpentinite. c) for a completely serpentinized uppermost mantle, note that the values are reversed and Ps conversion coefficients are no longer positive.

Finally, Endrun et al. (2004) concluded that beneath western Crete a thick crust extends down to the oceanic lithosphere.

Using the combination of both P and S receiver functions results in discrimination between different models. The stacked S receiver functions obtained from three stations at the forearc reveal, contrary to the computed P receiver functions, the presence of a normal Moho contrast beneath these stations. Furthermore, although the Moho converted phases reveal different polarities for P and S receiver functions for stations located at the forearc, they have the same polarity for the station located on mainland Greece and arrive at the same time. We consider three different crust-mantle contrasts (Hacker, 2003) and calculate their corresponding Ps and Sp conversion coefficients (Fig. 16). A normal crust overlain by 100% peridotite uppermost mantle shows a positive Ps and a negative Sp conversion coefficient. If the uppermost mantle contains 30% serpentinite, Ps conversion coefficients tend to have smaller values, while those of Sp increase. It is interesting to note that for a completely serpentinized uppermost mantle the values are reversed, Ps conversion coefficients become negative and those of Sp are positive. Therefore, a large amonut of serpentinite (larger than 30%) can provide a negative Ps conversion coefficient leading to a negative amplitude Ps conversions in the forearc.

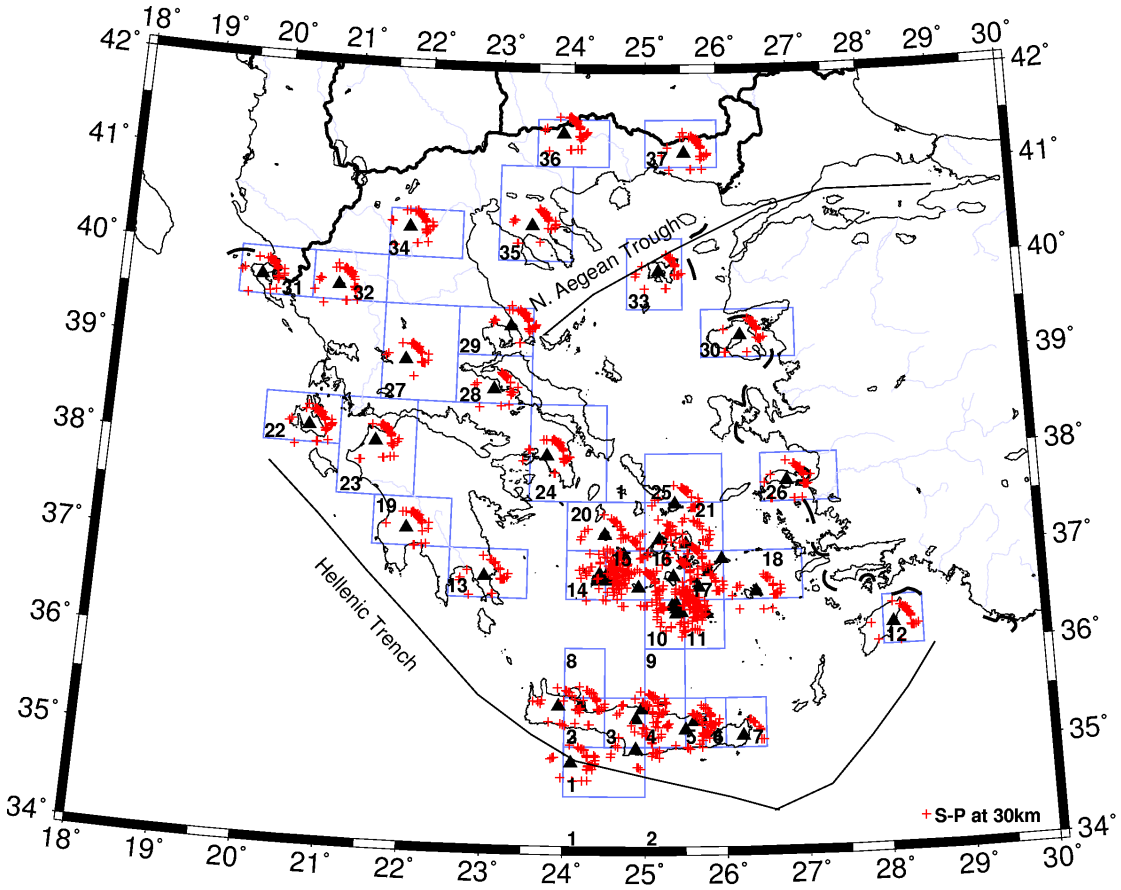

Fig. 5.22 The study area is divided into 37 boxes with respect to the Sp conversion points at 30 km. S receiver functions were calculated for each box and a stacked S receiver function was obtained from many individual traces box by box. The delay times of Sp conversions from Moho were converted into depth using IASP91 reference model.

It may concluded from these calculations that 50-60% serpentinization in the forearc could result in a negative contrast for P-to-S conversion, even though the Sp conversion coefficient remains negative.

5.3.4 Crustal thickness of the Aegean plate

Moho depth values obtained from P receiver functions (Table C.1, Appendix C) are complimented by using the stacked S receiver functions in each box shown in Figure 5.22 Figure 5.22 shows the distribution of Sp piercing points at 30 km (average depth of the Moho).

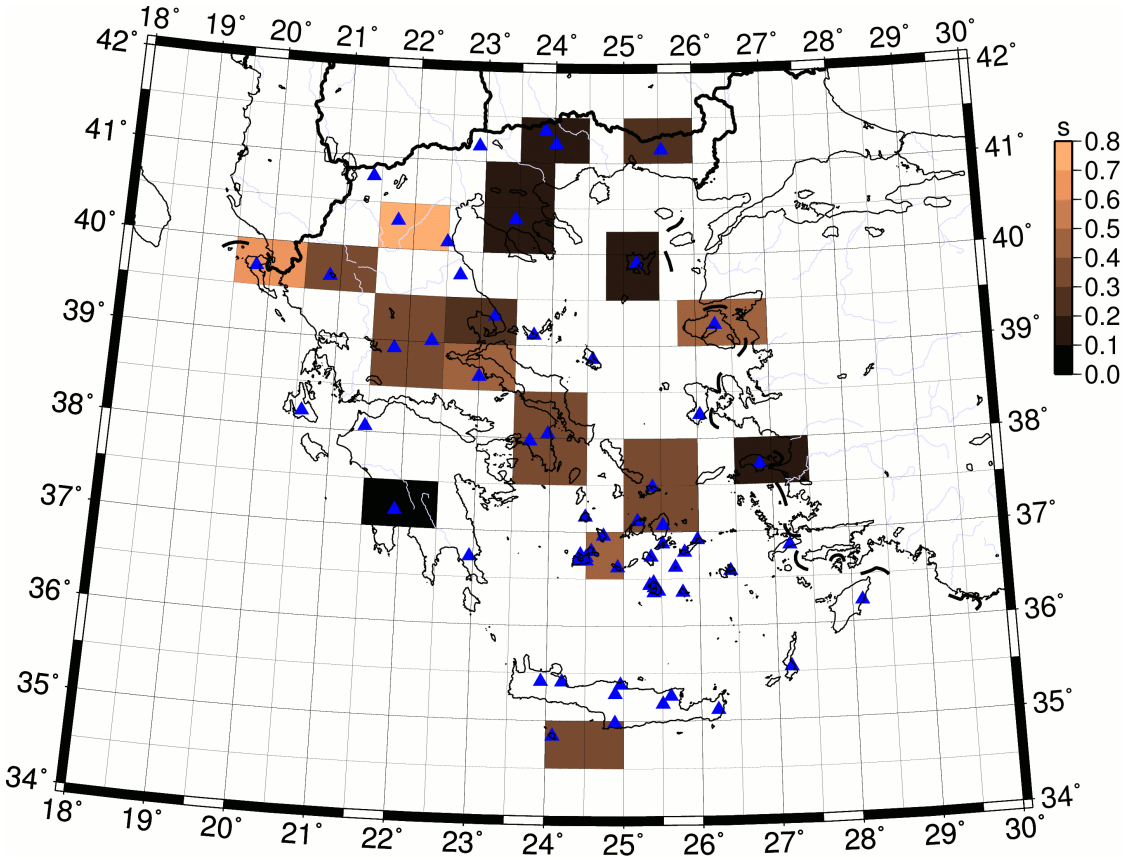

Fig. 5.23. Estimated time differences of the positive conversions at Moho obtained from P and S receiver functions. The maximum difference (0.7 s or ~ 6 km) is observed for western coast of Greece.

By combining both the P and S receiver function results, a more detailed, homogeneous map of the Moho depth for the whole Aegean area can be proposed.

The Moho depth is evaluated by converting the delay times of the Sp Moho phases into depth using a crustal Vp velocity of 6.2 km/s and Vp/Vs ratio of 1.73. These values are also listed in Table C.3, Appendix C. To propose a Moho depth map two factors need to be considered. First, it has to be checked that the Moho depths calculated from P receiver functions beneath each station agree with the depths computed from stacked S receiver functions for each box encompassing the station. This goal was achieved by calculating the time difference between the estimated Ps and Sp converted phases from the Moho boundary. Figure 5.23 shows the calculated time differences for the areas where a normal Moho contrast was seen using both methods.

Regarding Figure 5.23, the time differences are small and vary between 0-0.7 s (i.e. less than ~ 6 km in depth) and usually less than 0.4 s (~ 3 km), which is within our uncertainties. Second, a homogeneous map using both P and S receiver functions are built. For all stations in the back arc area, the Moho depths calculated by P receiver functions are used, because they are clear and more precise. For stations in the forearc region, where no positive Ps converted Moho phase could be determined, S receiver functions were utilized. Furthermore, due to the wider lateral distribution of piercing points for the S receiver functions compared to those of P receiver functions as well as the overlap of S piercing points from neighbor stations in some areas, a better coverage between stations is achieved.

All Moho depth estimates obtained from both P and S receiver functions (Tables C.1 & C.3, Appendix C) are used to generate a Moho map. The results are also complemented using Moho depths from 3 stations in Turkey (Saunders et al., 1998). However, to present a Moho depth map, the P receiver function results of some stations needs to be discussed as follows.

5.3.4.1 The observed Moho phase beneath PENT and ATH

Figure 5.24 shows the computed P receiver functions for two neighbor stations, PENT and ATH located in mainland Greece. Considering arrival times of the converted Ps phase from the Moho, the observed difference seems to be large for neighbor stations (3.1 s for ATH and 4.5 s for PENT). However, the computed stacked S receiver function obtained from box 24 includes this area (Fig. 5.22) and shows a Moho depth of about 28 km. This value is in good agreement with the computed Moho depth from P receiver functions for station ATH (~ 26 km). Due to the sparse data recorded at station PENT (24) and to the large difference in the computed Moho depth relative to its neighbor station ATH, the depth estimate from this station is not used in the Moho map, because it seems unrealistic to have such large offset in the Moho considering the gravity map.

5.3.4.2 Presence of thick Moho under SANT

For the stations MILO and SANT, located on the volcanic islands in the Cyclades region, two similar phases at about 2.5 and 4.5 s (i.e. ~ 20 and 36 km) are seen in the P receiver functions. Both of these phases arrive within the expected Moho delay time and appear to be stable and coherent (Fig. 5.25). The obtained S receiver functions from the corresponding boxes including SANT and MILO (boxes 10 and 15) seem different. The computed Moho depth from box 15 shows a Moho depth of 33 km (at ~ 4 s), while box 10 reveals a Moho at the depth of approximately 25 km (~ 3 s). As Figure 5.22 shows the distribution of the Sp piercing points in box 10 can not well cover the station SANT. Therefore the second phase in the P receiver functions is interpreted as the converted Moho phase, it shows however a larger amplitude than phase 1 at station SANT. It is suspected that phase 1 is produced by multiple scattering from sediment and upper crustal layers, that are usually present under

volcanic islands.

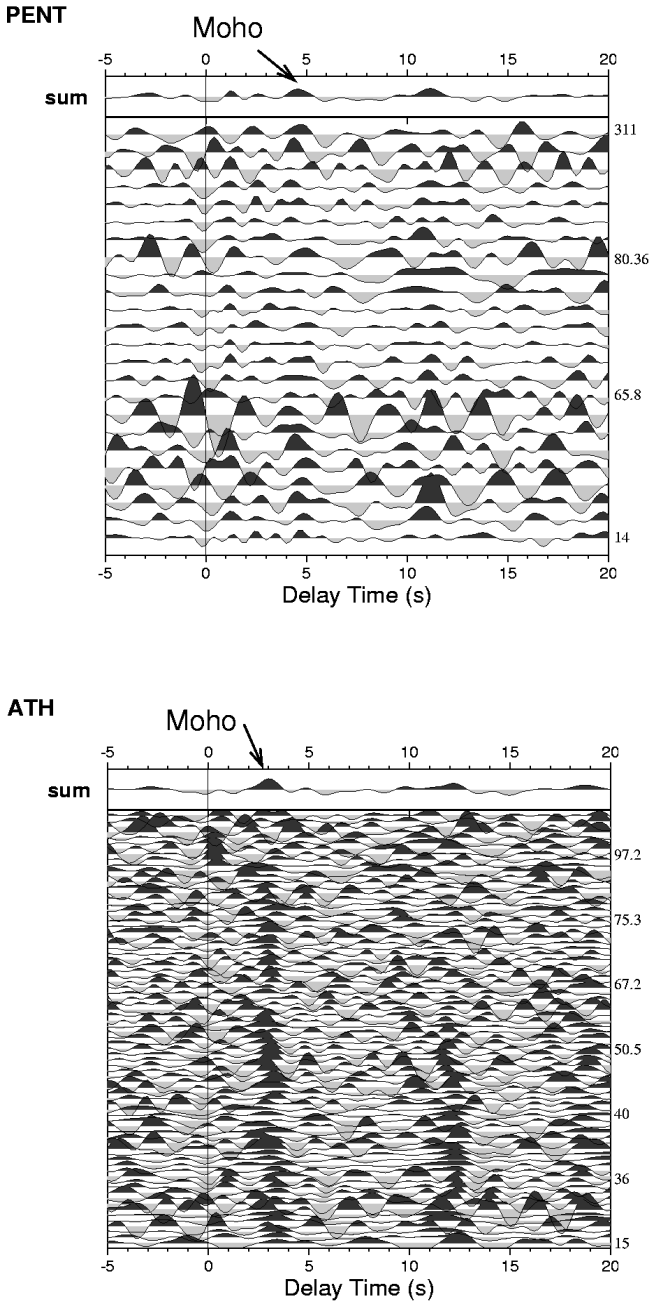

Fig. 5.24. Individual P receiver functions sorted after back azimuth (shown in the right) for two neighbor stations PENT and ATH in mainland Greece. The Ps converted phases from Moho observed at 4.5 and 3.1 s, respectively. This difference seems to be large. Although PENT shows sparse data compared to ATH.

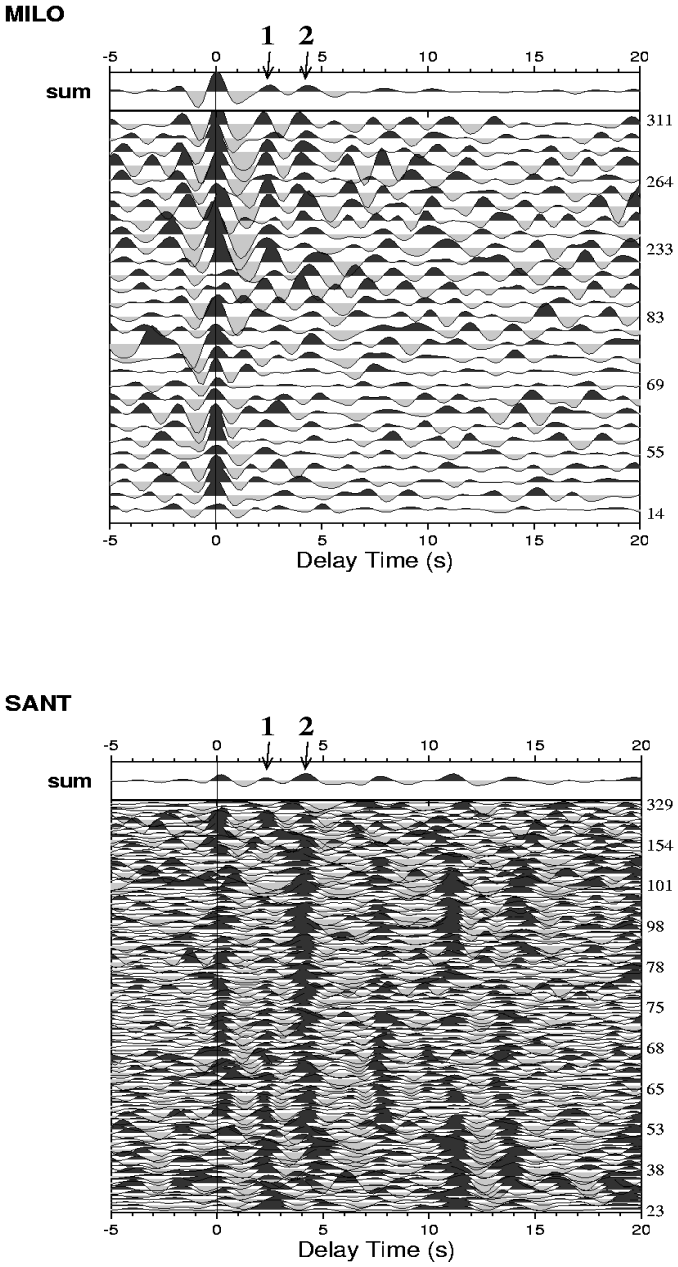

Fig. 5.25. Individual P receiver functions for two stations located on the volcanic islands of Cyclades region are sorted after back azimuth. Receiver function data show two coherent phases between 2-4 s labeled with 1 and 2, respectively. Regarding multiple scattering obtained from sediment and upper crustal layers presented in volcanic regions, phase 2 in interpreted as due to the Moho.

Li et al. (2003) observed significant energy on the transverse component at station SANT, which correlates well with the converted Moho phase at 4.2 s on the radial component. They interpreted this observation as due to an anisotropic crustal structure. They also showed that the boundary at 25 km depth may be related to the Moho of the Aegean subplate which overlies a thinned remnant of the Cretan microcontinent whose lower boundary (Moho) is located at 34 km.

5.3.4.3 Moho depth map

A map of the Moho depth that summarizes the results of this study is presented in Figure 5.26. A crust of approximately 32-38 km is observed beneath western Greece along the Hellenides mountain range. The correlation of thick crust and the remarkably high elevation beneath western Greece indicates an isostatic crustal balance, implying a distributed crustal thickening as the main mechanism of the crustal thickening in this area. This estimation of the crustal thickness is however less than previous studies for this region, where depths were indicated to be ~ 40-46 km (Makris, 1976; Ligdas & Lees, 1993; Papazachos, 1998; Tiberi et al., 2000; Karagianni et al., 2002, 2005).

Moving toward the west coast of the Aegean Sea, the crust thins to the depth of 28-30 km consistent with the result of Makris (1978) beneath Evia. This thin crust is likely to be due to the extension tectonics that affected the whole Aegean and adjacent areas.

The crustal thickness under the Peleponnesus is estimated to be about 25-28 km, since the first phase at 3-3.5 s (shown in Fig. 5.14(C), 5.15(F)) as the converted phase from the Moho discontinuity is reliably assumed. Rather than a Moho at a depth of 45 km as suggested by other authors (Karagianni et al., 2002; van der Meijde et al., 2003; Karagianni et al, 2005), it is suggested by this study that the second phase at about 4.5-5 s delay time defines the oceanic Moho of the subducting plate beneath the Peleponnesus as also suggested by the seismicity reported for this area.

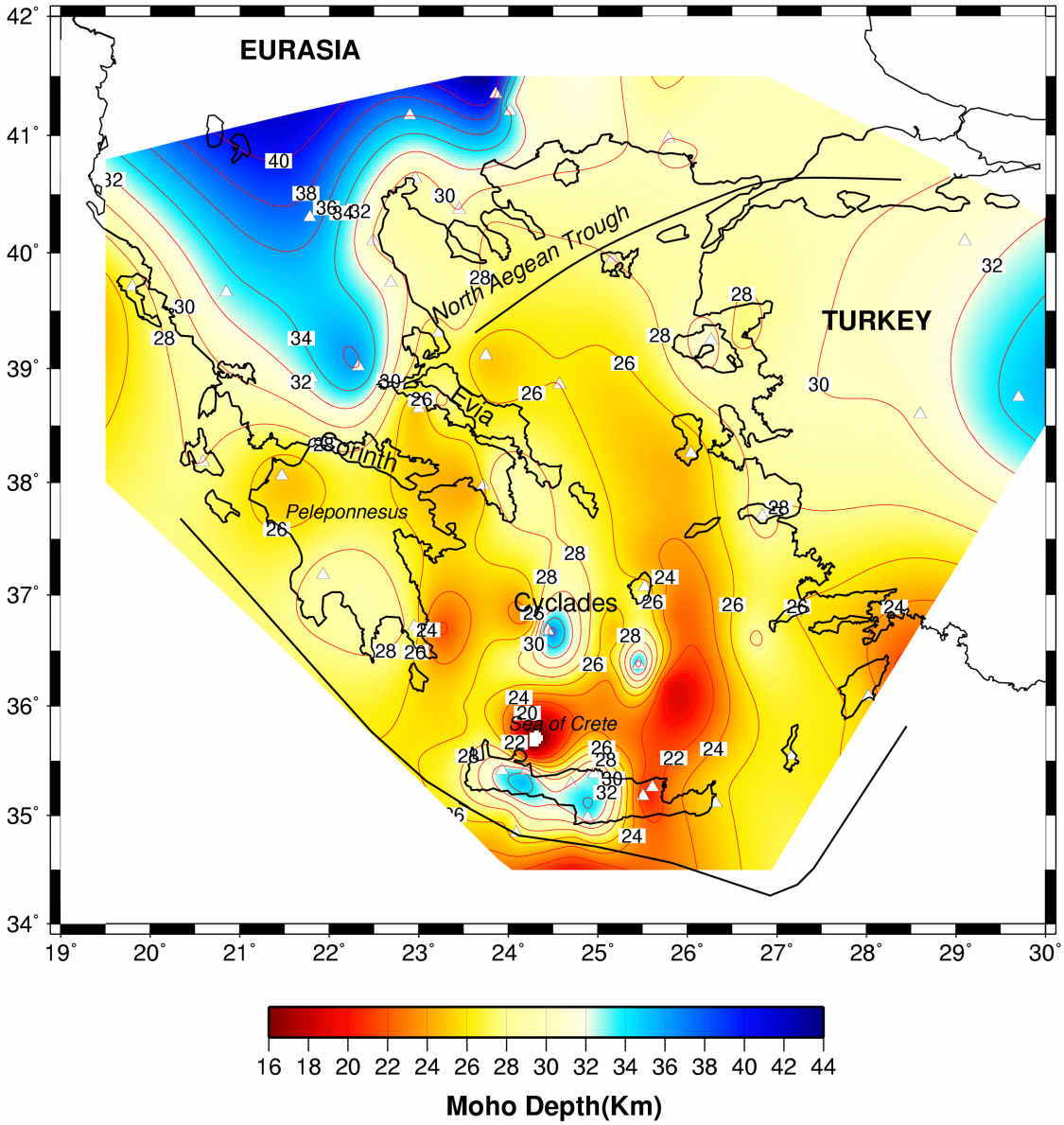

Fig. 5.26. The Moho depth map (in km) deduced from P and S receiver functions. The Moho depth values of three stations are from Saundres et al. 1998. The Moho depths used for this map are listed in Tables C.1 & C.3, Appendix C.

The resulted Moho depth estimates a crustal thickness of 25-29 km beneath Evia and Corinth Gulf, north of Peleponnesus, which are consistent with the Moho depths derived from inversion of gravity anomaly data by Tiberi et al. (2001). In the northern Aegean, a region that has undergone crustal extension since the Eocene, a thin crust of approximately 25-28 km is imaged.

Travel time (Papazachos, 1998) and shear wave velocity (Karagianni et al., 2005) tomographies also show a thin crust in this area. Wide angle reflection profiles, conducted in the Sporades Basin(near station SKOP) show a Moho depth at about 25 km (Vigner, 2002).

Beneath the southern Aegean Basin, a very thin crust of about 20-22 km is observed, which reaches 26 km eastwards. These results are also in good agreement with Moho depths obtained from seismic profiles (Makris, 1978; Bohnhoff et al., 2001), shear wave velocity tomography (Karagianni et al., 2005) and receiver function analysis (van der Meijde et al., 2003) for this region. Such a thickness would indicate significant thinning of the crust within this area in comparison to the northern Aegean area. The absence of large thinning associated with the North Aegean Trough, that is a region with the highest present day strain rate computed by GPS measurements, confirms a recent evolution in the geodynamics of the North Aegean Trough suggested by Armijo et al. (1996).

A thicker crust is observed beneath the central Aegean across the Cyclades region. The Moho depth in this part is estimated to be about 25-30 km. Refraction data (Makris, 1978, Vigner, 2002) indicated a Moho depth of about 28 km in this region. These values may confirm the idea that the Cyclades act such a rigid block which do not stretch during the second episode of the extension (which affects significantly the northern Aegean Sea). However, the crustal thickness displays a sudden thickening beneath stations MILO and SANT on the volcanic islands and reaches depths to 36 and 34 km, respectively. This value has been already suggested by Li et al. (2003) beneath station SANT, and is consistent with results derived from gravity studies in this region (Tirel et al., 2005).

A large difference in Moho depths has been reported beneath the island of Crete (Bohnhoff et al., 2001; Li et al., 2003). Makris (1978) showed an average depth of about 30-32 km beneath Crete, whereas Bohnhoff et al. (2001) revealed a crustal thickness of approximately 32 km in the central Crete which thins to 24 and 26 km eastwards and westwards, respectively. Li et al. (2003) showed that crustal thickness varies between 31-39 beneath the island of Crete. The observations of this study are

concluded that the crustal thickness beneath western and central Crete is estimated to be about 30-33 km and thins to 21-25 km under the eastern part of this island.

Based on this study, the stretching scenario in the Aegean will be modified in the way that a thinner crust is inferred as the unstretched crust in mainland Greece (32-38 km) and therefore suggested a stretching factor of 20-25% in the northern Aegean and 40-45% in the Cretan Sea. It seems also, contrary to the previous works, that a low to moderate extension has occurred in the whole region (Makris, 1978; Angelier et al., 1982). The resulted Moho map fits well in the sea with the inferred gravity map (Tsokas & Hansen, 1997; Tirel et al, 2005), however it is smoother than what is expected from tectonics. The Moho estimations reliably show that the continental crust along Hellenides mountains beneath Peleponnesus and Crete were also affected by the extension occurred in the Aegean, consistent with the GPS results in the southern Aegean (McClusky et al., 2000).

However, not similar reactions of the different parts of Crete to the extension resulted in a thicker crust in its western block. No NE-SW trend associated with the North Aegean Trough as inferred by gravity (Tirel et al., 2005) is observed by this study and may indicate that the North Aegean Trough is only a superficial feature not affect really the crustal thickness beneath this area. Finally, the relatively smooth Moho topography in the northern Aegean Sea (excluding MILO and SANT, whose thicknesses are related to the volcanic structure) is suggested from this study that varies between 25-29 km. This favors a “ductile” tectonic type for the extension instead of a chaotic horst and graben extension type.

CHAPTER 6

CONCLUDING REMARKS

By combining P and S receiver functions from the Aegean and Greece, a joint P and S receiver function analysis is performed that allows sampling seismic boundaries at sea with data from nearby land stations. Using this joint P and S receiver function analysis, for 65 permanent and temporary stations covering the whole Aegean area, resulted in a direct, homogeneous and detailed Moho map for the continental Aegean and subducting oceanic African plates. Due to the wider distributions of the Sp conversions, the receiver function technique allows a better resolution in space than surface waves and a direct measurements contrary to gravity anomaly interpretation. Furthermore, applying the new technique of S receiver function led to imaging of the Lithosphere-Asthenosphere Boundary for the first time in this area and discussed further the reversed Moho contrast complication in the forearc area of the subduction.

6.1 Crust-mantle boundary of the Aegean plate

Strong variations of the crustal thickness are demonstrated by this study in the Aegean. A thickness of approximately 32-38 km was observed beneath western Greece along the Hellenides mountains showing the unstretched crust in this area, whereas northern Greece and eastern part of continental Greece were stretched by the extension that occured within the whole Aegean and therefore shows a crustal thickness of 28-30 km. The observed thicker crust in western Greece is reliably related

to the crustal thickening resulted from isostatic compensation of the mountain range in this part. A very thin crust (20-22 km) restricted to the southern Aegean clearly shows 40-45% crustal thinning caused by the extension tectonics of the Aegean back arc area, which has been started since early Miocene and was great in the southern Aegean. This extension also affected the Peleponnesus and the island of Crete. Crustal thicknesses of 25-28 and 25-30 km for Peleponnesus and Crete respectively reveal the stretched crust beneath this area. However, presence of thicker crust beneath the western block of the Crete shows the different reaction of this block to the extension relative to the eastern part of Crete. Moderate crustal thinning of about 20-25% observed in northern Aegean shows the second episode of the extension, which was significant in northern Aegean along the North Anatolian Fault and resulted in 25-28 km crustal thickness for this region. The thicker crust of the rigid block of Cyclades (~ 25-30 km) confirms that this part was not involved in the second episode of extension. The discrepancy between the present day strain rate deduced from GPS measurements located mostly in the North Aegean Sea and the variation in the crustal thickness obtained from this study shows that the present day kinematics is recent.

6.2 Crust-mantle boundary of the African plate

The high resolved African Moho deduced from over 5000 observations of P and S receiver functions led to a homogeneous and detailed map of the subducted slab beneath the whole area. The African Moho is followed from western Peleponnesus, southern Crete and southeast of Rhodes at a depth of 40 km down to the depth of 160 km beneath volcanic arc and to 220 km under northern Greece, while P receiver functions could map it only down to 100 km beneath volcanic arc. The observed seismicity located only in the shallower part of the slab (~ 180 km) shows that the northern part of the slab is aseismic. The resulted image of the Hellenic subducted slab shows the characteristics of the slab laterally as well as vertically within the region.

The geometry of the slab is relatively complex. The western part of the subduction is much shallower than the eastern part, it is horizontal beneath Peleponnesus and observed at depth of about 50-60 km, it shows a sudden dipping to a depth of 200 km beneath northern Greece, while the slab dips steeply in the eastern part beneath the Dodecanese islands. This rapid sinking of the eastern segment of the arc shows that subduction occurs easier in this part in comparison with the western part of the arc. The slab shows a more linear form at the beginning of subduction compared with the present-day form, which is almost bent. This could be related to the two episodes of extension, which affected the whole Aegean region.

6.3 LAB beneath the whole area

The lithsphere-asthenosphere boundary could be well resolved using the new technique of S receiver function. The obtained oceanic lithosphere of the subducting African plate is 100 km thick beneath the southern Crete and southern part of the Aegean, it thickens beneath the volcanic arc where it reaches about 225 km. However, the depth of the oceanic lithosphere could not be imaged under mainland Greece. Beneath western and northern Greece, the continental Aegean lithosphere (Eurasian lithosphere) lies above the downgoing oceanic plate and is observed at about 150 km depth, this thickness may be related to the crustal thickening reported in this area.

References

Alessandrini, B., Beranzoli, L., Drakatos, G., Falcone, C., Karantonis, G., Mele, F. M. & Stavrakakis, G. (1997). Back Arcs Basins and P-wave Crustal Velocity in the Ionian and Aegean Regions, Geophys. Res. Letts., **24**, 5, 527-530.

Allan, T. D. & Morelli, C. (1971). A Geophysical Study of the Mediterranean Sea, Boll. Geofis. teor. ed appl., **13**, 50, 99-142.

Alptekin, Ö., Ilkisik, O. M., Ezen, Ü. & Üçer, S. B. (1990). Heat Flow, Seismicity and the Crustal Structure of Western Anatolia, IESCA-1990 Proceedings, 1-12.

Ambraseys, N. N. & Jackson, J. A. (1990). Seismicity and Assiciated Strain af Central Greece Between 1890 and 1988, Geophys. J. Int., **101**, 663-708.

Ambraseys, N. N. & Tchalenko, J. S. (1970). The Gediz (Turkey) Earthquake of 1970 March 28th., Nature, **227**, 592-595.

Ammon, C. J. (1991). The isolation of receiver effects from teleseismic P waveforms, Bull. Seism. Soc. Am. **81**, 2504-2510.

Anderson, H. & Jackson, J. (1987). Active Tectonics of the Adriatic Region., Geophys. J. R. Astron. Soc., **91**, 937-983.

References

Angelier, J. (1979). Recent Quaternary tectonics in the Hellenic arc: examples of gelogical observations on land, Tectonophysics, **52**, 267-275.

Angelier, J. & Le Pichon, X. (1980). Neotectonique Horizontale et Verticale de I Egee: Subduction et Expansion., Geologie des Chaines Alpines Issues de la Tethys. Int. Geol. Congr., 26th, Paris -Mem. B. R. G. M., **115**, 249260.

Angelier, J., Lyberis, N., Le Pichon, X., Barrier, E. & Huchon, P. (1982). The neotectonic development of the Hellenic arc and the Sea of Crete: a synthesis, Tectonophysics, **86**, 159-196.

Armijo, R., Meyer, B., King, G., Rigo, A. & Papanastassiou, D. (1996). Quaternary evolution of the Corinth Rift and its applications for the late Cenozoic evolution of the Aegean, Geophys. J. Int., **126**, 11-53.

Aubouin, J. (1959). Contribution a l' etude geologique de la Grece septentrionale: les confins de l' Epire et de la Thessalie, Ann. Geol. Pays Hellen., **10**, 483pp.

Barton, M., Salters, V. & Huijsmans, J. (1983). Sr-isotope and Trace Element Evidence for the Role of Continental Crust in Calc - Alkaline Volcanism on Santorini and Milos, Aegean Sea, Greece., Earth Planet. Sci. L, **63**, 273-291.

Berckhemer, H. & Kowalczyk, G. (1978). Postalpine Geodynamics of the Peloponnesus., Alps, Apennines, Hellenides (Eds: H. Cloos et al.). Schweizerbart, Stuttgart.

Bijwaard, H., Spakman, W., Engdahl, E. R. (1998). Closing the gap between regional and global travel time tomography, J. Geophys. Res. **103**, 30055-30078

Bock, G. (1991). Long-period S to P converted waves and the onset of partial melting beneath Oahu, Hawaii, Geophys. Res. Lett., **18**, 869-872.

Bohnhoff, M., Makris, J., Papanikolaou, D., and Stravakakis, G. (2001). Crustal investigation of the Hellenic subduction zone using wide aperture seismic data, *Tectonophysics*, **343**, 239-262.

Bostock, M. G., Hyndman, R. D., Rondeny, S. & Peacock, S. M. (2000). An inverted continental Moho and serpentinization of the forearc mantle, Nature, **417**, 536-538.

Bourova, E., Kassaras, I., Pedersen, H. A., Yanovskaya, T., Hatzfeld, D. & Kirtazi, A. (2000). Constraints on absolute S velocities beneath the Aegean sea from surface wave analysis, *Geophys. J. Int.,* **160**, 1006-1019.

Briqueu, L., Javoy, M., Lancelot, J. R. & Tatsumoto, M. (1986). Isotope Geochemistry of Recent Magmatism in the Aegean Arc: Sr, Nd, Hf, and O Isotopic Ratios in the Lavas of Milos and Santorini - Geodynamic Implications., Earth Planet. Sci. L, **80**, 41-54.

Brooks, M., Clews, J. E., Melis, N. S. & Underhill, J. R. (1988). Structural development of Neogene basins in western Greece, Basin Research, **1**, 129-138.

Brooks, M. & Kiriakidis, L. (1986). Subsidence of the North Aegean Trough: An alternative view, J. geol. Soc. Lond., **143**, 23-27.

Cassidy, J. F. (1992). Numerical experiments in broadband receiver function analysis, Bull. Seism, Soc. Am., **82**, 1453-1474.

References

Calcagnile, G., D'Ingeo, F., Farrugia, P. & Panza, G. F. (1982). The lithosphere in the central-eastern Mediterranean area, Pure Appl. Geophys., **120**, 389-406.

Caputo, M., Panza, G.F. & Postpischl, D. (1970). Deep Structure of the Mediterranean Basin., J. Geophys. Res., **75**, 4919-4923.

Christodoulou, A. & Hatzfeld, D. (1988). Three-dimensional crustal and upper mantle structure beneath Chalkidiki (northern Greece), Earth planet. Sci. Lett., **88**, 153-168.

Clément, C., Sachpazi, M., Charvis, P., Graindorge, D., Laigle, M., Hirn, A. & Zafiropoulos, G. (2004). Reflection-refraction seismic in the Gulf of Cornith: hints at deep structure and control of the deep marine basin, Tectonophysics, **391**, 97-108

Comninakis, P. E. & Papazachos, B. C. (1980). Space and Time Distribution of the Intermediate Focal Depth Earthquakes in the Hellenic Arc., Tectonophysics, **70**, 35-47.

Delibasis, N., Makris, J. & Drakopoulos, J. (1988). Seismic investigation of the crust and the upper mantle in western Greece, Annal. Geol. Pays Hell., **33**, 69-83.

De Jonge, M. R., Wortel, M. J. R. & Spakman, W. (1993). Form tectonic reconstruction to upper mantle model: An application to the Alpine-Mediterranean region, Tectonophysics, **223**, 53-65.

De Mets, C., Gordon, R. G., Argus, D. F. & Stein, S. (1990). Current plate motions, Geophys. J. Int., **101**, 425-478.

Drakatos, G. & Drakopoulos, J. (1991). 3-D velocity structure beneath the crust and upper mantle of the Aegean sea region, Pure appl. Geophys., **135**, 401-420.

Ekstrom, G. & England, Ph. (1989). Seismic strain rates in regions of distributed continental deformation, J. Geophys. Res., **94**, 10231-10257.

Endgahl, E. R., van der Hilst, R. & Buland, R. (1988). Global teleseismic earthquake relocation with improved travel times and procedures for depth determination, Bull. Seismol. Soc. Am., **88**, 722-743.

Endrun, B., Meier, T., Bischoff, M. & Harjes, H. P. (2004). Lithospheric structure in the area of Crete constrained by receiver functions and dispersion analysis of Rayleigh phase velocities, Geophys. J. Int., **158**, 592-608.

Ergin, K., 1966. On Epicentre Map of Turkey and Surrounding Area., T.J.K. Bült., **10**, 122.

Faber, S., Müller, G. (1980). Sp phases from the transition zone between the upper and lower mantle, Bull. Seism. Soc. Am., **70**, 487-508.

Farra, V. & Vinnik, L. (2000). Upper mantle stratification by P and S receiver functions, Geophys. J. Int., **141**, 699-712.

Faure, M. & Bonneau, M., 1988. Donnees Nouvelles sur / extension Neogene de I Egee: la Deformation Ductile du Granite Miocene de Mykonos (Cyclades, Greece)., C. R. Acad. Sci. Paris, **307**, 1553-1559.

Galanapoulos, A. G. (1967). The Seismotectonic Regime in Greece., Ann. Geofis., **20**, 109.

Gautier, P., Ballevre, M., Brun, J.-P. & Jolivet, L. (1990). Extension Ductile et Sedimentaires Mio -Pliocenes dans les Cyclades (iles de Naxos et Paros)., C. R. Acad. Sci. Paris, **310**, 147-153.

References

Gautier, P., Brun, J. P. (1994). Ductile crust exhumation and extensional detachments in the central Aegean (Cyclades and Evia islands), Geodyna. Acta, **7**, 57-85.

Gautier, P., Brun, J. P., Moriceau, R., Sokoutis, D., Martinod, J. & Jolivet, L. (1999). Timing, kinematics and cause of Aegean extension: a scenario based on a comparison with simple analogue experiments, Tectonophysics, **315**, 31-72.

Gregersen, S. & Jaeger, W. (1984). The Gravity Field of a Dipping Plate in Greece., Geophys. J. R. Astron. Soc., **76**, 439-443.

Hacker, B. R., Abers, G. A., Peacock, S. M. (2003). Subduction factory, 1. Theoretical mineralogy, densities, seismic wave speeds, and H2O contents, *J. Geophys. Res*., **108**, NO. B1, 2029, doi:10.1029/2001JB001127.

Hatzfeld, D., Karagianni, E., Kassaras, I., Kiratzi, A., Louvari, E., Lyon-Caen, H., Makropoulos, K., Papadimitriou, P., Bock, G., and Priestley, K. (2001). Shear wave anisotropy in the upper antle beneath the Aegean related to internal deformation, J. Geophys. Res., **106**, 30737-30753.

Hatzfeld, D. (1994). On the shape of the subducting slab beneath the Peleponnese, Greece, Geophys. Res. Lett., **21**, 173-176.

Hatzfeld, D., et al. (1989). The Hellenic subduction beneath the Peloponnesus: First results of a microerathquake study, Earth Planet. Sci. Lett., **93**, 283-291.

Hatzfeld, D., Besnard, M., Makropoulos, K., Voulgaris, N., Kouskouna, V., Hatzidimitriou, P., Panagiotopoulos, D., Karakaisis, G., Deschamps, & Lyon-Caen, H. (1993), Subcrustal microearthquake seismicity and fault plane solutions beneath the Hellenic arc, J. Geophys. Res., **98**, 9861-9870.

Hatzfeld, D., Kementzetzidou, D., Karakostas, V., Ziazia, M., Northard, S., Diagourtas, D., Deschamps, A., Karakaisis, G., Papadimitriou, P., Scordilis, M., Smith, R., Voulgaris, V., Kiratzi, S., Makropoulos, K., Bouin, M. P. & Bernard, P. (1996). The Galaxidi Earthquake of 18 November 1992: A Possible Asperity within the Normal Fault System of the Gulf of Corinth (Greece), Bull. Seism. Soc. Am., **86**, 6, 1987-1991.

Hatzfeld, D. & Martin, C. (1992). The Aegean intermediate seismicity defined by ISC data, Earth Planet. Sci. Lett., **113**, 267-275.

Hatzfeld, D., Martinod, J., Bastet, G. & Gautier, P. (1997). An analog experiment for the Aegean to describe the contribution of gravitational potential energy, J. Geophys. Res., **102**, 649-659.

Hatzfeld, D., Pedotti, G., Hatzidimitriou, P. & Makropoulos, K. (1990). The Strain Pattern in the Western Hellenic Arc Deduced from a Microearthquake Survey, Geophys. J. Int., **101**, 181-202.

Jackson, J. A., King, G. C. P. & Vita-Finzi, C. (1982). The Tectonics of the Aegean: an Alternative View., Earth Planet. Sci. Lett.

Jackson, J. A. & McKenzie, D. P. (1984a). Active Tectonics of the Alpine Himalayan Belt Between Western Turkey and Pakistan, Geophys. J. R. Astron. Soc., **77**, 185-246.

Jackson, J. A. & McKenzie, D. P. (1984b). Rotational Mechanism of Active Deformation in Greece and Iran, The Geological Evolution of the Eastern Mediterranean (Eds: J. E. Dixon, A. H. F. Robertson), 743-754.

References

Jackson, J., Haines, J. & Holt, W. (1994). A comparison of satellite laser ranging and seismicity data in the Aegean region, Geophys. Res. Lett., **21**, 2849-2852.

Jackson, J. A. & McKenzie, D. P. (1988). The relationship between plate motions and seismic moment tensors, and the rates of active deformation in the Mediterranean and Middle East, Geophys. J. R. Astron. Soc., **93**, 45-73.

Jolivet, L., Brun, J.-P., Gautier, P., Lallemant, S. & Patriat, M. (1994). 3D-Kinematics of Extension in the Aegean Region from the Early Miocene tothe Present, Insights from the Ductile Crust, Bull. Soc. géol. Fr., **165**, 3, 195209.

Jolivet, L. (2001). A comparison of geodetic and finite strain in the Aegean, geodynamic implications, Earth Planet. Sci. Lett. **187**, 95-104.

Jongsma, D. (1974). Heat Flow in the Aegean Sea, Geophys. J. R. Astron. Soc., **37**, 337-346.

Jongsma, D. (1975). A Marine Geophysical Study of the Hellenic Arc, PhD, Cambridge.

Jongsma, D. (1977). Bathymetry and Shallow Structure of the Pliny and Strabo Trenches, South of the Hellenic Arc, Geol. Soc. Am. Bull., **88**, 797-805.

Kahle, H. -G., Straub, C., Reilinger, R., McClusky, S., King, R., Hurst, K., Veis, G., Kastens, K., Cross, P. (1998). The strain field in the eastern Mediterranean region, estimated by repeated GPS measurments, Tectonophysics, **294**, 237-252.

Karagianni, E. E. et al. (2002). Rayleigh wave group velocity tomography in the Aegean area, Tectonophysics, **358**, 187-209.

Karagianni, E. E., Papazachos, C. B., Panagiotopoulos, D. G., Suhadolc, P., Vuan, A. & Panza, G. F. (2005). Shear velocity structure in the Aegean area obtained by inversion of Rayleigh waves, Geophys. J. Int., **160**, 127-143.

Kind, R. (1985). The reflectivity method for different source and receiver structures and comparison with GRF data, J. Geophys. **58**, 146-152, 1985.

Kind, R. and Vinnik, L. P. (1988). The upper mantle discontinuities underneath the GRF array from P-to-S converted phases, J. Geophys. **62**,138-147.

Kirtazi, A. A., Papadimitriou, E. E & Papazachos, B. C. (1987). Survey in the Steno dam site in norhwestern Greece, Ann. Geophys., **5**, 161-166.

Kissel, C. & Laj, C. (1988). The tertiary geodynamical evolution of the Aegean arc; a paleomagnetic reconstruction, Tectonophysics, **146**, 183-201.

Kosarev, G., Kind, R., Sobolev, S. V., Yuan, X., Hanka, W., Oreshin, S. (1999). Seismic evidence for a detached Indian lithosphere mantle beneath Tibet, Science, **283**, 1306-1309.

Knapmeyer, M. & Harjes, H. -P. (2000). Imaging crustal discontinuities and the downgoing slab beneath western Crete, Geophys. J. Int., **143**, 1-21.

Kumar, P., Kind, R., Hanka, W., Wylegalla, K., Reigber, Ch., Yuan, X., Wölbern, I., Schwintzer, P., Fleming, K., Dahl-Jensen, T., Larsen, T., Schweitzer, J., Priestley, K., Gudmundsson, O., Wolf, D. (2005). The Lithosphere-Asthenosphere Boundary in the North West Atlantic Region. EPSL, submitted.

References

Kumar, P., Yuan, X., Kind, R. and Kosarev, G. (2005). The lithosphere-asthenosphere boundary in the Tien Shan-Karakoram region from S receiver functions - evidence of continental subduction, Geophys. Res. Lett., 32, L07305, doi:10.1029.

Lagios, E., Hipkin, R. G., Angelopoulos, A. & Nikolaou, S. (1988). The gravity anomaly map of Greece: A recompilation, Inst. of Geol. and Miner. Explor. of Greece, Athens.

Langston, C. A. (1979). Structure under the Mount Rainier, Washington, inferred from telesismic body waves, J. Geophys. Res., **84**, 4749-4762.

Langston, C. A. (1977). The effect of planar dipping structure on source and receiver responses for constant ray parameter. Bull. Seism. Soc. Am., **67**, 1029-1050.

Le Pichon, X. & Angelier, J. (1979). The Hellenic arc and trench system: a key to the neotectonic evolution of the eastern Mediterranean area, Tectonophysics, **60**, 1-42.

Le Pichon, X. & Angelier, J. (1981). The Aegean Sea, Phil. Trans. Roy. Soc. Lond., A**300**, 357 -372.

Le Pichon, X., Chamot-Rooke, N. & Lallemant, S. (1995). Geodetic determination of the kinematics of central Greece with respect to Europe: implications for eastern Mediterranean tectonics, J. Geophys. Res., **100**, 12675-12690.

Le Pichon, X., Lybéris, N. & Alvarez, F. (1984). Subsidence History of the North Aegean Trough, The Geological Evolution of the Eastern Mediterranean (Eds: J. E. Dixon, A. H. F. Robertson), 727-741.

Le Pichon, X., Lyberis, N., Angelier, J. & Renard, V. (1982). Strain distribution over the east Mediterranean ridge: a synthesis incorporating new Sea-Beam data, Tectonophysics, **86**, 243-274.

Levin, V. & Park, J. (1997). P-SH conversions in a flat-layered medium with anisotropy of arbitrary orientation, Geophys J. Int, **131**, 253-266.

Li, X., Bock, G., Vafidis, A., Kind, R., Harjes, H. -P., Hanka, W., Wylegalla, K., v. d. Meijde, M., and Yuan, X. (2003). Receiver function study of the Hellenic subduction zone: Imaging crustal thickness variations and the oceanic Moho of the descending African lithosphere, Geophys. J. Int., **155**, 733-748.

Li, X., Kind, R., Yuan, X., Wölbern, I. and Hanka, W. (2004). Rejuvenation of the Lithosphere by the Hawaiian plume. Nature, **427**, 827 – 829.

Ligdas, C. N. & Lees, J. M. (1993). Seismic velocity constrains in the Thessaloniki and Chalkidiki areas (northern Greece) from a 3-D tomographic study, Tectonophysics, **228**, 97-121.

Ligdas, C. N. & Main, I. G. (1991). On the resolving power of tomographic images in the Aegean area, Geophys. J. Int., **107**, 197-203.

Ligdas, C. N, Main, I. G. & Adams, R. D. (1990). 3-D structure of the lithosphere in the Aegean sea region, Geophys. J. Int., **102**, 219-229.

Lort, J. M. (1971). The Tectonics of the eastern Mediterranean: A Geophysical Review, Reviews of Geophysics and Space Physics, 9, 2.

References

Makris, J. (1973). Some geophysical aspects of the evolution of the Hellenides, Bull. geol. Soc. Greece, **10**, 206-213.

Makris, J. (1975). Crustal Structure of the Aegean Sea and the Hellenides Obtained from Geophysical Survey., J. Geophys., **41**, 441-443.

Makris, J. (1976). A dynamic model of the Hellenic arc deduced from geophysical data, Tectonophysics, **36**, 339-346.

Makris, J. (1977). Geophysical Investigations of the Hellenides, Hamburger Geophysikalische Einzelschriften (Ed: Söhne, G. M. L. W.).

Makris, J. (1978a). Some Geophysical Considerations on the Geodynamic Situation in Greece, Tectonophysics, **46**, 251-268.

Makris, J. (1978b). The Crust and Upper Mantle of the Aegean region From Deep Seismic Soundings, Tectonophysics, **46**, 269-284.

Makris, J. (1985). Geophysics and Geodynamic Implications for the Evolution of the Hellenides, Geological Evolution of the Mediterranean Basin (Eds: D. J. Stanley, F. C. Wezel), 231-248.

Makris, J., Nicolich, R. & Weigel, W. (1986). A Seismic Study of the Western Ionian Sea., Ann. Geoph., **6**, 665678.

Makris, J. & Stobbe, C. (1984). Physical properties and state of the crust and upper mantle of the eastern Mediterranean Sea deduced from geophysical data. Marine Geol., **55**, 347-363.

Makris, J. & Vees, R. (1977). Crustal structure of the Aegean Sea and the island Evia and Crete, Greece, obtained by refractional seismic experiments, J. Geophys., **42**, 329-341.

Makropoulos, k. & Burton, P. (1984). Greek tectonics and seismicity, Tectonophysics, **106**, 275-304.

Maley, T. S. & Johnson, G. L. (1971). Morphology and Structure of the Aegean Sea, Deep-Sea Res., **18**, 109-122.

Marone, F., van der Meijde, M., van der Lee, S. & Giardini, D. (2003). Joint inversion of local, regional and teleseismic data for crustal thickness in the Eurasia-Africa boundary region, Geophys. J. Int., **154**, 499-514.

Martin, C. (1988). Geometric et Cinematique de la Subduction Egeene Structure en Vitesse et en Attenuation Sous le Peleponnese., Ph.D, Univ. Joseph Fourier, Grenoble, 261p.

Mascle, J. & Martin, L. (1990). Shallow structure and recent evolution of the Aegean Sea: A synthesis based on continuous reflection profiles, Marine Geology, **94**, 271-299.

McClusky, S., et al. (2000). GPS constraints on plate motions and deformations in the Eastern Mediterranean: Implications for plate dynamics, J. Geophys. Res., **105**, 5695-5719.

McKenzie, D. P. (1970). The plate tectonics of the Mediterranean region, Nature, **226**, 239-243.

References

McKenzie, D. P. (1972). Active tectonics of the Mediterranean region, Geophys. J. R. astr. Soc., **30**, 109-185.

McKenzie, D. P. (1978). Active tectonics of the Alpine-Himalayan belt: the Aegean Sea and surrounding regions, Geophys. J. R. astr. Soc., **55**, 217-254.

Meijer, P. T. & Wortel, M. J. R. (1997). Present-day dynamics of the Aegean region: A model analysis of the horizontal pattern of stress and deformation, Tectonics, **16**, 879-895.

Melis, N. S., Brooks, M. & Pearce, R. (1989). A Microearthquake Study in the Gulf of Pataras Region, Westeern Greece, and its Seismotectonic Interpretation., Geophys. J. Int., **98**, 595-524.

Mercier, J. (1981). Extensional-compressional tectonics associated with the Aegean Arc: comparison with the Andean Cordillera of south Peru-north Bolivia, Phil. Trans. R. Soc. Lond., A**300**, 337-355.

Mercier, J. L., Carey, E., Philip, H. & Sorel, D. (1976). La Neotectonique Plio-Quaternaire de I Arc Egeen Externe et la mer Egee et ses Relations Avec la Seismicite., Bulletin de la Societe Geologique de France, **7**, XVIII, 355-372.

Mercier, J. L., Carey, E., Philip, H. & Sorel, D. (1977). La Neotectonique Plio-Quaternaire de I arc Egeen Externe et de la mer Egee et ses Relations Avec la Sismicite, Bull. Soc. géol. Fr., **18**, 159-176.

Mercier, J., Sorel, D., Vergely, P. & Simeakis, K. (1989). Extensional tectonic regimes in the Aegean basins during the Cenozoic, Basin research, **2**, 49-71.

Mueller, S. & Kahle, H.-G. (1993). Crust-Mantle Evolution, Structure and Dynamics of the Mediterranean-Alpine Region, Geodynamic Series, **23**, 249-298.

Mueller, S., Kahle, H.-G. & Barka, A. A. (1997). Plate Tectonic Situation in the Anatolian-Aegean Region, ATNAMPP, 13-28.

Myrianthis, M. L. (1984). Graben Formation and Associated Seismicity in the Gulf of Korinth (Central Greece), Geological Evolution of the Eastern Mediterranean (Ed:), 701-707.

Oral, M. B., Reilinger, R. E., Toksöz, M. N., King, R. W., Barka, A. A. & Kinik, I. (1995). Coherent Plate Motions in the Eastern Mediterranean Continental Collision Zone, Eos, Trans. AGU, **76**, 2, 9-11.

Owens, T. J., Zandt, G. & Taylor, S. R. (1984). Seismic evidence for an ancient rift beneath the Cumberland Plateau, Tennessee: A detailed analysis of braodband teleseismic P waveforms. J. Geophys. Res., **89**, 7783-7795.

Panagiotopoulos, D. G. & Papazachos, B. C. (1985). Travel times of Pn waves in the Aegean and sorrounding area, Geophy. J. R. astr. Soc., **80**, 165-176.

Papazachos, B. C. (1969). Phase velocities of Rayleigh waves in the southeastern Europe and eastern Mediterranean Sea, Pure Appl. Geophys., **75**, 47-55.

Papazachos, B. C. (1973). Distrubution of Seismic Foci in the Mediterranean and Suirrounding Area and its Tectonic Implication, Geophys. J. R. Astron. Soc., **33**, 421-430.

References

Papazachos, B. C. (1990). Seismicity of the Aegean and surrounding area, Tectonophysics, **178**, 287-308.

Papazachos, B. C. & Comninakis, P. E. (1969). Geophysical features of the Greek Island arc and eastern Mediterranean ridge, C. R. Seances Conf. Reunie Madrid, **16**, 74-75.

Papazachos, B. C. & Comninakis, P. E. (1971). Geophysical and tectonic features of the Aegean arc, J. Geophys. Res., **76**, 8517-8533.

Papazachos, B. C., Karakostas, V. G., Papazachos, C. B. & Scordilis, E. M. (2000). The geometry of the Wadati-Benioff zone and lithospheric kinematics in the Hellenic arc, Tectonophysics, **319**, 275-300.

Papazachos, C. B. (1994). Structure of the Crust and Upper Mantle in SE Europe by Inversion of Seismic and Gravimetric Data (in Greek)., Ph.D, Thesis, Univ. of Thessaloniki, Thessaloniki, Greece, 208pp.

Papazachos, C. B. (1998). Crustal and upper mantle P and S velocity structure of the Serbomacedonian massif (Northern Greece), Geophys. J. Lett., **134**, 25-39.

Papazachos, C. B. (1999). Seismological and GPS evidence for the Aegean Anatolia interaction, Geophys. Res. Lett., **17**, 2653-2656.

Papazachos, C. B., Hatzidimitriou, P. M., Panagiotopoulos, D. G. & Tsokas, G. N. (1995). Tomography of the crust and upper mantle in southeast Europe, J. Geophys. Res., **100**, 12405-12422.

Papazachos, C. & Kirtazi, A. (1996). A detailed study of the active crustal deformation in the Aegean and surrounding area, Tectonophysics, **253**, 129-153.

Papazachos, C. B. and Nolet, G. (1997). P and S deep velocity structure of the Hellenic area obtained by robust nonlinear inversion of travel times, J. Geophys. Res., **102**, 8349-8367.

Papazachos, C. B. & Scordilis, E. M. (1998). Crustal structure of the Rhodope and surrounding area obtained by non-linear inversion of P and S travel times and its tectonic implications, Acta Vulcanologica, **10**(2), 339-345.

Payo, G. (1967). Crustal structure of the Mediterranean Sea by surface waves, I, Group velocity, Bull. Seismol. Soc. Am., **57**,151-172.

Payo, G. (1969). Crustal structure of the Mediterranean Sea by surface waves, II, Phase velocity and travel time, Bull. Seismol. Soc. Am., **59**, 23-42.

Reilinger, R., McClusky, S. C., Oral, M. B., King, R. W. & Toksoz, M. N. (1997). Global Positioning System measurements of present-day crustal movements in the Arabia-Africa-Eurasia plate collision zone, J. Geophys. Res., **102**, 9983-9999.

Rigo, A., Lyon-Caen, H., Armijo, R., Deschamps, A., Hatzfeld, D., Makropoulos, K., Papadimitriou, E. & Kassaras, I. (1995). A Microseismic Study in the Western Part of the Gulf of Corinth (Greece): Implications for Large Scale Normal faulting Mechanisms., Geophys. J. Int., **126**, 663-688.

Roberts, S. C. & Jackson, J. A. (1991). Active Normal Faulting in Central Greece: An Overview., The Geometry of Normal Faults (Eds: A. M. Roberts, G. Yielding and B. Freeman) Spec Publ. Geol. Soc. Lond, Blackwell Scientific Publications, Oxford, **56**, 125-142.

References

Ryan, W. B. F. & Hsu, K. et al. (1973). Mediterranean Ridge, Levantine Sea - Site 130., Initial Reports of the Deep Sea Drilling Project (Eds: W. B. F. Ryan et al.), **3**, 355-382.

Ryan, W. B. F., Stanley, D. J., Hersey, J. B., Fahlquist, D. A. & Allan, T. D. (1969). The Tectonics and Geology of the Mediterranean Sea, The Sea (Ed: A. E. Maxwell), 387-492.

Sengör, A. M. C., Görür, N. & Saroglu, F. (1985). Strike-Slip faulting and related Basin Formation in Zones of Tectonic Escape: Turkey as a Case Study, Soc. Econ. Paleont. Min. Spec. Pub., **37**, 227-264.

Sengör, A. M. C. (1987). Cross-Faults and Differential Stretching of hanging Walls in Regions of Low-Angle Normal Faulting: Examples from Western Turkey, Tectonics, **28**,575-589.

Saunders, P., Priestley, K. & Taymaz, T. (1998), Variations in the crustal structure beneath western Turkey, Geophys. J. Int., **134**, 373-389.

Shanov, S., Spassov, E. & Georgiev, T. (1992). Evidence for the existence of a paleosubduction zone beneath the Rhodopean massif (Central Balkans), Tectonophysics, **206**, 307-314.

Simsek, S. (1997). Geothermal Potential in Northwestern Turkey, Active Tectonics of Northwestern Anatolia-The Marmara Poly-Project (Ed: C.Schindler, M. Pfister), 111-123.

Sorel, D., Mercier, J. L., Keraudren, B. & Cushing, M. (1988). Le r´´ le de la traction de la lithosphere subducte dans l' volution geodynamique plio-plistocne de l' arc gen: mouvement verticaux alterns et vaiations du rgime tectonique, C. R. Acad. Sci. Paris, **307**, 1981-1986.

Sonder, L. & England, P. (1989), Effects of a Temperature-Dependant Rheology on Large-Scale Continental Extension, J. Geophys. Res., **94**, 7603-7619.

Spakman, W. (1985). A Tomographic Image of the Upper Mantle in the Eurasian - African - Arabian Collision Zone., Eos, Trans.

Spakman, W. (1986). Subduction beneath Eurasia in connection with the Mesozoic Tethys, Geol. Mijnbouw., **65**, 145-153.

Spakman, W., Van der Lee, S. & Van der Hilst, R. D. (1993). Travel time tomography of the European-Mediterranean mantle down to 1400 km, Phys. Earth. Planet. Inter., **79**, 3-74.

Spakman, W., Wortel, M. J. R. & Vlaar, N. S. (1988). The Hellenic subduction zone: a tomographic image and its geodynamical implications, Geophys. Res. Lett., **15**, 60-63.

Taymaz, T., Jackson, J. A. & Mckenzie, D. (1991). Active Tectonics of the North and Central Aegean Sea, Geophys. J. Int., **106**, 433-490.

Tiberi, C., et al. (2000). Crustal and upper mantle structure beneath the Cornith rift (Greece) from a teleseismic tomography study, J. geophys. Res., **105**, 28159-28172.

Tiberi, C., Diament, M., Lyon-Caen, H. & King, T. (2001). Moho topography beneath the corinth Rift area (Greece) from inversion of gravity data, Geophys. J. Int., **145**, 797-808.

References

Tirel, C., Gueydan, F., Tiberi, C., Brun, J. -P. (2004). Aegean crustal thickness inferred from gravity inversion Geodynamical implications, Earth Planet. Sci. Let., **228**, 267-280.

Tsokas, G. N. and Hansen, R. O. (1997). Study of the crustal thickness and subducting lithosphere in Greece from Gravity data, J. geophys. Res., **102**, 20585-20597.

van der Meijde, M., van der Lee, S. & Giardini, D. (2003). Crustal structure beneath broad-band seismic stations in the Mediterranean region, Geophys. J. Int., **152**, 729-739.

Vigner, A. (2002). Images sismiques par reflexions verticale et grand-angle de la croute en contexte extensif, Les Cyclades et le Fosse Nord-Egeen, These de l' Institut Physique du Globe de paris, pp. 269.

Vogt, P. R. & Higgs, R. H. (1969). An Aeromagnetic Survey of the Eastern Mediterranean Sea and Its Interpretation, Earth Planet. Sci. L, **5**, 439-448

Wdowinski, S., O' Connell, R. J. & England, Ph. (1989). A continuum Model of Continental Deformation Above Subduction Zones: Application to the Andes and the Aegean, J. Geophys. Res., **94**, 10331-10346.

Westaway, R. (1994b). Evidence for dynamic coupling of surface processes with isostatic compensation in the lower crust during active extension of western Turkey, J. Geophys. Res., **99**, 20,203-20.,204.

Woodside, J. M. & Bowin, C. (1970). Gravity Anomalies and Inferred Crustal Structure in the Eastern Mediterranean Sea., Geol. Soc. Am. Bull., **81**, 1107-1122.

Wortel, M. J. R., Goes, S. D. B. & Spakman, W. (1990). Structure and seismicity of the Aegean subduction zone, Terra Nova, **2**, 554-562.

Yuan, X. and 21 authors. (2000). New constraints on subduction and collision processes in the Central Andes from P-to-S converted seismic phases, Nature, **408**, 958-961.

Yuan, X., Sobolev, S. V. & Kind, R. (2002). Moho topography in the central Andes and its geodynamic implication, Earth Planet. Sci. Let., **199**, 389-402.

Zandt, G. & Ammon, C. J. (1995). Continental crust composition constrained by measurements of crustal Poisson's ratio, Nature, **374**, 152-154.

Zhu, H. & Kanamori, H. (200Li, X., Kind, R., Yuan, X., Wölbern, I. and Hanka, W., 2004. Rejuvenation of the Lithosphere by the Hawaiian plume. *Nature No. 427, 827 – 829*.0). Moho depth variation in southern Clifornia from teleseismic receiver functions, J. Geophys. Res. **105**, 2969-2980.

References

Appendix A

Stations list & Instrumentation

Statios	*Lon*	*Lat*	*Network*	*Sensor*
AGGI	22.32	39.01	SFG	CMG3
ALEX	25.79	40.97	SFG, NOA	CMG3, LE20S
ANAT	22.68	39.74	SFG	LE5S
APEZ	24.88	34.97	GEOFON	STS-2
ATH	23.72	37.97	NOA	LE20S
DRAM	24.01	41.2	SFG	LE5S
EVR	21.81	38.92	NOA	LE20S
FODE	24.95	35.37	GEOFON	STS-2
FLOR	21.38	40.78	SFG	CMG3
GVD	24.08	34.83	GEOFON	STS-2
HIOS	26.04	38.25	SFG	CMG40
IDI	24.89	35.28	MEDNET	STS-2
ITM	21.93	37.18	NOA	LE20S
JAN	20.85	39.66	NOA	LE20S
KARP	27.17	35.55	SFG,NOA	CMG40, CMG40
KEK	19.8	39.71	NOA	LE20S
KOS1	27.21	36.84	SFG	CMG40
KOZA	21.78	40.3	SFG, NOA	LE5S, LE20S
KRIS	25.5	35.17	GEOFON	STS-2
LESB	26.26	39.24	SFG, NOA	CMG3, LE20S
LIMN	25.16	39.95	SFG, NOA	CMG3, CMG40

Appendix A. Stations list & Instrumentation

Statios	*Lon*	*Lat*	*Network*	*Sensor*
LITO	22.48	40.1	SFG	CMG40
LKR	23	38.65	NOA	CMG40
MILO	24.44	36.67	SFG	CMG40
NAXO	25.52	37.07	SFG, GEOFON	CMG40, STS-2
NEO	23.22	39.31	NOA	LE20S
NPS	25.61	35.26	NOA	LE20S
NVR	23.86	41.35	NOA	CMG40
PENT	23.96	38.04	SFG	CMG3
PLG	23.45	40.37	NOA	LE20S
RLS	21.47	38.06	NOA	LE20S
RODO	28.02	36.08	SFG, NOA	CMG3, LE20S
SAMO	26.83	37.7	SFG, NOA	CMG3, LE20S
SANT	25.45	36.37	GEOFON	STS-2
SKD	23.92	35.41	GEOFON	STS-2
SKIR	24.57	38.85	SFG	CMG40
SKOP	23.74	39.11	SFG	CMG40
THES	22.96	40.63	SFG	CMG3
VAM	24.2	35.41	NOA	LE20S
VELI	22.94	36.71	SFG, NOA	CMG3, LE20S
VLS	20.59	38.18	NOA	LE20S
ZKR	26.31	35.11	GEOFON	STS-2
AMOE	25.97	36.91	CYC	Mark_L4_3D
AMOW	25.8	36.78	CYC	Mark_L4_3D
ANAF	25.77	36.35	CYC	Mark_L4_3D
ANID	25.68	36.62	CYC	Mark_L4_3D
ASTY	26.41	36.58	CYC	STS-2
FOLE	24.92	36.62	CYC	Mark_L4_3D
IOSI	25.36	36.73	CYC	Mark_L4_3D
KIMO	24.56	36.79	CYC	Mark_L4_3D
MILE	24.49	36.73	CYC	Mark_L4_3D

Statios	*Lon*	*Lat*	*Network*	*Sensor*
MILN	24.42	36.75	CYC	Mark_L4_3D
MILO	24.4	36.69	CYC	STS-2
MILS	24.5	36.69	CYC	Mark_L4_3D
MYKO	25.38	37.48	CYC	Mark_L4_3D
NEAK	25.4	36.4	CYC	Mark_L4_3D
PARO	25.18	37.11	CYC	Mark_L4_3D
SANC	25.45	36.42	CYC	Mark_L4_3D
SANN	25.39	36.46	CYC	Mark_L4_3D
SANS	25.39	36.35	CYC	Mark_L4_3D
SCHI	25.51	36.87	CYC	Mark_L4_3D
SERI	24.48	37.16	CYC	Mark_L4_3D
SIFN	24.73	36.95	CYC	Mark_L4_3D
THIR	25.34	36.43	CYC	Mark_L4_3D

Table A.1. List of utilized stations and instrumentation.

Appendix A. Stations list & Instrumentation

Appendix B

List of events

Date	Lat	Long	Depth	mb
9609052342	21.9264	121.5127	24.5	5.9
9609200003	9.5913	126.3468	51.1	5.9
9609200410	9.4749	126.3234	39.5	6.3
9610011550	12.3771	58.0723	10	6
9610020948	11.7729	125.5176	46.8	6
9706270439	38.2482	-26.7073	10	6.1
9707091924	10.5045	-63.5453	3	6.9
9711081002	35.1163	87.3741	10	6.2
9801020103	-2.7846	101.9943	102.4	6.3
9801020742	-5.154	102.5056	33	6
9801030610	-35.5487	-16.0444	10	5.9
9802162353	52.6815	-33.6622	10	6.1
9802201218	36.5084	71.1185	230.7	6.3
9803211633	80.1089	2.5307	10	6.7
9803211822	36.4396	70.1202	10	6.5
9803290715	-0.0504	-17.9662	10	6.1
9804011756	-0.502	99.3222	61.6	7
9805032330	22.3022	125.3178	10	6.6
9805210534	0.1811	119.5659	20.4	6.3
9805231744	8.1778	123.7885	646	6.8
9805292249	41.1312	75.6611	17.5	5.8
9805300622	37.1533	70.1183	30.4	6.2
9807172203	-4.7137	103.0174	58.9	6.2
9807241844	21.4381	121.9653	6.7	5.9
9808020440	39.5712	77.0284	9.8	5.8
9808100952	7.4056	94.2391	33	5.9
9808230536	14.7225	120.0509	73	6.7
9808270903	39.5762	77.3403	33	6.4
9809202121	-7.6785	107.0171	65.7	6
9809281334	-8.1741	112.4447	157.2	6.8
9811191539	22.6733	125.7718	23	5.8
9901240800	-26.463	74.476	10	6
9902030635	-6.19	104.222	33	5.8
9902041928	4.033	95.283	55.5	5.8

9902251858	51.604	104.864	10	5.9
9903040852	5.397	121.937	33	6.4
9903281905	30.512	79.403	15	6.4
9905181952	5.625	123.855	33	5.8
9906292318	36.622	71.353	189.3	5.9
9907211346	4.567	97.211	175	5.9
9908140016	-5.885	104.711	101.4	6
9909220014	23.729	121.167	26	6.2
9909252352	23.738	121.158	17	6.2
9910220218	23.445	120.506	33	5.9
9911011753	23.378	121.52	33	6.1
9911081645	36.522	71.24	228.4	6.2
9911111805	1.276	100.322	211	6
9911150542	-1.339	88.976	10	6.3
9911290346	-1.275	89.043	10	5.9
9912111803	15.766	119.74	33	6.5
0004180012	-52.455	13.544	10	6.2
0005122310	35.975	70.657	107.7	6
0005211958	71.19	-8.263	10	6.8
0006041628	-4.721	102.087	33	5.8
0006050300	-5.605	102.886	33	5.8
0006050634	-4.909	102.656	33	5.8
0006060958	-5.093	102.699	33	6.3
0006072146	26.856	97.238	33	6.1
0006072345	-4.612	101.905	33	5.8
0006090800	-5.549	102.679	33	6.2
0006101823	23.843	121.225	33	6.6
0006171540	63.966	-20.487	10	6.8
0006181444	-13.802	97.453	10	6.1
0006210051	63.98	-20.758	10	6.1
0007080452	-5.408	102.7	33	5.8
0007101039	-4.473	103.758	104.7	6.1
0007160321	20.253	122.043	33	6
0007172253	36.283	70.924	141.4	5.8
0007222056	-4.07	102.37	69.1	5.9
0007250314	-53.553	-3.169	10	5.9
0008241136	-6.026	102.687	33	6
0009011156	1.438	96.591	33	5.8
0009080134	-39.841	41.762	10	5.8
0009100854	24.008	121.526	34.8	6.3
0009120027	35.389	99.343	10	6.1
0009121627	-5.435	101.823	33	5.8
0009221822	-4.964	102.104	33	5.9
0009250400	-46.806	37.59	10	6.1
0010020225	-7.977	30.709	34	6.2
0010041437	11.124	-62.559	110.3	6.1
0010051339	31.732	-40.958	10	6.3
0010250932	-6.549	105.63	38	5.8
0011050445	-6.076	102.68	33	6.3
0101150552	-40.344	78.362	10	6.5
0101161325	-4.022	101.776	28	6.9
0101260316	23.419	70.232	16	5.9

0101280102	23.507	70.517	10	5.8
0102080541	24.269	125.112	15.7	6.2
0102131928	-4.68	102.562	36	6
0102181304	-47.456	32.386	10	5.8
0102250221	36.424	70.881	202.5	5.8
0103051550	34.369	86.902	33	6
0103071810	-6.81	-12.911	10	5.8
0103122335	-7.206	106.116	33	5.9
0103150122	8.656	94.013	33	5.8
0105180205	0.414	97.784	33	5.8
0105250506	-7.869	110.179	143.1	5.9
0106140235	24.513	122.033	32.1	6
0106151619	13.903	51.679	10	5.9
0108050516	12.224	93.352	96.4	5.9
0108172225	25.748	126.19	33	5.8
0109020225	0.889	82.501	10	6.2
0109070245	-13.166	97.297	10	5.8
0110140110	-8.598	110.633	67.2	6
0110171129	19.354	-64.932	33	6.1
0111140926	35.946	90.541	10	6
0111150103	-1.587	-15.578	10	5.9
0111182159	35.726	93.691	10	5.9
0111232043	36.392	71.506	106.5	5.8
0201030705	36.088	70.687	129.3	5.8
0201150712	-6.314	105.205	10	5.8
0202120327	23.716	121.56	54.8	6.3
0203031208	36.429	70.438	209	6.3
0203052116	6.033	124.249	31	6
0203081827	5.871	124.274	23.3	6
0203171933	-45.221	35.105	10	5.9
0203251456	36.062	69.315	8	5.8
0203260345	23.346	124.09	33	5.9
0203270852	36.023	69.338	10	6.4
0203310652	24.279	122.179	32.8	5.8
0204120400	35.959	69.417	10	5.8
0205131957	19.132	121.238	33	6.1
0205141656	-36.518	78.932	10	6.2
0205150346	24.636	121.922	10	5.8
0205281645	24.069	122.264	33	5.9
0206160000	0.495	119.901	34.8	5.8
0206161831	-2.338	102.559	231.6	6
0206270550	-6.963	104.181	11	5.8
0207110736	24.075	122.288	43.8	5.8
0207132006	30.797	69.979	33	6
0208041516	-35.457	-16.238	10	5.9
0208130605	-6.998	104.016	33	5.8
0208130837	14.749	55.85	10	5.8
0208261455	-6.75	105.705	62.9	5.8
0209011714	14.284	51.945	10	5.9
0209031423	13.536	120.754	10	6.2
0209132228	13.036	93.068	21	5.8
0209141958	13.055	93.157	33	5.8

0209161848	66.938	-18.456	10	6
0210031905	-7.526	115.663	315.8	6.1
0210122343	15.096	118.504	33	5.9
0210240608	-1.884	29.004	11	6.2
0210242153	6.03	94.419	64.6	6.2
0211020126	2.824	96.085	30	5.8
0211020447	12.701	92.856	33	5.9
0211020946	2.954	96.394	27	6.5
0211202132	35.414	74.515	33	5.9
0212300449	7.471	123.407	10	6
0301062343	15.651	119.658	10	6.3
0301271756	-46.048	35.057	10	5.8
0302150547	12.171	123.921	10	5.8
0302151101	12.168	124.079	10	5.8
0302240203	39.61	77.23	11	5.8
0303260422	12.52	92.635	33	5.9
0303291146	35.966	70.606	115	5.8

Table **B**.1. List of events recorded by GEOFON stations for P receiver function analysis.

Date	Lat	Long	Depth	mb
0303021642	-36.958	-20.879	10	5.6
0303022246	37.68	141.719	42.6	5.7
0303120447	39.362	77.426	10	5.7
0303151941	52.249	160.387	30.2	5.6
0303171636	51.272	177.978	33	5.9
0303171837	52.326	160.306	33	5.5
0303191443	52.207	160.716	33	5.6
0303260422	12.518	92.564	33	5.8
0303291146	35.976	70.585	114.1	5.9
0304020343	35.28	-35.729	10	5.5
0304071828	36.296	141.679	33	5.5
0304161759	40.983	142.208	57	5.7
0304170048	37.529	96.476	14	6.2
0304171450	-54.624	1.432	10	5.5
0304241056	48.764	154.991	43.8	5.6
0304291044	-7.02	103.683	10	5.6
0304291353	43.706	147.805	62.5	6
0305041544	39.43	77.219	10	5.6
0305070258	48.532	89.572	33	5.6
0305092026	-48.209	32.272	10	5.5
0305120303	1.142	98.911	77.6	5.6
0305140603	18.266	-58.633	41.5	6.5
0305221811	42.946	72.764	33	5.5
0305240146	14.428	53.813	10	5.6
0305260924	38.849	141.568	68	6.7
0305262313	6.761	123.707	565.8	6.2
0305281615	-17.646	66.116	10	5.5
0305290559	50.878	157.301	49.4	5.5

0306011750	28.197	142.773	10	5.5
0306090152	24.413	122.02	48.1	5.5
0306100840	23.52	121.628	44.5	5.8
0306121843	13.17	120.514	46.4	5.6
0306151924	51.552	176.923	20	6
0306162208	55.492	159.999	174.8	6.3
0306191259	71.122	-7.577	10	5.6
0306231212	51.439	176.783	20	6.3
0306240652	27.362	60.974	61.3	5.6
0306250138	28.82	-43.612	10	5.5
0306261411	12.253	123.85	10	5.7
0306300007	17.457	-61.14	33	5.7
0307010552	4.529	122.511	635.4	5.8
0307011700	12.803	124.898	33	5.6
0307012229	-37.064	78.177	10	5.7
0307022352	42.323	144.842	23.9	5.8
0307040716	76.372	23.282	10	5.7
0307070655	34.606	89.475	17.7	5.7
0307071955	20.372	122.001	10	5.6
0307091715	29.736	129.968	67.4	5.5
0307111353	9.337	122.044	33	5.6
0307122301	54.65	-134.47	20	5.7
0307142000	-0.537	100.822	144.2	5.7
0307152027	-2.598	68.382	10	6.1
0307160229	-2.569	68.329	10	5.6
0307192120	-8.682	111.227	56.2	5.9
0307211516	25.975	101.29	10	6
0307211921	6.678	93.601	10	5.5
0307231638	-15.592	-13.351	10	5.8
0307251513	38.432	141.003	10	5.6
0307252213	38.415	140.996	6	6
0307262318	22.854	92.306	10	5.5
0307270625	47.151	139.248	470.3	6.3
0307280328	-1.194	67.58	10	5.7
0308112122	12.119	93.558	100	5.6
0308161058	43.796	119.618	24	5.6
0308180903	29.553	95.584	33	5.7
0308210402	29.091	59.814	20	5.8
0308312308	43.414	132.234	481	5.6
0309011513	12.076	122.4	21	5.5
0309012316	38.57	75.265	33	5.5
0309050123	5.361	95.914	134	5.7
0309071116	-5.644	102.121	33	5.6
0309080626	-8.405	110.332	45	5.5
0309141845	18.6	121.03	33	5.5
0309161124	56.05	111.34	10	5.6
0309211816	19.94	95.72	10	6.7
0309212315	-1.16	-13.96	10	6
0309220445	19.67	-70.67	10	6.5
0309251950	41.83	143.83	33	8.3
0309252010	41.9	143.64	33	5.5
0309252057	41.77	143.56	33	5.7

0309260626	42.21	144.64	10	5.6
0309262038	42.05	144.47	33	5.6
0309271133	50.06	87.73	17.6	7.5
0309271316	50.08	87.9	10	5.7
0309271852	50.08	87.79	14.8	6.3
0309272212	28.95	128.26	10	5.7
0309280417	42.7	144.65	33	5.5
0309290236	42.45	144.41	25	6.5
309290749	42.38	144.05	33	5.6
0310010103	50.19	87.67	10	6.7
0310080906	42.62	144.46	33	6.6
0310082315	42.31	144.56	33	5.7
0310090652	41.54	143.4	33	5.5
0310092219	13.81	120.04	33	6.1
0310110008	42	144.27	33	5.7
0310110111	44.08	148.07	62.6	6
0310161228	25.89	101.34	33	5.6
0310171719	-4.99	102.44	33	5.7
0310231054	51.4	176.687	33	5.6
0310251241	38.4	100.951	10	5.8
0310310106	37.812	142.619	10	6.1
0311011310	37.742	143.083	10	5.9
0311021335	44.579	150.329	33	5.5
0311070359	50.976	157.223	66	5.5
0311091952	-0.674	-19.689	10	5.5
0311120826	33.171	137.072	384.9	6.1
0311141843	36.396	141.072	41.1	5.7
0311170643	51.146	178.65	33	6.2
0311180750	51.045	178.888	33	5.8
0311181714	12.025	125.416	35	6.1
0311201224	-10.024	111.028	10	5.6
0311201405	13.037	93.245	33	5.5
0311210409	45.219	-28.035	10	5.5
0311270607	53.684	-163.247	33	5.5
0312052126	55.5	165.763	10	6.5
0312082012	51.154	178.225	33	5.7
0312091244	51.482	-179.282	33	5.9
0312100438	23.055	121.33	10	6.7
0312100846	22.893	121.366	33	5.5
0312101551	17.688	120.819	33	5.7
0312190011	19.842	95.717	10	5.8
0312210740	-0.748	-20.56	10	5.8
0312230558	-0.688	-20.34	10	5.6
0312231402	40.059	-29.669	10	5.5
0312241133	-5.723	102.2	33	5.5
0312290130	42.468	144.54	33	5.8
0312300950	47.165	154.068	33	5.6

Table **B**.2. List of events recorded by NOA stations for P receiver function analysis.

Date	Lat	Long	Depth	mb
9702070841	-19.8737	-173.2283	10	5.9
9702080155	-8.5435	158.9859	96.7	5.7
9702091232	-14.4479	-76.2662	10.4	5.7
9702091857	55.2405	161.8493	17.4	5.5
9702212340	43.7041	149.0877	10	5.8
9702251945	-21.1748	169.5427	44	5.5
9702272108	29.9614	68.2024	33.6	6.5
9702272130	30.0377	67.9747	43.4	6.4
9702281132	43.9579	147.8928	.7	5.6
9703111919	-21.818	-179.4265	614.1	5.8
9703111921	8.1376	126.344	83.5	5.7
9703111922	7.7587	127.6742	8.5	7.1
9703170805	-6.66	105.4835	50.9	5.7
9703200850	30.1313	68.0227	32.7	5.7
9703260208	51.2772	179.5267	36	5.6
9703260831	31.9526	130.3705	6.5	5.5
9703261818	2.7802	128.2069	134.2	6.2
9704011842	-18.2172	-69.2485	55.6	6.0
9704020614	11.4664	-61.1936	73.4	5.8
9704051223	-6.535	147.4619	67.1	5.9
9704060436	39.5409	77.0021	31	6.2
9704081807	18.3951	120.959	77.9	6.1
9704110534	39.5557	76.9477	20	5.8
9704151819	39.62	76.9819	22.4	5.8
9704191526	78.4324	125.8178	10	5.7
9704211202	-12.6004	166.6428	65.7	6.3
9704211401	-7.3945	125.7763	436.3	5.7
9704220931	11.162	-61.0914	47.1	6.1
9704231944	13.9319	144.9407	114.3	5.8
9704270031	-19.1169	168.6796	51.1	6.2
9704281207	-42.4134	42.6807	10	6.1
9705011137	18.9948	-107.2671	15	6.2
9705031645	-31.6399	-179.3367	47.8	6.8
9705080253	24.8899	92.2768	10	5.6
9705081329	51.6735	-170.8742	33	5.7
9705090906	13.1446	144.7535	49.5	5.8
9705112216	-36.1161	-97.6809	10	5.6
9705131413	36.4817	71.0003	198.1	6.8
9705211410	-20.3924	169.2302	69	6.3
9705212251	23.0911	80.0818	29.1	6.0
9705220750	18.6706	-101.6584	84.6	6.3
9705221321	18.9866	121.3381	49.7	5.6
9705252322	-32.1148	179.8192	322.9	6.3
9705270800	-15.353	-173.2083	33	6.0
9705291702	-35.9445	-102.4959	10	6.0
9706022124	-57.8622	-25.642	33	6.1
9706102220	-35.7508	-108.2846	10	6.2
9706110929	-24.039	-177.5181	183.5	5.6
9706121207	-6.0057	147.0001	67.1	5.7
9706172103	51.3139	-179.3145	33	6.1

9706242304	-1.8877	127.9339	41.5	5.9
9706261921	-49.761	-114.6525	10	6.1
9707060954	-30.047	-71.8104	14	6.8
9707071119	1.104	97.6114	62.1	5.5
9707080224	23.8137	142.8132	10.5	5.6
9707081211	51.3849	-178.5847	30.6	5.7
9707111000	-5.7505	110.766	595.7	5.7
9707141609	43.163	146.4299	6.9	5.8
9707191222	-29.2001	-71.5917	4.2	5.6
9707191422	16.339	-98.1903	31.4	6.4
9707200030	52.5143	-167.5609	14.4	5.8

Table **B**.3. List of events recorded by Seisfaultgreece stations for P receiver function analysis.

Date	Lat	Long	Depth	mb
9707010340	42.5061	144.6596	71	5.9
9707071124	1.0437	97.6287	56.1	6.2
9707091924	10.5045	-63.5453	3	6.9
9707272235	-6.0469	103.8685	53.3	6.1
9708130445	25.132	125.8665	39.5	6.6
9708200715	4.3081	96.5056	24.7	5.9
9709251420	-13.7492	66.2555	10	5.9
9710041534	16.0065	-46.7515	10	6
9710111824	25.0242	122.5163	153.5	6
9710220955	44.68	146.2715	163.3	6.2
9711150705	43.7931	145.0345	158	6.4
9711160818	-4.9219	103.2035	55.5	5.9
9711280610	47.1089	145.5993	390.6	6.1
9712051135	53.8902	161.5591	43.6	6.1
9712051222	53.8696	161.38	42.5	6.7
9712051848	53.7222	161.721	16.7	6.1
9712052124	53.752	161.5226	26.5	6
9712070553	-5.9845	103.8051	33	6
9712091302	53.9221	161.8428	23.9	6
9803220108	-11.4055	66.2704	10	6.2
9804011756	-0.502	99.3222	61.6	7
9804221542	43.4502	147.0506	44.7	6
9804250607	-35.507	-17.2526	10	6.3
9805212231	-43.3649	41.5525	10	6
9806010534	52.8757	160.0159	48.6	6.3
9806241044	-37.2784	-17.3577	10	6.3
9807172203	-4.7137	103.0174	58.9	6.2
9808100952	7.4056	94.2391	33	5.9
9808301434	53.619	161.8093	28.8	6
9810010341	13.7502	-45.56	10	6.1
9810031115	28.5264	127.6489	216.5	5.9
9901240037	30.61	131.136	48.2	6.3
9902030635	-6.202	104.079	14.9	6
9902041928	4.054	95.279	55.2	5.9

9902051437	47.484	147.151	391	6.1
9902090019	42.312	143.022	65.1	6.2
9903070103	42.933	145.926	28.6	6
9904081310	43.607	130.35	566	6.4
9904222219	-27.939	26.675	3.7	5.9
9905121759	42.95	143.93	78.8	6.1
9906081204	15.068	-60.398	52.4	5.9
9907211346	4.585	97.152	165.5	6.4
9909220014	23.769	121.154	41.9	6.3
9909252352	23.817	121.076	22.2	6.1
9909280500	54.585	168.146	35.1	6
9910010719	-5.344	104.427	67.7	6
9910220218	23.494	120.421	22.4	6.4
9911011753	23.411	121.614	58.5	6.2
9911110241	49.336	155.622	51	6.1
9911111805	1.246	100.214	214.6	6.5
9911162037	-4.64	103.228	72.4	5.9
9911162254	42.133	142.38	70.4	6.3
9911281017	-1.293	88.918	10	6.3
9911290346	-1.301	89.005	10	5.9
9912111803	15.758	119.797	69.6	6.6
9912161036	-28.907	-13.292	10	6
0001142337	25.542	101.09	32	6.1
0001281639	26.062	124.547	184.7	6.6
0004071908	-17.6979	65.93	10	5.9
0005081229	-0.8769	98.057	33	5.9
0006040000	-4.7209	102.087	33	6.8
0006041628	-4.6919	102.141	52.7	7.7
0006042047	-4.6729	102.139	78.9	6.8
0006042153	-4.7749	102.259	65.7	6.6
0006042310	-5.3479	102.746	65.4	7
0006072142	-5.5609	103.132	12.4	6.3
0006081913	-5.1479	102.096	33	6.6
0006090800	-5.5989	102.731	10	6
0006090824	-5.6199	102.69	10	5.9
0006091424	-4.9269	103.01	40.8	6.5
0006101823	23.861	121.185	35.6	6.4
0006140020	-4.9739	102.165	52.6	6.4
0006140307	-24.0319	66.747	197	7.2
0006151522	-5.0129	102.624	59.2	7.9
0006180000	-13.8019	95.453	10	6.8
0006181444	-13.7979	97.424	10	8
0006201134	-14.0529	97.558	9	5.9
0007080452	-5.4049	102.695	9.3	5.9
0007100958	46.846	145.381	352.7	6.7
0007101039	-4.5009	103.766	106.7	6.7
0007131550	49.416	155.777	80.9	6.2
0007160321	20.292	122.14	18.1	6.5
0007222056	-4.0939	102.336	61.8	6.3
0008100707	48.725	142.267	13.3	6.5
0008241136	-5.9819	102.747	33	6.1
0009011156	1.445	96.548	31.3	5.9

0009120811	49.859	155.337	126.3	6.5
0009121627	-5.4329	101.817	0	6.1
0009131008	42.761	145.16	51.2	6.4
0009221822	-4.9889	102.099	0	6.3
0009230217	4.315	-32.6189	7.5	5.9
0009250400	-46.7399	37.82	10	6
0010041437	11.153	-62.4809	0	6.1
0010090230	10.013	92.991	44.2	5.9
0010300307	17.552	-61.2109	45.9	6.2
0011050445	-5.9229	102.68	0	6.2
0011291035	63.923	-150.3869	6.8	6.3
0101161325	-4.022	101.776	28	6.5
0102131928	-4.68	102.562	36	6.2
0102181304	-47.456	32.386	10	6
0103240627	34.083	132.526	50	6.4
0105180205	0.414	97.784	33	5.9
0108050516	12.224	93.352	96.4	5.9
0109020225	0.889	82.501	10	6.1
0109070245	-13.166	97.297	10	6.2
0110171129	19.354	-64.932	33	6
0201281350	49.381	155.594	33	6.1
0203171933	-45.221	35.105	10	6
0203260345	23.346	124.09	33	6.6
0203310652	24.279	122.179	32.8	6.4
0206281719	43.752	130.666	566	6.7
0208041516	-35.457	-16.238	10	6
0209132228	13.036	93.068	21	6.2
0209150839	44.833	129.923	586.3	6.4
0210122343	15.096	118.504	33	6.1
0210141412	41.174	142.249	61.4	5.9
0210161012	51.952	157.323	102.4	6.1
0210231127	63.514	-147.912	4.2	6
0210242153	6.03	94.419	64.6	6.2
0211020126	2.824	96.085	30	6.2
0211020946	2.954	96.394	27	5.9
0211032212	63.517	-147.444	4.9	7
0211170453	47.824	146.209	459.1	7.3
0301062343	15.651	119.658	10	6
0301271756	-46.048	35.057	10	6.3
0303021642	-36.958	-20.879	10	6.2
0303151941	52.249	160.387	30.2	6
0303260422	12.518	92.564	33	5.9
0304241056	48.764	154.991	43.8	6.1
0305092026	-48.209	32.272	10	6.1
0309211816	19.94	95.72	10	6.7
0309220445	19.81	-70.63	10	6.5
0309251950	41.83	143.83	33	8.3
0309260626	42.156	144.67	33	5.9
0309262038	41.988	144.576	33	5.8
0309272212	28.827	128.393	10	5.7
0309290236	42.45	144.38	25	6.1
0309292122	41.4	144.151	33	5.7

0310080906	42.648	144.57	32	6
0310081332	42.227	144.72	33	5.8
0310082315	42.21	144.689	33	5.9
0310090652	41.471	143.508	33	5.7
0310110008	41.924	144.358	33	5.9
0310171719	-5.077	102.458	35.1	5.7
0401110432	-36.696	53.352	5.3	6.1
0401161807	7.641	-37.704	10	5.9
0402220646	-1.527	100.46	42	6.3
0402262032	-17.644	66.772	10	5.9
0402280523	-18.705	-12.526	10	5.7
0403240153	45.45	118.17	15.8	5.7
0403261520	41.92	144.12	30.1	5.9

Table **B**.4. List of events recorded by GEOFON stations for S receiver function analysis.

Date	Lat	Long	Depth	mb
0306090152	24.413	122.02	48.1	5.8
0306100840	23.52	121.628	44.5	5.8
0306162208	55.492	159.999	174.8	6.3
0306300007	17.457	-61.14	33	5.7
0307022352	42.323	144.842	23.9	5.8
0307142000	-0.537	100.822	144.2	5.7
0307211516	25.975	101.29	10	6
0307231638	-15.592	-13.351	10	5.8
0307252213	38.415	140.996	6	6
0307270625	47.151	139.248	470.3	6.3
0308112122	12.124	93.53	100.2	6
0308212331	68.689	-148.038	12.5	6
0308312308	43.393	132.267	481.1	6.2
0309050123	5.316	95.9	124.8	5.7
0309100826	2.082	96.818	33	5.8
0309121540	-36.161	53.523	10	5.9
0309141845	18.667	121.033	64.4	5.7
0309211816	19.917	95.672	10	6.1
0309220445	19.777	-70.673	10	6.2
0309251950	41.815	143.91	27	6.9
0309252057	41.73	143.637	33	5.7
0309260626	42.156	144.67	33	5.9
0309262038	41.988	144.576	33	5.8
0309272212	28.827	128.393	10	5.7
0309272336	44.666	150.348	33	5.9
0309290236	42.45	144.38	25	6.1
0310080906	42.648	144.57	32	6
0310081332	42.227	144.72	33	5.9
0310082315	42.21	144.689	33	5.9
0310110008	41.924	144.358	33	5.9
0310110111	43.973	148.206	51.2	6.2
0310171719	-5.077	102.458	35.1	5.7

0312031411	42.36	144.732	33	5.7
0312052126	55.538	165.78	10	6.1
0312100438	23.039	121.362	10	6
0312101551	17.642	120.892	33	5.7
0312220847	42.279	144.598	37.5	5.8
0312290130	42.423	144.613	33	5.7
0312300950	47.053	154.187	33	5.7
0312312157	46.971	154.241	33	5.9
0401110432	-36.696	53.352	5.3	6.1
0401161807	7.641	-37.704	10	5.9
0402220646	-1.559	100.488	42	6.3
0402262032	-18.171	66.419	10	5.8
0402280523	-18.732	-12.562	11.2	5.7
0403082339	10.48	-43.919	10	6.1
0403192042	-34.5	55.28	10	5.7
0403200853	53.829	160.468	52.5	5.8
0403261520	41.863	144.209	22.4	5.7
0404111806	42.918	144.836	41.8	5.7
0404140154	55.226	162.659	51.3	6
0404162157	-5.214	102.718	44.5	5.8
0405080802	21.949	121.604	26.4	5.7
0405110828	0.415	97.825	21	6.2
0405190704	22.662	121.505	20	5.8
0406012047	-9.037	67.253	10	5.7
0406101519	55.713	160.031	184	6.3
0407081030	47.194	151.31	128	5.9
0407220945	26.55	128.88	43.3	6.2
0407251435	-2.4	104.02	577.5	7.3

Table **B**.5. List of events recorded by NOA stations for S receiver function analysis.

Date	Lat	Long	Depth	mb
0209132228	13.036	93.068	21	6.2
0209141958	13.055	93.157	33	5.7
0209150839	44.833	129.923	586.3	5.8
0209261255	-19.648	-12.014	10	5.7
0211020126	2.824	96.085	30	6.2
0211020447	12.701	92.856	33	5.8
0211020946	2.954	96.394	27	5.9
0211030337	38.886	141.977	39	5.7
0211032212	63.517	-147.444	4.9	7
0211170453	47.824	146.209	459.1	7.3
0212241248	47.715	154.6	33	5.7
0212271328	4.111	97.72	138.5	5.7
0301062343	15.651	119.658	10	6
0301090442	0.538	98.6	45.4	5.7
0301101518	0.202	97.957	27.2	5.7
0301220258	4.495	97.568	33	5.7
0301271756	-46.048	35.057	10	6.3
0302080849	-39.785	45.104	10	5.7

0302190501	44.149	141.799	214.4	5.9
0303151941	52.249	160.387	30.2	5.8
0303260422	12.518	92.564	33	5.8
0304071743	18.877	121.259	33	5.7
0304161759	40.983	142.208	57	5.7
0304241056	48.764	154.991	43.8	5.7
0304291044	-7.02	103.683	10	5.7
0304291353	43.706	147.805	62.5	6
0305140603	18.266	-58.633	41.5	6.5
0305260924	38.849	141.568	68	6.7
0305281615	-17.646	66.116	10	5.9
0306090152	24.413	122.02	48.1	5.8
0306100840	23.52	121.628	44.5	5.8
0306162208	55.492	159.999	174.8	6.3
0306300007	17.457	-61.14	33	5.7
0307022352	42.323	144.842	23.9	5.8
0307142000	-0.537	100.822	144.2	5.7
0307211516	25.975	101.29	10	6
0307231638	-15.592	-13.351	10	5.8
0307252213	38.415	140.996	6	6
0307270625	47.151	139.248	470.3	6.3
0308112122	12.124	93.53	100.2	6
0308212331	68.689	-148.038	12.5	6
0308312308	43.393	132.267	481.1	6.2
0309050123	5.316	95.9	124.8	5.7
0309100826	2.082	96.818	33	5.8
0309121540	-36.161	53.523	10	5.9
0309141845	18.667	121.033	64.4	5.7
0309211816	19.917	95.672	10	6.1
0309220445	19.777	-70.673	10	6.2
0309251950	41.815	143.91	27	6.9
0309252057	41.73	143.637	33	5.7
0309260626	42.156	144.67	33	5.9
0309262038	41.988	144.576	33	5.8
0309272212	28.827	128.393	10	5.7
0309272336	44.666	150.348	33	5.9
0309290236	42.45	144.38	25	6.1
0310080906	42.648	144.57	32	6
0310081332	42.227	144.72	33	5.9
0310082315	42.21	144.689	33	5.9
0310110008	41.924	144.358	33	5.9
0310110111	43.973	148.206	51.2	6.2
0310171719	-5.077	102.458	35.1	5.7
0310282148	43.844	147.75	65.4	6.1
0312031411	42.36	144.732	33	5.7
0312052126	55.538	165.78	10	6.1
0312100438	23.039	121.362	10	6
0312101551	17.642	120.892	33	5.7
0312110001	22.719	121.523	10	5.7
0312220847	42.279	144.598	37.5	5.8
0312290130	42.423	144.613	33	5.7
0312300950	47.053	154.187	33	5.7

0312312157	46.971	154.241	33	5.9
0401110432	-36.696	53.352	5.3	6.1
0401161807	7.641	-37.704	10	5.9
0402262032	-18.171	66.419	10	5.8
0402280523	-18.732	-12.562	11.2	5.7
0403082339	10.48	-43.919	10	6.1
0403192042	-34.5	55.28	10	5.7
0403200853	53.829	160.468	52.5	5.8
0403261520	41.863	144.209	22.4	5.7
0404111806	42.918	144.836	41.8	5.7
0404140154	55.226	162.659	51.3	6
0404162157	-5.214	102.718	44.5	5.8
0405080802	21.949	121.604	26.4	5.7

Table **B**.6. List of events recorded by CYC-NET stations for S receiver function analysis.

Appendix C

List of delay times and depth values

Stations	*Lon*	*Lat*	*Moho(s)*	*Moho(km)*	*Slab(s)*	*Slab(km)*
AGGI	22.32	39.01	4.4	36	-	-
ALEX	25.79	40.97	3.7	30	-	-
ANAT	22.68	39.74	3.8	31	-	-
APEZ*	24.88	34.97	4	33	6.2	52
ATH	23.72	37.97	3.1	25.5	-	-
DRAM	24.01	41.2	4.1	34	-	-
EVR	21.81	38.92	4	33	-	-
FODE*	24.95	35.37	4	33	6.7	58
FLOR	21.38	40.78	4.8	40	-	-
GVD	24.08	34.83	3.3	27	5.8	48.5
HIOS	26.04	38.25	3	25	-	-
IDI*	24.89	35.28	4	33	7.1	61
ITM	21.93	37.18	3.5	28.5	5	41
JAN	20.85	39.66	3.4	28	-	-
KARP	27.17	35.55	-	-	6.2	52
KEK	19.8	39.71	3.3	27	-	-
KOS1	27.21	36.84	3.2	26	-	-
KOZA	21.78	40.3	4.5	37	-	-
KRIS*	25.5	35.17	2.5	21	8.1	70
LESB	26.26	39.24	3.8	31	-	-
LIMN	25.16	39.95	3.4	28	-	-

Appendix C. List of delay times and depth values

Stations	*Lon*	*Lat*	*Moho(s)*	*Moho(km)*	*Slab(s)*	*Slab(km)*
LITO	22.48	40.1	3.7	30	-	-
LKR	23	38.65	3	25	-	-
MILO	24.44	36.67	4.4	36	10.2	90.5
NAXO	25.52	37.07	3.3	27	-	-
NEO	23.22	39.31	3.3	27	-	-
NPS*	25.61	35.26	2.5	21	7.4	64
NVR	23.86	41.35	4.8	40	-	-
PENT	23.96	38.04	4.5	37	-	-
PLG	23.45	40.37	3.7	30	-	-
RLS*	21.47	38.06	3	25	8	69.5
RODO	28.02	36.08	3	25	5.5	46
SAMO	26.83	37.7	3.5	28.5	-	-
SANT	25.45	36.37	4.2	34.5	11.1	99
SKD*	23.92	35.41	4	33	7.2	62
SKIR	24.57	38.85	3.2	26	-	-
SKOP	23.74	39.11	3	25	-	-
THES	22.96	40.63	3.6	29.5	-	-
VAM*	24.2	35.41	4	33	7.3	63
VELI	22.94	36.71	3.3	27	7.2	62
VLS	20.59	38.18	3.4	28	4.5	36.5
ZKR*	26.31	35.11	3.1	25.5	6.2	52

* no observed positive Ps Moho conversion, the delay times of Moho conversions are inferred from S receiver functions.

Table C.1. List of delay times of Moho and slab conversions as well as according depth values obtained from P receiver functions for stations.

Box No.	*lon*	*lat*	*Slab(s)*	*Slab(km)*	*LAB(s)*	*LAB(km)*
1	24.8	34.7	6	50.5	12.5	112.5
2	25.15	34.7	6	50.5	11.3	102
3	24.7	35.3	7	60	13.5	121.5
4	25.7	35.25	7.5	64.5	12	108

Box No.	*lon*	*lat*	*Slab(s)*	*Slab(km)*	*LAB(s)*	*LAB(km)*
5	26.5	35	8	69.5	14	126
7	24.75	35.75	10.5	93	12.4	112
8	25.5	35.75	9	79	13.5	121.5
9	26.25	35.7	8	69.5	13.5	121.5
10	24.1	36.15	9	79	12	108
11	24.9	36.1	11	98	13	117
12	26.3	36.25	11	98	14	126
13	26.8	36.25	11	98	12.5	112.5
14	24.2	36.8	13	117	17.5	157.5
15	25.4	36.6	13	117	16.5	148.5
16	26	36.9	15	136	19.5	175.5
17	27	36.75	13.5	122	19	171
18	28.75	36.75	-	-	15	135
19	23.25	37.3	7.5	64.5	-	-
20	24.9	37.25	16	145.5	21.5	193.5
21	25.25	37.1	18.5	169	25	225
22	26.4	37.4	16	145.5	20	180
23	24.6	37.8	16.5	150	19	171
24	25.75	37.65	18.5	169	19.5	175.5
25	22	37.6	5.5	46	19	171
26	21	38.6	17	155	22	198
27	22	38.5	13	117	17.5	157.5
28	24	38.5	22	202	18	162
29	27.4	38.2	19	174	12	108
30	21.75	39.5	22	202	17	153
31	22.4	39.4	20	183	17	153
32	23.8	39.8	22	202	19	171
33	26.8	39.8	21	192.5	17.5	157.5
34	20.25	40.2	23	211	20	180
35	22.4	40.8	24	220	18.5	166.5

Appendix C. List of delay times and depth values

Box No.	*lon*	*lat*	*Slab(s)*	*Slab(km)*	*LAB(s)*	*LAB(km)*
36	24	40.8	-	-	18.5	166.5
37	25.9	40.25	24	220	17	153
38	24.5	41.7	22.5	206.5	19	171
39	26.2	41.7	24	220	19	171

Table **C**.2. List of delay times of Slab and LAB conversions as well as according depth values obtained from S receiver functions box by box.

Box No.	*lon*	*lat*	*Moho(s)*	*Moho(km)*
1	24.3	34.7	3	25
2	24.2	35.2	2.6	21.5
3	24.7	35.2	-	-
4	25.25	35.25	3.5	28.5
5	25.6	35.2	2.5	21
6	25.8	35.2	2.8	23
7	26.25	35.25	3.1	25.5
8	24.25	35.6	2	17
9	25.15	35.6	3	25
10	25.2	36.25	3	25
11	25.75	36.2	2.5	21
12	28.3	36.25	2.7	22
13	23.2	36.7	2.7	22
14	24.25	36.75	3	25
15	24.65	36.75	4	33
16	25.2	36.65	3	25
17	25.8	36.8	2.8	23
18	26.7	36.6	3.4	28
19	22.2	37.25	3.5	28.5
20	24.7	37.25	3.5	28.5
21	25.5	37.2	3	25
22	20.7	38.2	4.5	37

Box No.	***lon***	***lat***	***Moho(s)***	***Moho(km)***
23	21.7	38	3	25
24	23.8	38	3.4	28
25	25.5	37.65	3	25
26	27	37.75	3.4	28
27	22	39	3.7	30
28	23.2	38.7	3.4	28
29	23.4	39.4	3.5	28.5
30	26.5	39.25	3.4	28
31	20	39.75	3.9	32
32	21	39.75	3.7	30
33	25.4	40	3.5	28.5
34	22	40.4	3.7	30
35	40.35	23.7	3.5	28.5
36	24	41.25	4	33
37	25.7	41.25	3.5	28.5

Table **C**.3. List of delay times of Moho conversions as well as according depth values obtained from S receiver functions box by box.

Appendix C. List of delay times and depth values

Danksagung

Mein größter Dank gilt Herrn Prof. Dr. Rainer Kind für die freundliche und effiziente Betreuung während meiner Promotionszeit. Er war jederzeit offen für Fragen, Diskussionen und Anregungen und sorgte für ein sehr nettes Arbeitsklima in der Arbeitsgruppe 2.4.

Unvergessen bleibt die Unterstützung von Dr. Günter Bock bei der Einarbeitung in das Thema, sowie seine stetige Hilfsbereitschaft und Freundlichkeit.

Bei Herrn Prof. Dr. Serge Shapiro möchte ich mich für die Unterstützung bei meinem Promotionsstart sowie die Übernahme des Koreferates bedanken.

Weiter danke ich den Mitgliedern der Prüfungskomission Prof. Dr. Onno Oncken, Prof. Dr. Frank Schilling, Dr. Heinrich Brasse und Frau Dipl. Geophys. Susanne Rentsch, die mir Ihre Zeit gewidmet haben.

Mein Dank gilt auch der Deutschen Forschungsgemeinschaft für die Finanzierung der Arbeit.

Für die konstruktiven und sehr hilfreichen Diskussionen danke ich insbesondere Prof. Dr. Denis Hatzfeld, Prof. Dr. Keith Priestley, Frau Dr. Helle Pedersen, Dr. Thomas Meier, Dr. Marco Bohnhoff, Dr. Prakash Kumar und Dr. Ali Dehghani.

Desweiteren bedanke ich mich bei den Betreuen der Netzwerke GEOFON, NOA, CYC-NET, MEDNET für die Bereitstellung der Daten.

All den Kollegen der sektion 2.4 danke ich für ihre Freudlichkeit und tolle Zusammenarbeit während meiner Doktorarbeit. Besonderer Dank gebührt Dr. Jörn Kummerow, Dr. Xueqing Li, Dr. Xiaohui Yuan, Dr. Ingo Wölbern, Dr. Ayman Mohsen und Dr. Joachim Saul, die diese Arbeit mit vielen interessanten Ideen und zahlreichen Diskussionen unterstüzt haben. Ein ganz besonderer Dank geht dabei auch an Dr. Mirjam Bohm, die immer für mich da war, an Benjamin Heit, für seine gute Laune, an Barbara Heuer für ihre geduldigen Bemühungen bei der Verbesserung meiner Deutschen Sprache und an Manfred Stiller, der mich in allen Situationen motiviert hat.

Für die Korrekturlesung gilt meine besondere Verbundenheit Herrn Dr. Prakash Kumar und Frau Amerika Manzanares.

Bei meiner lieben Zwillingsschwester Frau Dr. Sahar Sodoudi möchte ich mich ganz persönlich bedanken für ihre großartige Hilfe bei der Kalkulation der S Receiver Functions sowie ihre motivierten Unterhaltungen.

Abschließend noch ein ganz liebes Dankeschön an meinen Freund, der mich in schwierigen Situationen ohne wenn und aber unterstützt hat, an meine Eltern und meine Großmutter für

ihre liebevolle moralische und finanzielle Unterstützung und an meinen Onkel, der mir die Promotion in Deutschland ermöglicht hat.

Lebenslauf

Name:	Sodoudi
Vorname:	Forough
Geboren am:	27.01.1975, Berlin
Staatsangehörigkeit:	Iranerin

Schule

1980-1992	Besuch der Schule in Tehran
1992	Abitur (Experimentelle Wissenschaften)

Studium

1992-1996	Studium an der Azad Universität Tehran
1996	B.Sc in Physik (Festkörper Physik)
1997-2000	Aufbaustudium an der Tehran Universität (Geophysik Institut)
2000	M.Sc in Seismology
2001	Promotionsstart an der Freien Universität Berlin
seit Feb. 2001	Wissenschaftliche Mitarbeiterin (Doktorandin) am GeoForschngsZentrum in Potsdam